

PRESSURE-DEPENDENT HYDRAULIC  
TRANSPORT AS A MODEL FOR FLUID  
INDUCED EARTHQUAKES

DISSERTATION

zur Erlangung des Grades eines

DOKTORS DER NATURWISSENSCHAFTEN

am Fachbereich Geowissenschaften  
der Freien Universität Berlin

vorgelegt von

Dipl.-Geophys. Nicolas Hummel

Berlin, September 2013



EHRENWÖRTLICHE ERKLÄRUNG:

Hiermit versichere ich, dass ich die vorliegende Dissertation selbstständig und nur mit den angegebenen Quellen bzw. Hilfsmitteln angefertigt und verfasst habe.

Berlin, den 05.09.2013

Referent:  
Korreferent:  
Datum der Disputation:

Prof. Dr. Serge A. Shapiro  
PD Dr. Erik H. Saenger  
22. November 2013



Freie Universität Berlin  
Fachbereich Geowissenschaften  
Institut für Geologische Wissenschaften  
Malteserstr. 74 - 100  
12249 Berlin



# Summary

Borehole fluid injections are frequently used for diverse geo-technical and geo-energy applications. As such hydraulic stimulations modify the pore-fluid pressure level, they are typically accompanied by the occurrence of microearthquakes. Following the seismicity-based reservoir characterization (SBRC) approach, the spatio-temporal evolution of such earthquakes can be evaluated to quantify in-situ fluid transport properties of the rock, assuming that they are constant with time and pressure. However, field and laboratory experiments demonstrate that permeability can be significantly pressure-dependent.

The main objective of this thesis is to further investigate the phenomenon of fluid injection induced earthquakes taking into account pressure-dependent hydraulic transport properties. This study includes the derivation of analytical scaling relations for the triggering front (i.e. upper bound envelope of injection phase seismicity in space-time diagrams), the development of novel simulation models and their application to real data. In particular, a power-law as well as an exponential-dependent diffusivity model are considered and integrated into simulation workflows. Non-linear diffusion equations are numerically solved to compute synthetic seismicity. The analysis of their spatio-temporal signatures shows that the triggering front concept still holds for the case of a pressure-dependent hydraulic transport. However, instead of providing an in-situ diffusivity estimate, the triggering front is found to hydraulically characterize the medium not before but after stimulation including hydraulic fracturing of the rock. Additionally, synthetic seismicity also demonstrates that the triggering front signature depends on the diffusivity model in use. In agreement with scaling relations obtained from dimensional analysis, a linear and exponential-dependent diffusion both lead to a square root of time dependent triggering front. For the power-law diffusion model, this signature can yet change into a cubic root of time dependency. In other words, a time-dependent triggering front which is different from the square root is a clear indication of a non-linear diffusional pressure relaxation and therefore of a pressure-dependent hydraulic diffusivity.

Motivated by these findings, the applicability of the power-law diffusion model to real data is further examined. For this, hydraulic fracturing induced seismicity from the Barnett Shale gas reservoir (USA) is analyzed and compared with results

---

obtained from numerical simulations. A normalization approach is introduced to account for the influence of hydraulic anisotropy on the distribution of induced microearthquakes. Together with a concept of a factorized anisotropic pressure dependence of permeability, this approach allows to reconstruct the principal components of the permeability tensor from the characteristic dimensions of the seismicity cloud. A new modelling scheme is presented to compute calibrated non-linear pressure evolutions for real flow rate data. Following this numerical simulation workflow, synthetic seismicity is generated which shows similar spatio-temporal features as the ones from the Barnett Shale. Hence, a non-linear pore pressure diffusion with a power-law pressure dependence of the permeability is found to provide a reasonable model for hydraulic fracturing induced seismicity from the Barnett Shale.

Despite the injection phase, the impact of pressure-dependent hydraulic transport properties on post-injection induced microearthquakes is also comprehensively analyzed. The proposed normalization approach is further generalized and applied to seismicity from the Ogachi (Japan) and Fenton Hill (USA) geothermal reservoir stimulation. From the spatio-temporal analysis of corresponding induced seismicity, the back front (i.e. lower bound envelope of post-injection induced seismicity in space-time diagrams) is found to provide an estimate for the minimum principal component of the permeability tensor. However, to explain the observation that for some situations the linear diffusion back front does not appropriately describe the temporal evolution of post-injection induced microearthquakes, further catalogs of synthetic seismicity are generated on the basis of numerical simulations. For this, a new model of a so-called frozen medium diffusivity is developed and implemented. This model explicitly accounts for a post-injection enhanced hydraulic transport which is one of the major objectives of hydraulic stimulation including hydraulic fracturing treatments. It is found that the linear diffusion back front is only applicable for a weak non-linear fluid-rock interaction and three dimensional exponential diffusion. For such situations which seem to correspond to Ogachi and Fenton Hill, a cubic root of time-dependent power-law function is then a good approximation of the exact back front. For a strong non-linear fluid-rock interaction like the hydraulic fracturing, the back front is found to deviate from its linear diffusion signature. This finally is observed from synthetic seismicity, which shows similar spatio-temporal characteristics as the ones observed from hydraulic fracturing induced seismicity from the Horn River Basin (Canada) gas reservoir.

In such a way, this thesis represents a significant further development and important non-linear generalization of the SBRC approach. Simultaneously, it contributes to a better understanding of the physical processes of borehole fluid injections and associated earthquakes.

# Zusammenfassung

VORBEMERKUNG: Die vorliegende Dissertation ist bis auf diese Zusammenfassung in englischer Sprache geschrieben. Da auch in der deutschen Sprache einige *englische Fachausdrücke* gebräuchlich sind, wurde bei diesen Ausdrücken auf eine Übersetzung verzichtet.

Fluidinjektionen in Bohrlöchern kommen regelmäßig im Rahmen unterschiedlicher geotechnischer und geo-energierelevanter Anwendungen zum Einsatz. Da derartige hydraulische Stimulationen Änderungen des Porenwasserdrucks verursachen, werden sie in der Regel durch das Auftreten von Mikroerdbeben begleitet. Nach der Methode der seismizitätsbasierten Reservoircharakterisierung (SBRC) kann das raum-zeitliche Ausbreitungsverhalten dieser Erdbeben ausgewertet werden, um die in-situ Fluidtransporteigenschaften des Gesteins, welche als konstant mit der Zeit und dem Druck angenommen werden, zu quantifizieren. Allerdings zeigen sowohl Feld- als auch Laborexperimente, dass die Permeabilität signifikant druckabhängig sein kann.

Der wesentliche Gegenstand dieser Dissertation besteht darin, das Phänomen der durch Fluidinjektionen ausgelösten Erdbeben unter Berücksichtigung druckabhängiger hydraulischer Transporteigenschaften zu untersuchen. Diesbezüglich werden in dieser Arbeit analytische Skalierungsbeziehungen für die *triggering front* (Einhüllende der in Raum-Zeit Diagrammen dargestellten induzierten Seismizität der Injektionsphase) hergeleitet, sowie neue Simulationsmodelle entwickelt und auf Realdaten angewendet. Hierfür werden insbesondere sowohl eine Potenz- als auch eine exponentielle Abhängigkeit der Diffusivität berücksichtigt und in Simulationsprozesse integriert. Ferner werden nichtlineare Diffusionsgleichungen numerisch gelöst um synthetische Seismizität zu berechnen. Die Analyse deren raum-zeitlicher Signaturen zeigt, dass auch im Falle eines druckabhängigen hydraulischen Transportes die *triggering front* noch immer anwendbar bleibt. Allerdings stellt sich heraus, dass anstelle einer Abschätzung für die in-situ Diffusivität, die *triggering front* das Medium nicht vor, sondern nach der Stimulation bzw. dem *hydraulic fracturing* charakterisiert. Darüber hinaus belegen die synthetischen Seismizitätsverteilungen auch, dass der Charakter bzw. die Signatur der *triggering front* vom verwendeten Diffusivitätsmodell abhängt. In Übereinstimmung mit den aus der Dimensionsanalyse gewonnenen Skalierungsbeziehungen führen sowohl die lineare als auch die

---

exponentiell abhängige Diffusion zu einer von der Quadratwurzel der Zeit abhängigen *triggering front*. Diese Signatur kann sich im Fall der potenzabhängigen Diffusion zu einer Kubikwurzel der Zeit ändern. Mit anderen Worten, eine *triggering front* die eine von der Quadratwurzel der Zeit verschiedene Abhängigkeit aufweist, ist ein deutlicher Hinweis für eine nichtlineare Porendruckdiffusionsrelaxation und damit für eine druckabhängige hydraulische Diffusivität.

Motiviert durch diese Ergebnisse wird die Anwendbarkeit des potenzabhängigen Diffusionsmodells auf Realdaten weiter untersucht. Hierzu wird die induzierte Seismizität aus dem Barnett Shale Gasreservoir (USA) analysiert und mit Ergebnissen aus numerischen Simulationen verglichen. Ferner wird ein Normalisierungsansatz zur Berücksichtigung des Einflusses der hydraulischen Anisotropie auf die Verteilung der induzierten Mikroerdbeben eingeführt. Zusammen mit dem Konzept einer faktorisierten anisotropen Druckabhängigkeit der Permeabilität ermöglicht dieser Ansatz die Hauptkomponenten des Permeabilitätstensors unter Verwendung der charakteristischen Abmessungen der Seismizitätswolke zu rekonstruieren. Im Übrigen wird eine neue Modellierungsmethode vorgestellt, mit der unter Berücksichtigung realer Fließraten kalibrierte nichtlineare Druckentwicklungen berechnet werden können. Diesem numerischen Simulationsschema folgend wird synthetische Seismizität generiert, deren raum-zeitliche Merkmale zu denjenigen des Barnett Shale ähnlich sind. Somit stellt die nichtlineare Porendruckdiffusion zusammen mit einer auf dem Potenzgesetz basierten Druckabhängigkeit der Permeabilität ein berechtigtes Modell für die induzierte Seismizität in Barnett Shale dar.

Neben der Injektionsphase werden die Auswirkungen druckabhängiger hydraulischer Transporteigenschaften auch auf die induzierten Mikroerdbeben der Postinjektionsphase umfassend analysiert. Hierfür wird der vorgeschlagene Normalisierungsansatz weiter verallgemeinert und auf die bei geothermischen Reservoirstimulationen in Ogachi (Japan) und Fenton Hill (USA) induzierte Seismizität angewendet. Aus deren raum-zeitlicher Analyse folgt, dass die *back front* (Einhüllende der in Raum-Zeit Diagrammen dargestellten induzierten Seismizität der Postinjektionsphase) eine Abschätzung der kleinsten Hauptkomponente des Permeabilitätstensors liefert. Um allerdings die Beobachtung zu erklären, dass in manchen Situationen die auf der linearen Diffusion basierte *back front* die zeitliche Entwicklung der entsprechenden Mikroerdbeben nicht angemessen genug beschreibt, werden weitere Kataloge synthetischer Seismizität auf der Basis numerischer Simulationen erzeugt. Hierzu wird ein neues Modell der so genannten *frozen medium diffusivity* entwickelt und implementiert. Dieses Modell berücksichtigt explizit einen nach der Injektion verbesserten hydraulischen Transport, der einer der Hauptziele solcher Stimulationen bzw. *hydraulic fracturing* Operationen ist. Es zeigt sich, dass die auf der linearen Diffusion basierte *back front* nur bei schwacher nichtlinear Fluid-Gestein Wechselwirkung und dreidimensionaler exponentiell abhängiger Diffusion angewendet werden kann. Für

---

derartige Situationen, die auf Ogachi und Fenton Hill zuzutreffen scheinen, ist eine von der Kubikwurzel der Zeit abhängige Potenzfunktion eine gute Annäherung an die exakte *back front*. Für eine starke nichtlineare Fluid-Gestein Wechselwirkung wie dem *hydraulic fracturing* zeigt sich, dass die *back front* von ihrer auf der linearen Diffusion basierten Signatur abweicht. Dies wird schließlich in synthetisch erzeugter Seismizität beobachtet, die ähnliche raum-zeitliche Eigenschaften aufweisen, wie diejenigen der induzierten Mikroerdbeben aus dem Horn River Basin (Kanada) Gasreservoir.

Auf diese Weise stellt die vorliegende Dissertation eine wesentliche Weiterentwicklung und wichtige nichtlineare Verallgemeinerung der SBRC Methode dar. Gleichzeitig trägt sie zu einem besseren Verständnis der physikalischen Prozesse von Bohrlochfluidinjektionen und der damit verbundenen Erdbeben bei.

---

# Contents

	<b>Page</b>
<b>1 General introduction</b>	<b>1</b>
1.1 From porosity to permeability . . . . .	2
1.2 Aspects of rock permeability . . . . .	3
1.3 Borehole fluid injections and their applications . . . . .	7
1.4 Fluid injection induced seismicity . . . . .	11
1.5 Characterization of rock hydraulic transport properties . . . . .	14
1.6 Transition from linear to non-linear fluid-rock interaction . . . . .	18
1.7 Motivation . . . . .	21
1.8 Outline of this thesis . . . . .	21
<b>2 Microseismic estimates of hydraulic diffusivity in case of non-linear fluid-rock interaction</b>	<b>25</b>
2.1 Introduction . . . . .	27
2.2 Methodical background . . . . .	28
2.2.1 From linear to non-linear fluid-rock interaction . . . . .	28
2.2.2 Modelling non-linear pore-fluid pressure diffusion . . . . .	30
2.2.3 Simulation of synthetic microseismicity . . . . .	31
2.2.4 Triggering fronts in non-linear media . . . . .	32
2.2.5 Effective diffusivity . . . . .	34
2.3 Results . . . . .	36
2.3.1 Solutions for the pore-fluid pressure . . . . .	36
2.3.2 Diffusivity estimates . . . . .	40
2.4 Discussion of the results . . . . .	44
2.4.1 Triggering front signatures . . . . .	44
2.4.2 Assumptions and restrictions of our modelling . . . . .	45
2.5 Conclusion . . . . .	46
2.6 Appendix: Determination of the effective diffusivity . . . . .	47

<b>3</b>	<b>Non-linear diffusion-based interpretation of induced microseismicity: A Barnett Shale hydraulic fracturing case study</b>	<b>51</b>
<b>4</b>	<b>Back front of seismicity induced by non-linear fluid-rock interaction</b>	<b>81</b>
4.1	Introduction . . . . .	83
4.2	Meaning of back front estimates in anisotropic media . . . . .	88
4.2.1	Normalization of microseismic event clouds . . . . .	89
4.2.2	Case study: Ogachi, Japan . . . . .	92
4.2.3	Case study: Fenton Hill, New Mexico . . . . .	98
4.3	Back front signatures of non-linear fluid-rock interaction . . . . .	102
4.3.1	Modelling non-linear pore-fluid pressure diffusion . . . . .	103
4.3.2	Frozen diffusivity model . . . . .	104
4.3.3	Pore pressure profiles . . . . .	107
4.3.4	Seismicity triggering and analysis of spatio-temporal characteristics . . . . .	108
4.3.5	Synthetic seismicity . . . . .	110
4.3.6	Synthetic vs. real seismicity . . . . .	113
4.3.7	Frozen versus non-linear hydraulic medium behaviour . . . . .	116
4.4	Conclusion . . . . .	116
4.5	Appendix: Remaining pressure profiles and clouds of synthetic seismicity . . . . .	119
<b>5</b>	<b>Conclusions and perspectives</b>	<b>125</b>

---

<b>A</b>	<b>Estimates of fracture geometry and fluid transport properties from hydraulic fracturing induced seismicity</b>	<b>133</b>
A.1	Introduction . . . . .	134
A.2	Review of the methodology . . . . .	135
A.2.1	Hydraulic fracturing induced seismicity during the injection phase . . . . .	135
A.2.2	Hydraulic fracturing induced seismicity during the post-injection phase . . . . .	137
A.3	Hydraulic fracturing induced microseismic data . . . . .	138
A.4	Data overview . . . . .	138
A.5	Results . . . . .	142
A.5.1	Estimation of fracture geometry . . . . .	142
A.5.2	Estimation of fluid-loss coefficient . . . . .	143
A.5.3	Estimation of reservoir permeability . . . . .	144
A.5.4	Estimation of fracture body diffusivity . . . . .	144
A.6	Discussion and conclusion . . . . .	145
	<b>References</b>	<b>147</b>
	<i>List of Figures</i>	<b>165</b>
	<i>List of Tables</i>	<b>167</b>
	<i>Curriculum Vitae</i>	<b>169</b>
	<i>Publications</i>	<b>171</b>
	<i>Acknowledgements - Danksagung</i>	<b>177</b>



# Chapter 1

## General introduction

In civil, energy and environmental engineering hydraulic transport properties of rocks play an important role. As they control fluid flow, rock hydraulic properties are essential for a variety of projects such as the design of an effective drainage of construction sites, measures for water and soil protection or the elaboration of a long-term strategy for dealing with high-level radioactive waste disposal in geological subsurface repositories. Beyond these engineering applications, hydraulic transport properties become even more important when it comes to the exploration of geo-resources. In particular, knowing how fluids flow through a reservoir is fundamental to a successful management and operation of both geothermal and hydrocarbon reservoirs.

Admittedly, even up to date, an accurate determination of fluid migration in rocks is still one of the most difficult tasks for the exploration industry. This is due to the fact, that standard seismic methods have fundamental difficulties in accessing information about fluid mobility. While illuminating the subsurface no longer than for seconds, active seismic methods only provide snapshot-like images of the underground rock volume. Consequently, these methods are restricted in a way that they can not fully capture or quantify hydraulic processes which generally last for hours or days. However, over the past few years, one has understood that promising possibilities for rock hydraulic transport determination are given as a by-product of hydraulic stimulation treatments. Such fluid injections through a borehole into the surrounding rock are frequently used for waste injections, carbon capture and sequestration as well as particularly for the development of hydrocarbon and geothermal reservoirs. By evaluating the spatio-temporal evolution of fluid injection induced earthquakes, the so-called seismicity-based reservoir characterization (SBRC) approach allows to determine information about the permeability of rocks.

Since the present thesis further develops and generalizes the SBRC, a brief review of this approach will be given in the following. First, however, the concept of permeability will be shortly addressed along with an introductory description of borehole fluid injections and associated earthquakes.



Figure 1.1: Simplified illustration of rocks on the grain scale. The pore space (white) in between the rocks solid constituents (grey) is in-situ filled with fluids (liquid or gaseous).

### 1.1 From porosity to permeability

Although rocks are hard and appear to be solid, they are naturally porous. Rocks consist of mineral grains whose irregular shape and distribution forms fluid filled void spaces (Figure 1.1). The larger this pore volume the larger the amount of fluids (liquid or gaseous) trapped inside the rocks. The storage capacity can be quantified by the porosity  $\phi$  which describes the relative volume of void space not occupied by the solid substance. This pore volume is controlled by the shape, size and distribution of grains as well as on deformational processes during and after deposition like for instance burial compaction, dissolution or recrystallization. Furthermore, most geological formations down to depths interesting for hydrocarbon and geothermal exploration contain natural fractures (Zemanek et al., 1970; Plumb and Hickman, 1985; Seeburger and Zoback, 1982; Ito, 2003; Gale et al., 2007). Such fractures appear as displacement discontinuities on micro to macro scales. They comprise not only fissures and cracks which might be limited to a single rock layer but also include large scale fractures which extend throughout more than one single formation. Fractures exist due to brittle deformations in the Earth's crust associated with mechanical failure. Subsurface stress changes can exceed the rock strength resulting in failure on pre-existing planes of weakness. Such stress changes can be caused by natural processes like tectonic activity, altering lithostatic and thermal stresses, as well as man-made activities such as drilling of boreholes or injection and withdrawal of fluids. As porosity only quantifies the relative volume of void space it does not provide information about the size and distribution of pores nor on their hydraulic interconnectivity. Hence, different rocks of the same porosity may have a substantially different amount of interconnected fluid-filled pores. However, besides the storage capacity quantifying the amount of trapped fluid, it is also the interconnectivity of pores which plays a key role for transmitting fluids.

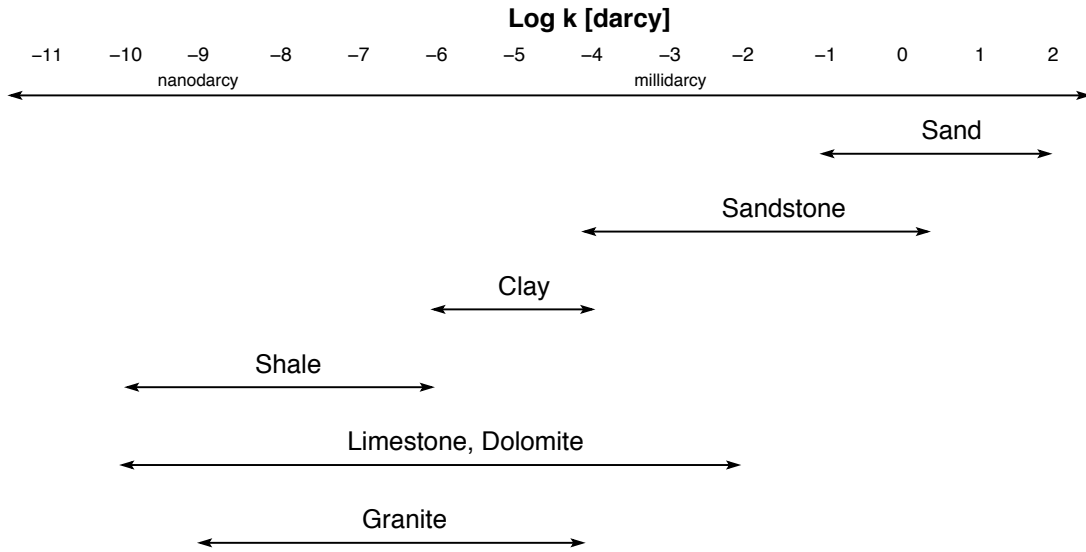


Figure 1.2: Range of laboratory measured permeabilities for different types of rocks (after Brace, 1980; de Marsily, 1986; Guéguen and Palciauskas, 1994; Jaeger et al., 2007)

## 1.2 Aspects of rock permeability

The capability with which fluids flow through the pore space is described by the permeability. Hence, permeability is a physical property of the rock which characterizes the hydraulic transport. The larger the interconnectivity of pores and fractures the larger the permeability. Generally, permeability is given in units of square meters although sometimes, in honor of the French engineer Henry Darcy, permeability is also given in darcy (1 darcy  $\approx 10^{-12}$  m<sup>2</sup>). From filtration experiments of water through beds of sands Darcy found an empirical relation which until today describes the main permeability formula in use. It relates the fluid filtration velocity  $\vec{q}$  to the pore pressure gradient  $\nabla p$  and is given in the most general form as (Jaeger et al., 2007)

$$\vec{q} = -\frac{\mathbf{k}}{\eta} \nabla p. \quad (1.1)$$

Here,  $\eta$  is the dynamic viscosity of the pore fluid and  $\mathbf{k}$  the second order permeability tensor accounting for the appreciable hydraulic anisotropy. This anisotropy is mainly caused by the naturally preferred orientation of minerals due to different physical and chemical processes related to diagenesis or stress induced alignment of cracks and fractures. However, as the experimental determination of the permeability tensor is quite laborious and associated with high technical effort (Kwon et al., 2004; Clavaud et al., 2008) most analysis neglect hydraulic anisotropy. This then simplifies the tensor to the scalar permeability coefficient  $k$ . Based on Darcy's law, Figure 1.2 shows a compilation of documented laboratory determined permeability coefficients for different porous rocks. As the permeability of intact rocks changes approximately

with the fourth power of the mean pore size (Dullien, 1992), it becomes obvious that permeability varies over several orders of magnitude, even for the same type of rock. For instance, sand or other material such as gravels show permeabilities greater than 1 darcy. In contrast, for rocks forming typical hydrocarbon and geothermal reservoirs, their permeability magnitudes are usually much smaller than 1 darcy. Especially for shales, permeabilities down to the order of about 0.1 to 300 nanodarcy are reported (Best and Katsube, 1995; Mayerhofer et al., 2006). However, due to fracture enhanced fluid flow, permeability magnitudes of in-situ rocks can be significantly larger than the ones obtained in laboratory measurements (Brace, 1980; Guéguen et al., 1996).

Such laboratory experiments (Summers et al., 1978; Moore et al., 1994; Guéguen et al., 1996; Morrow et al., 2001; Polak et al., 2003) including X-Ray imaging (Polak et al., 2003) have been also performed in order to investigate temperature effects on the permeability which in-situ rocks are expected to be exposed to. These experiments show that rock permeability decreases with increasing temperature. Chemical processes at elevated temperatures lead to mineral redistribution, dissolution and precipitation (Guéguen and Palciauskas, 1994). As a result, asperities can be diminished which decreases the aperture width. At the same time, pores and discontinuities can be filled up which overall reduces the capability of transmitting fluids by a factor of two to one hundred (Morrow et al., 1984; Vaughan et al., 1986; Lee and Farmer, 1993).

Apart from these permeability influencing factors (i.e. temperature or pore structure consisting of pore size and interconnectivity), the primary and by far most significant control on permeability is its sensitivity to pressure (and stress). With increasing depth pores and fractures are subsequently diminished and even closed as a result of the increasing lithostatic pressure. Evidently, this effect has to be considered when it comes to simulations of subsurface fluid flow, formation characterization or reservoir evaluation. To understand the interaction between the transport of fluids and the deformation of rock, it is necessary to understand how permeability evolves with pressure. For this, the pressure sensitivity of permeability has been extensively studied in laboratory experiments (Brace et al., 1968; Somerton et al., 1975; Walls et al., 1982; Yilmaz et al., 1994; David et al., 1994; Morrow and Lockner, 1997; Kwon et al., 2004; Dong et al., 2010; Li et al., 2009; Liu and Rutqvist, 2010; Meng et al., 2011).

To describe the observed strong dependency of permeability on effective pressure different relations have been proposed, including inverse power (Tiller, 1955; Ghabezloo et al., 2009), cubic-power (Gangi, 1978) and cubic-log relations (Walsh, 1981). However, the most widely observed and accepted data driven model shows an exponential dependence of permeability on effective pressure  $P_{eff}$  (Figure 1.3)

$$k = k_0 e^{-\kappa P_{eff}} = k_0 e^{-\kappa(P_c - \alpha P)}. \quad (1.2)$$

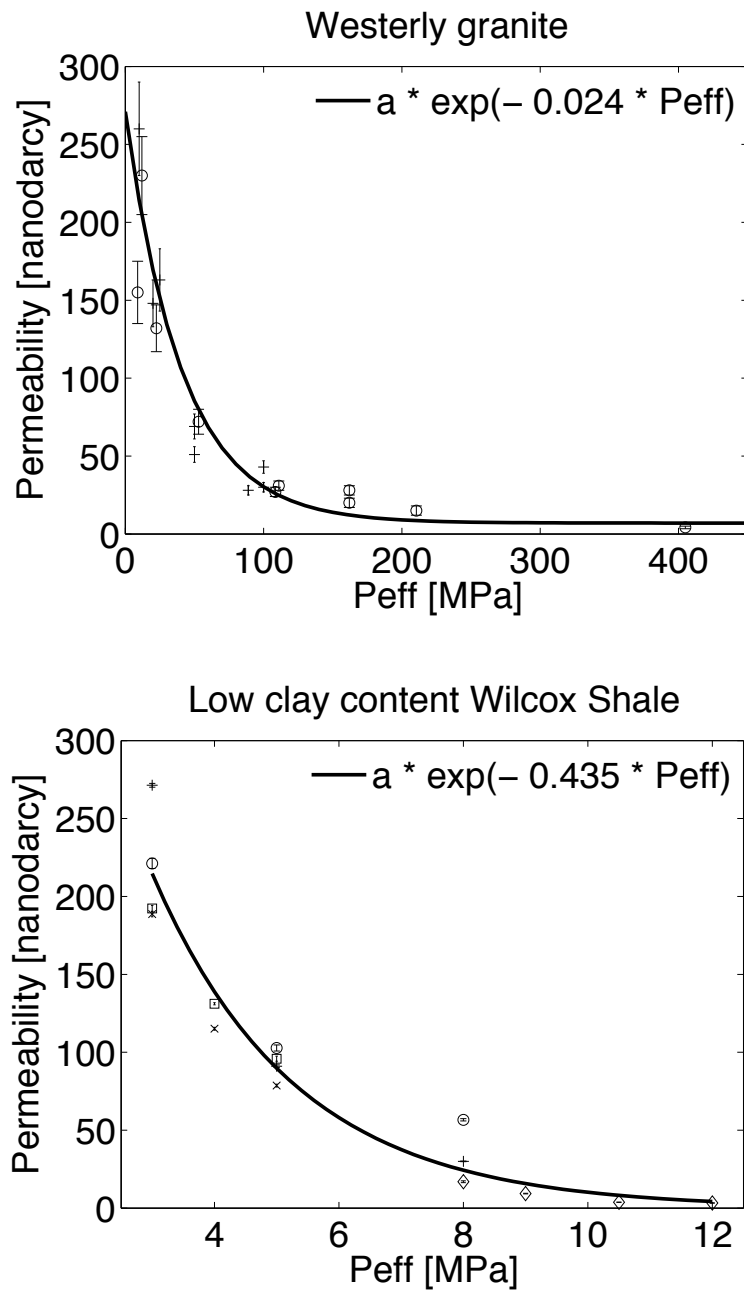


Figure 1.3: Two examples for an exponential dependence of permeability on effective pressure, both determined from laboratory measurements. Data of Westerly granite and Wilcox Shale are given in Brace et al. (1968) and Kwon et al. (2004).

## 1 General introduction

Table 1.1: Compilation of documented permeability compliances  $\kappa$  for different porous rocks (obtained from laboratory measurements) and injection sites.

Rock type / Reservoir	Porosity $\phi$	$\kappa$ [GPa <sup>-1</sup> ]	Reference
Faulted crystalline rocks	0.01 ... 0.03	35 ... 200	Evans et al. (1997)
Fractured rock		5 ... 400	Yilmaz et al. (1994)
Fractured rock		$\approx$ 500	Daley et al. (2006)
Granite		18 ... 69	Morrow and Lockner (1997)
Fractured granitic rocks		79 ... 92	Kranz et al. (1979)
Barre granite		21	Bernabe (1986)
Chelmsford granite		20	Bernabe (1988)
Pigeon Cove granite		14	Bernabe (1987)
Westerly granite		36	Bernabe (1987)
Sandstone	0.16 ... 0.24	1 ... 38	Nur et al. (1980)
Adamswiller sandstone	0.23	12	David et al. (1994)
Berea sandstone	0.21	10	David et al. (1994)
Boise sandstone	0.35	7	David et al. (1994)
Cholan sandstone <sup>1</sup>	0.17	3 ... 8	Dong et al. (2010)
E-bei sandstone	0.02 ... 0.11	60 ... 170	Li et al. (2009)
Fontainebleau sandstone	0.14	10	David et al. (1994)
Pottsville sandstone		17	Bernabe (1987)
Rothbach sandstone	0.20	18	David et al. (1994)
Tight gas sandstone	0.03 ... 0.08	33 ... 115	Walls et al. (1982)
Shale <sup>2,3</sup>		11 ... 81	Best and Katsube (1995)
Chinshui Shale <sup>1</sup>	0.09 ... 0.14	17 ... 43	Dong et al. (2010)
Coalbed methane reservoir <sup>4</sup>		193 ... 446	Meng et al. (2011)
Fenton Hill		79 ... 196	Nathenson (1999)
KTB		140	Millich et al. (1998)
Rosemanoves		225 ... 334	Nathenson (1999)

<sup>1</sup> Taiwan Chelungpu fault Drilling Project, TCDP

<sup>2</sup> Venture gas field (Canada)

<sup>3</sup> Beaufort-MacKenzie Basin (Canada)

<sup>4</sup> Southern Qinshui Basin (China)

Here,  $P_{eff} = P_c - \alpha P$ , where  $P_c$  is the confining pressure,  $\alpha$  a poroelastic parameter and  $P$  the pore-fluid pressure. Although  $\alpha$  does not necessarily have to be constant, it is close to one for most fractured reservoir rocks. Hence, reducing the confining pressure or increasing the pore pressure both reduce  $P_{eff}$ . Additionally, at reservoir operating conditions, variations in the confining pressure are supposed to be rather small (i.e.  $\Delta P_c \approx 0$ ). Consequently, equation 1.2 becomes

$$k = k_0 e^{\kappa P}, \quad (1.3)$$

where  $k_0$  describes a reference or background medium permeability. The parameter  $\kappa$  denotes the so-called permeability compliance which describes the variation of permeability with pore pressure (Walls et al., 1982; Yilmaz et al., 1994; Guéguen et al., 1996; Nathenson, 1999). This exponential relation holds for most rocks including sandstones (David et al., 1994), granites (Kranz et al., 1979), coals (Somerton et al., 1975; Durucan and Edwards, 1986) and even shales (Best and Katsube, 1995). Table 1.1 summarizes values of  $\kappa$  documented for different porous rocks and injection sites. Although the magnitudes of the permeability compliance of most rocks are usually in the order of 10 - 100  $\text{GPa}^{-1}$ , values of 200 to even 500  $\text{GPa}^{-1}$  have also been observed. However, this then includes that the rock is either faulted or even fractured. These aforementioned characteristics have shown that hydraulic permeability is strongly influenced by the presence of cracks and other heterogeneities of the pore space. Hence, it becomes obvious that permeability is a highly fluctuating parameter whose estimates can vary by orders of magnitude, even for adjacent locations.

Although permeability is generally used to describe and quantify the ability of rocks to transmit fluids, the alternative concept of the hydraulic diffusivity may be used instead. Both transport properties are directly proportional to each other (Shapiro et al., 1997; Jaeger et al., 2007)

$$\mathbf{k} = \frac{\eta}{N} \mathbf{D}, \quad (1.4)$$

where  $\eta$  is the dynamic viscosity of the pore fluid and  $N$  is a poroelastic modulus related to porosity and different bulk moduli for the pore-fluid, the rock skeleton, the grain material as well as the Biot coefficient. Thus, instead of [ $\text{m}^2$ ], the components of the diffusivity tensor  $\mathbf{D}$  have the unit of [ $\text{m}^2/\text{s}$ ].

### 1.3 Borehole fluid injections and their applications

Accurate knowledge of the permeability is important for engineering projects associated with borehole fluid injection. Such fluid injections into the deeper subsurface are used for different purposes, including for instance the capture and sequestration of carbon dioxide (CCS) (see for example Holt et al., 1995; Gibbins and Chalmers, 2008; Haszeldine, 2009; Gilfillan et al., 2009; Mathieson et al., 2010). In order

to reduce the rate of global warming, the amount of this greenhouse-gas within the atmosphere needs to be reduced. One way of mitigating the quantum of fossil power-plant emitted CO<sub>2</sub> is to inject and store carbon dioxide into underground geological formations. Potential long-term storage sites include depleted oil and gas reservoirs or deep saline aquifers (Figure 1.4). However, in order to prevent the carbon dioxide from penetrating back to the surface due to leakage, the storage site must have an impermeable cap rock.

Despite CCS or other geo-technical engineering projects, the most common applications of fluid injections through a borehole into the surrounding rock are used for energy production, in particular for hydrocarbon exploration. These hydrocarbons are trapped in the pore space of subsurface geological formations (Figure 1.4). Depending on the in-situ conditions of pressure and temperature these pores are mainly filled with oil or natural gas. To exploit hydrocarbon bearing formations with a relatively high permeability (i.e. so-called conventional reservoirs) wells are drilled into the corresponding reservoir. Due to the pressure gradient between the reservoir pressure and the pressure at the bottom of the well hydrocarbons are forced to flow through the porous rock into the well. Typically, this stage is referred to as primary recovery. However, due to a decrease in reservoir pressure fluids can not be recovered longtime at high and constant rates. Methods have been developed in order to artificially provide a longterm profitable production rate. These secondary recovery methods include for instance water flooding to displace residual oil (Carnes Jr., 1966; Economides and Nolte, 2000). For this, water is injected into the reservoir to increase its pressure and to press fluids to adjacent production wells.

However, since most of the discovered conventional reservoirs have already been exploited during the past, new sources for fossil energy production had to be discovered. In contrast to conventional reservoirs, these alternative hydrocarbon bearing formations are tight and compact. Therefore, they have a significant lower permeability. Such unconventional reservoirs include for instance, shale gas, tight gas sand, coalbed methane, heavy oil or oil/bituminous sand (Holditch, 2003). Since unconventional reservoirs do not produce commercially profitable volumes of hydrocarbons their exploitation requires immense technical efforts. These efforts include the injection of steam and solvents (Farouq Ali, 1974; Farouq Ali and Abad, 1976; Brock and Bryan, 1989; Macaulay et al., 1995) or special stimulation treatments called hydraulic fracturing (Hubbert and Willis, 1957; Economides and Nolte, 2000). The latter case corresponds to a massive hydraulic stimulation aiming to increase the permeability and hence production by connecting pre-existing cracks with larger fractures. Specially engineered fluids are injected into the reservoir through an open-hole section or perforated interval of the wellbore with flow rates high enough so that the bottom hole pressure exceeds the strength of the rock (i.e. minimum principal tectonic stress). As a result, the rock breaks artificially and a

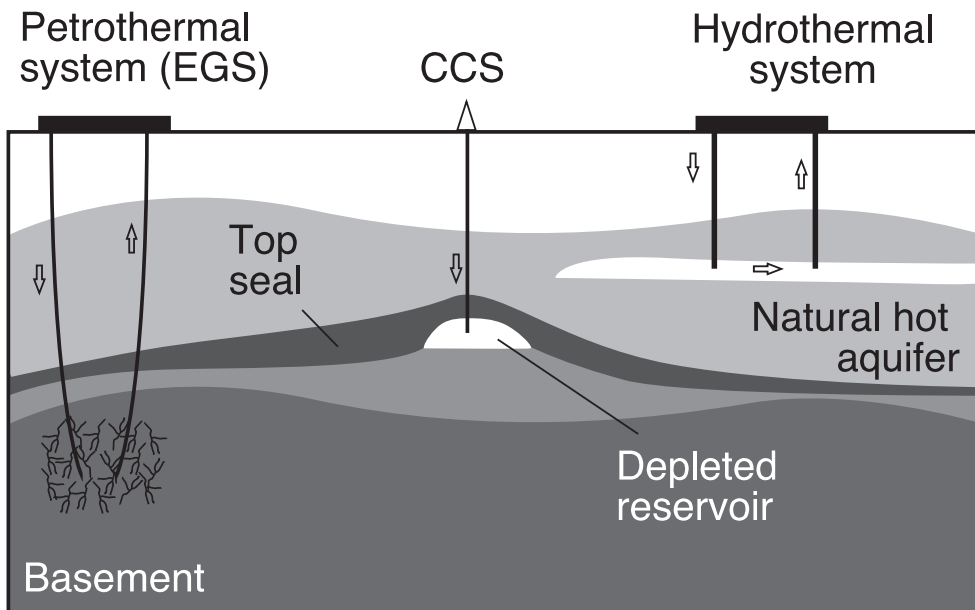
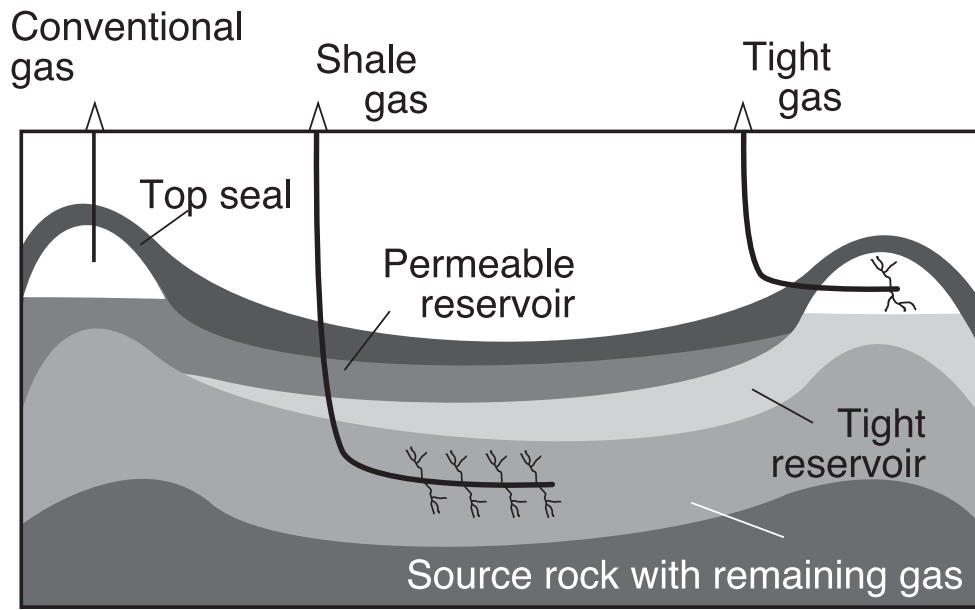


Figure 1.4: Applications of borehole fluid injections for hydrocarbon and geothermal exploration as well as carbon capture and sequestration (CCS).

tensile opening hydraulic fracture is created which further penetrates up to several hundreds of meters into the formation. Hence, the drainage area for hydrocarbons is significantly increased. Simultaneously, highly permeable flow paths are created which work as guiding paths for the oil and gas to drain from the rock into the cracks and finally to the well.

Since a hydraulically induced fracture will open along the least resistive direction, its orientation and geometry depends on the local underground stress conditions. The stress state of subsurface rocks can be fully described using the concept of principal stresses,  $\sigma_1 \geq \sigma_2 \geq \sigma_3$  (Jaeger et al., 2007). These principal stresses can be found after a coordinate transformation into the principal coordinate system of the stress tensor in which shear stresses vanish. Since the Earth's surface is in contact with fluids (i.e. water and air) which cannot support shear tractions, the Earth's surface itself represents a principal stress plane. Hence, at a certain location and (shallow) depth, one principal stress should be close to the vertical direction while the other two are in the horizontal plane (Zoback and Zoback, 2002). The magnitude  $S_v$  of the vertical stress corresponds to the weight of the overburden while  $S_{H_{max}}$  and  $S_{h_{min}}$  denote the maximum and minimum principal horizontal stress. If the minimum principal stress is horizontal,  $\sigma_3 = S_{h_{min}}$ , the fracture orientation will be vertical. Vice versa, if  $\sigma_3$  is vertical (i.e.  $S_v$ ), the fracture orientation will be horizontal.

Independent of its orientation, the fracture will close as soon as the pressure is released after stop of the injection. To prevent fracture closing, proppant is added to the treatment fluid. These solid materials include for instance sand or high strength granular substitutes for sand (Mader, 1989; Sheriff, 2002; Renpu, 2011). The economic benefits include a cost effective exploration strategy because the hydraulically increased drainage results in higher production rates with less production wells. However, due to the fact that the fracturing fluid includes some additives, there are also environmental concerns including for instance groundwater contamination (Osborn et al., 2011; Vidic et al., 2013).

Besides hydrocarbon exploration, hydraulic borehole stimulation treatments are also carried out to develop non-hydrocarbon energy sources. A not yet fully established and adequate alternative to fossil energy is geothermal energy (Figure 1.4). The source of this renewable energy is the heat stored in the subsurface (Gudmundsson and Lund, 1985). This heat is produced by radioactive processes inside the Earth (for example Schubert et al., 2001; Stevenson, 2004; Jaupart and Mareschal, 2010). Basically, there are two different types of geothermal reservoirs. So-called hydrothermal reservoirs consist of a naturally hot aquifer from which hot water is extracted to the surface (Elders et al., 1984; Muraoka et al., 1998; Baria et al., 1999; Barbier, 2002). Hence, such reservoirs could be exploited using only one single borehole. However, in order to keep a hydrothermal reservoir in sustainable operation, the extracted and therefore

cooler fluid is circulated by re-injection from a second well. In contrast, petrothermal reservoirs have no own aquifer. Therefore, water has to be circulated from an injection well through the hot formation to a production well (Potter et al., 1974; Smith, 1983; Baria et al., 1999; Tenzer, 2001; Lund, 2007). Such reservoirs are usually referred to as hot-dry-rock reservoirs or Enhanced Geothermal Systems (EGS). In the optimal case the reservoir rock is naturally fractured and has a small to modest permeability. In this case, water can be circulated from the injection to the production well using injection pressures being smaller than the minimum principal tectonic stress. However, if the permeability is too low resulting in an insufficient hydraulic connectivity between both wells, artificial flow passages have to be induced prior to stimulation. This is normally done by hydraulic water fracturing treatments (Smith, 1983; Brown et al., 1999).

## 1.4 Fluid injection induced seismicity

Independent of the application of borehole fluid injections (including also extraction and withdrawal operations), they are typically accompanied by small magnitude earthquakes. This phenomenon has been widely observed throughout the past dating back to 1966. The seismically monitored experiment of injecting pressurized waste water into a disposal well close to the city of Denver has proven that earthquakes can be triggered by such hydraulic operations (Healy et al., 1968, 1970; Raleigh et al., 1972; Gibbs et al., 1973; Raleigh et al., 1976). Soon after, this discovery has been confirmed from water flooding treatments at Los Angeles (Teng et al., 1973) as well as from the research fluid injection experiment at Matsushiro, Japan (Othake, 1974).

Although seismogenic processes are still subject of current research, such hydraulic experiments have shown that artificial man-made changes in pore-fluid pressure can modify the stress state within subsurface rocks in a way capable to induce an earthquake as follows.

The stress state of rocks can be analyzed graphically by so-called Mohr-Coulomb diagrams (Mohr, 1914). For any plane within the rock, these diagrams relate the shear stress  $\tau$  with the normal stress  $\sigma_n$ . For the simplified 2-D case, the state of stress is completely described by a Mohr circle of radius  $(\sigma_1 - \sigma_3)/2$  being centered at  $(\sigma_1 + \sigma_3)/2$ , where  $\sigma_1$  and  $\sigma_3$  are again the maximum and minimum principal stresses (Figure 1.5). Following the linearized Coulomb criterion, rock failure is assumed to occur when the shear stress  $\tau$  equals the sum of the shear strength  $S_0$  and frictional stress on the fault plane  $\mu \cdot \sigma_n$  (Scholz, 2002; Jaeger et al., 2007)

$$|\tau| = \mu \cdot \sigma_n + S_0. \quad (1.5)$$

Equation 1.5 describes a straight line of slope  $\mu$  in the  $\sigma$ - $\tau$  plane. The parameter  $\mu$  is the so-called coefficient of internal friction which, taking into account the angle of internal friction  $\phi$ , is also expressed as  $\mu = \tan \phi$ . According to Byerlee's law (i.e.

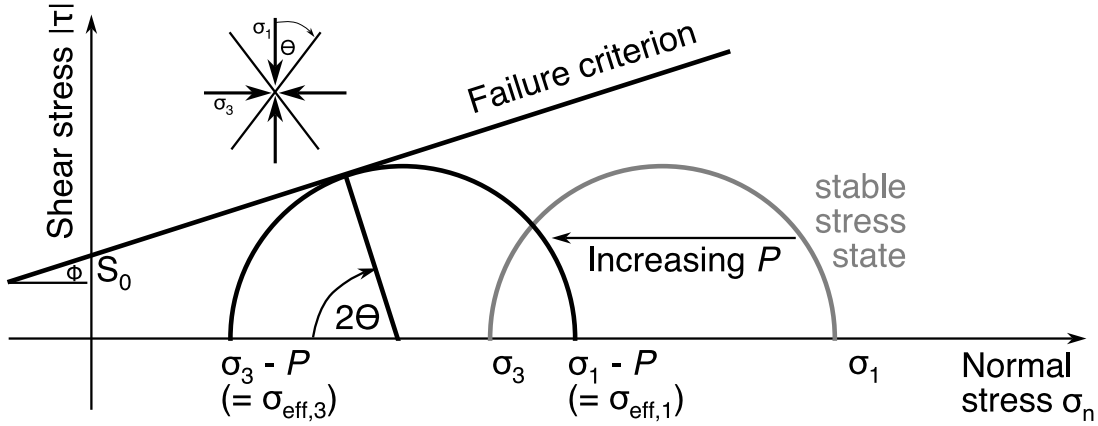


Figure 1.5: Sketch showing a Mohr diagram together with a Coulomb failure criterion. A safe stress state is represented by a Mohr circle which is below the failure line (grey). However, a safe in-situ stress state can become critical if the pore pressure  $P$  is sufficiently increased. This shifts the Mohr circle closer to the failure line. If this line becomes tangent to the Mohr circle shear failure occurs.

bilinear empirical relation) typical laboratory determined magnitudes of  $\mu$  are of the order of 0.6 (Byerlee, 1978). However, despite the fact that this relation holds for a common range of different types of rocks, noticeable exceptions include for instance clays and other sheet silicates (Jaeger et al., 2007). Equation 1.5 further shows that the failure line intercepts the ordinate at  $S_0$ . This parameter  $S_0$ , sometimes also denoted as cohesion  $c$ , reflects the fact, that without any normal stress a certain shear stress is still necessary to initiate failure. Any Mohr circle below this failure envelope defines a stable stress state which does not give rise to failure on any plane. In contrast, if the stress state defines a Mohr circle which is tangent to this line, the rock will fail in shear. Then,  $\Theta$  defines the angle by which the failure plane is oriented to the  $\sigma_1$  direction.

However, so far, the effect of pore fluids has not been considered. Due to the porous nature of rocks, their pore space is filled in-situ with fluids under pressure. Since the pore-fluid pressure  $P$  acts against the total stress, Terzaghi (1936) proposed that rock failure is not controlled by the simple stresses but by the effective stresses (i.e. principal stresses minus pore pressure)

$$\sigma_{eff,i} = \sigma_i - P \quad \text{for } i = 1, 2, 3. \quad (1.6)$$

Given that most experiments on rocks support this effective stress law, the aforementioned discussion still holds in the presence of fluids. If stresses  $\sigma$  are replaced by the effective stresses  $\sigma_{eff}$ , Mohr circles are shifted closer to the failure line (i.e. to the left) by the amount of the pore pressure  $P$ . Consequently, a safe in-situ stress state can become critical if the pore pressure build up is sufficient. Since most parts

of the Earth's crust are in a critically stressed state (Barton et al., 1995; Zoback and Townend, 2001) artificial stress perturbations through hydraulic stimulations increase the pore pressure inside the interconnected pore space which in turn decreases the effective normal stress

$$\sigma_{n,eff} = \sigma_n - P. \quad (1.7)$$

A sufficient reduction of the effective normal stress can therefore lead to shear induced reactivation of pre-existing sub-critically stressed cracks or fractures by releasing the previously accumulated shear stress in the stimulated rock volume (Pearson, 1981; Zoback and Harjes, 1997; Shapiro et al., 1997; Rutledge et al., 1998; Shapiro et al., 1999, 2002; Rutledge and Phillips, 2003). Typically, such earthquakes associated with borehole fluid injections (or extractions) have small magnitudes ranging from -3 to 2. This is why such usually non-noticeable earthquakes are referred to as (micro)seismic events or simply events. However, occasionally, borehole fluid injections induce events of a significant larger magnitude (Davis and Pennington, 1989; Nicholson and Wesson, 1992; Lahaie et al., 1998; Ake et al., 2005; Ottemöller et al., 2005; Dahm et al., 2007; Häring et al., 2008; Evans et al., 2012).

If an event occurs, seismic waves travel away from the unknown event source location. The P- and S-wave field can be recorded by a monitoring system which typically consists of a few to several hundred receivers (i.e. usually geophones and/or seismometers but also accelerometers) which are installed subsurface, near surface or even at the surface (Fehler, 1989; Rutledge et al., 2004; Häring et al., 2008; Cuenot et al., 2008; Viegas et al., 2012). If the layout and positioning of the seismically sensitive monitoring network is adequate, the hypocenter of a microseismic event can be located with accuracies in the order of several tens of meters (for example House, 1987). For this, different (semi-)automatic location algorithms like arrival time based (i.e. require to identify seismic phases and picking of P- and S-wave arrival times, Thurber and Rabinowitz, 2000; Lay and Wallace, 1995) or migration based (i.e. use full wavefield around a detected event, McMechan, 1982; Baker et al., 2005) have been developed. Once induced events are accurately located microseismic monitoring provides numerous possibilities of analyzing the nature of induced seismicity including especially the high resolution spatial mapping of fractures.

In such a way, passive seismic monitoring provides valuable applications for both geothermal and hydrocarbon exploration. Some of these applications include for instance the estimation of the stimulated reservoir volume (e.g. Brown et al., 1999; Mayerhofer et al., 2006; Häring et al., 2008), leakage detection due to casing failure (e.g. Talebi et al., 1998), observations of the caprock integrity (e.g. Zoback and Zinke, 2002; Lescanne et al., 2011), quantification of the reservoirs seismotectonic conditions for hazard risk assessment (Langenbruch and Shapiro, 2010; Shapiro et al., 2010) or the determination of the fracture geometry and azimuth (Pearson, 1981; Eberhart-Phillips and Oppenheimer, 1984; Rutledge et al., 1998; Fisher et al., 2002; Rutledge

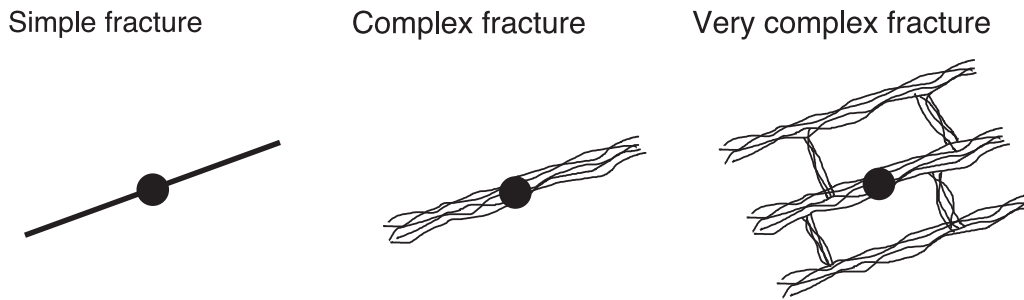


Figure 1.6: Categorization of different types of fractures after Fisher et al. (2002). The simple fracture model represent the classical bi-wing shaped hydraulic fracture with the well bore in the centre. This type of fracture approximately corresponds to the situation at Cotton Valley (Rutledge and Phillips, 2003; Dinske et al., 2010) or the Canyon Sands (Fischer et al., 2008). In contrast, the very complex fracture model describes the situation observed at Barnett Shale where induced hydraulic fractures interact with pre-existing natural fractures which together form a complex fracture network (Gale et al., 2007; Maxwell et al., 2009).

and Phillips, 2003; Dinske et al., 2010). Especially the latter one was of particular importance, as mapping of induced seismicity helped to optimize injection strategies for economic hydrocarbon production from unconventional reservoirs like the Barnett Shale. For this tight gas reservoir, spatial mapping of induced events significantly helped to reveal its complex fracture geometry (see Figure 1.6, Fisher et al., 2002; Gale et al., 2007; Maxwell et al., 2009). For waste injections or CCS, microseismic monitoring helps to observe and ensure that fluids do not migrate but are contained in corresponding underground salt caverns or depleted formations (Bohnhoff et al., 2010; Bohnhoff and Zoback, 2010; Lescanne et al., 2011). However, besides these applications of passive seismic monitoring, induced seismicity can also be used to characterize and quantify rock hydraulic transport properties.

## 1.5 Characterization of rock hydraulic transport properties

In the past, much effort has been made to estimate and quantify rock hydraulic transport properties. However, in the frame of understanding the nature and physics of fluid injection induced seismicity, first fundamental findings were obtained by Shapiro et al. (1997, 1999, 2002). For hydraulically induced events, they showed that the dominant mechanism of seismicity triggering is governed by a diffusional relaxation of the pore-fluid pressure perturbation which initially has been created at the injection source. In agreement with the aforementioned Mohr-Coulomb failure concept, these pressure perturbations can induce seismic events caused by shear slippage.

If a real configuration of a fluid injection into a borehole is approximated by a point source of pressure perturbation into an infinite hydraulically heterogeneous anisotropic poroelastic fluid-saturated medium, then, in the low frequency limit of Biot's equations of poroelasticity (Biot, 1962), the spatio-temporal evolution of the pressure perturbation  $p$  can be described by the following differential equation of diffusion (Shapiro et al., 2002)

$$\frac{\partial p}{\partial t} = \frac{\partial}{\partial x_i} \left[ D_{ij} \frac{\partial p}{\partial x_j} \right] \quad \text{for } i, j = 1, 2, 3. \quad (1.8)$$

Here,  $t$  is the time,  $D_{ij}$  are the components of the hydraulic diffusivity tensor, and  $x_{i,j}$  are the components of the radius vector from the injection point to an observation point inside the medium. For the simpler case of a homogeneous and hydraulically effective isotropic medium equation 1.8 becomes (Shapiro et al., 1997)

$$\frac{\partial p}{\partial t} = D \nabla^2 p. \quad (1.9)$$

Equation 1.9 shows that the spatio-temporal pressure evolution in such a medium is completely described by the constant with time and pressure scalar hydraulic diffusivity  $D$ . Following the seismicity-based reservoir characterization (SBRC) approach (Shapiro et al., 1997, 1999, 2002) a reasonable heuristic field scale magnitude estimate of  $D$  can be determined by analyzing the spatio-temporal characteristics of induced events. For this, so-called  $r - t$  diagrams are computed which show the radial distance between event location and the injection point  $r$  as a function of the elapsed time  $t$  since beginning of the injection. In such diagrams, clouds of hydraulically induced events show a characteristic parabolic signature which can be understood as footprint of the underlying hydraulic transport. This characteristic signature of pore pressure diffusion triggered seismicity is evaluated by the so-called triggering front. The triggering front represents a spatial surface which approximately separates regions in which the pressure has not yet relaxed from those in which the pressure has already relaxed. Hence, in  $r - t$  diagrams, it approximately describes the outermost envelope of induced seismicity. From the dispersion equation of the diffusion wavenumber the following expression for the triggering front can be obtained assuming a homogeneous and effective hydraulically isotropic medium (Shapiro et al., 1997)

$$r = \sqrt{4 \pi D t}. \quad (1.10)$$

Hence, fitting this square root of time-dependent parabola as an envelope of injection phase induced events allows to heuristically estimate the field-scale in-situ hydraulic diffusivity of a given seismically active rock volume.

The following example of the Fenton Hill, New Mexico, hydraulic stimulation treatment demonstrates the applicability of the SBRC approach. The purpose of this borehole fluid injection experiment was to create an artificial geothermal reservoir

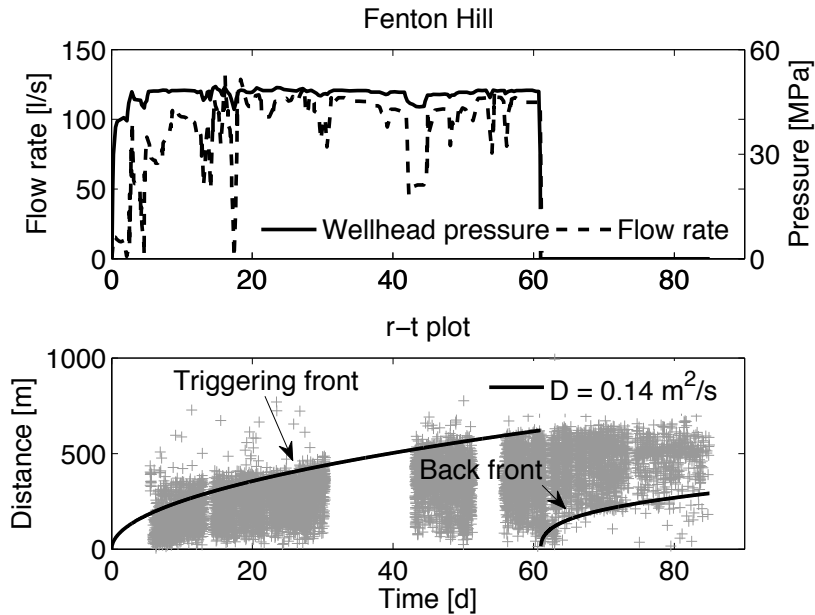


Figure 1.7: Engineering data and  $r - t$  diagram of induced seismicity being recorded during and after the 1983 fluid injection experiment carried out at Fenton Hill, New Mexico. Fitting the triggering front (equation 1.10) as the envelope of injection phase induced events provides a heuristic field scale in-situ diffusivity estimate of  $D = 0.14 \text{ m}^2/\text{s}$ . With termination of the fluid injection, a developing domain of seismic quiescence evolves. The corresponding spatio-temporal distribution of post-injection induced events is well described by the back front (equation 1.11) which accounts for the same hydraulic diffusivity estimate as well as a two dimensional active rock volume.

within a low permeability granitic rock (House, 1987; Fehler, 1989). As a result of the high pressure fluid injection more than 11300 events have been recorded and located (Figure 1.7). The computed  $r - t$  diagram shows the characteristic parabolic signature of the seismicity cloud. Fitting the triggering front (equation 1.10) as envelope of injection phase induced events provides a large scale in-situ rock hydraulic diffusivity estimate of  $D = 0.14 \text{ m}^2/\text{s}$  (see also Parotidis et al., 2004; Shapiro et al., 2005).

However, seismicity has not only been observed during the fluid injection. Meanwhile, numerous field experiments at different globally distributed injection sites are known, where a significant number of events has also been monitored up to several hours to days after termination of the injection. Amongst others, these experiments include for instance Barnett Shale (Shapiro and Dinske, 2009a), Basel (Häring et al., 2008; Dinske et al., 2009; Goertz-Allmann and Wiemer, 2013), the Canyonsands (Fischer et al., 2008), Cooper Basin (Baisch et al., 2006), and also Fenton Hill (Fehler et al., 1998; Parotidis et al., 2004; Langenbruch and Shapiro, 2010). This phenomenon of

post-injection induced seismicity has first been studied by Parotidis et al. (2004). They show that after shut-in,  $r - t$  diagrams of post-injection induced seismicity show a growing parabolic domain of seismic quiescence (see Figure 1.7). To explain this observation and to investigate the nature of post-injection induced seismicity triggering, they also consider a linear diffusional pressure relaxation (as Shapiro et al., 1997, 1999, 2002). However, despite shut-in, the pressure perturbation is still able to increase as a function of time and distance from the injection point. After reaching a certain maximum, the pressure starts to decrease which, in turn, increases the effective normal stress. According to the Mohr-Coulomb failure mechanism (section 1.4 and Figure 1.5), an increase of the effective normal stress shifts the Mohr circle to the right. As a result, pre-existing cracks and fractures become more stable which overall leads to a strengthening of rocks. Consequently, the triggering of seismic events is only possible for positive pore pressure changes. In other words, seismic events can not be triggered at locations where the pressure has already reached its maximum. This minimum distance from the injection point  $r$  at which seismicity is terminated at a given time  $t$  after the end of the fluid injection at  $t_0$  is described by the back front (Parotidis et al., 2004). In other words, the back front separates the spatial seismically active from the inactive domain. For a hydraulically homogeneous and isotropic  $d$ -dimensional space the analytically derived back front is given by the following equation (Parotidis et al., 2004; Shapiro, 2008)

$$r = \sqrt{2 d D t \left( \frac{t}{t_0} - 1 \right) \ln \left( \frac{t}{t - t_0} \right)}. \quad (1.11)$$

Hence, fitting the curve described by equation 1.11 as an envelope of the post-injection aseismic area in the  $r - t$  domain allows to determine a scalar hydraulic diffusivity estimate  $D$ . For the given assumptions this hydraulic diffusivity estimate corresponds to the one provided by the triggering front (see Figure 1.7).

## 1.6 Transition from linear to non-linear fluid-rock interaction

So far, the characterization of rock hydraulic transport properties is based on the assumption of a constant with time and pressure hydraulic transport (i.e. linear pressure diffusion). However, as shown previously, the hypothesis of such a linear fluid-rock interaction is not always valid. This has not only been proven by numerous laboratory experiments in which the strong sensitivity of permeability on pressure has been demonstrated (see section 1.2 and Figure 1.3). Recent field experiments also come to similar conclusions. For example, from intensive hydraulic tests at the Soultz-sous-Forêts hot-dry-rock injection site Cornet et al. (2007) conclude that the assumption of linear pressure diffusion is only valid within a narrow pore pressure window. Additionally, fluid injections like for example hydraulic fracturing

treatments can considerably enhance the permeability (Economides and Nolte, 2000). In such situations permeability becomes a function of the pressure. Consequently, it is not sufficient to assume a constant with time and pressure hydraulic transport.

Motivated by these facts, Shapiro and Dinske (2008) show that the aforementioned process of linear diffusion-based seismicity triggering can be considered as an asymptotic end member of a more general non-linear pressure diffusion. This non-linear diffusional relaxation of the pressure perturbation can be described by combining two fundamental equations. One corresponds to Darcy's law (equation 1.1) which describes the balance of the pressure perturbation and viscous friction force. The other represents the continuity equation which describes the conservation of mass

$$\frac{\partial \phi \rho}{\partial t} = -\nabla \cdot \vec{q} \rho. \quad (1.12)$$

Here,  $\phi$  is the porosity of the rock,  $\rho$  denotes the density of the pore fluid and  $\vec{q}$  its filtration velocity. If the temporal dependence of  $\phi \rho$  is supposed to be proportional to the pressure perturbation than it can be displaced by  $\phi \rho = \rho_0 p S$ , where  $\rho_0$  describes a reference density of the pore fluid and  $S$  a poroelastic compliance (i.e. uniaxial storage coefficient). The combination of both equations 1.1 and 1.12 lead to the following equation

$$\frac{\partial p}{\partial t} = \frac{\rho}{\rho_0 S} \nabla \cdot \left( \frac{\mathbf{k}}{\eta} \nabla p \right), \quad (1.13)$$

which, assuming a spherically symmetric problem in a  $d$ - dimensional space as well as a pressure-dependent hydraulic diffusivity of the form  $D(p) = k(p) \rho(p) / (S \eta \rho_0)$ , can further be simplified to

$$\frac{\partial r^{d-1} p}{\partial t} = \frac{\partial}{\partial r} \left( D(p) r^{d-1} \frac{\partial p}{\partial r} \right). \quad (1.14)$$

This general non-linear diffusion equation includes a pressure-dependent hydraulic diffusivity  $D(p)$ , which basically accounts for a non-linear Darcy's law. At the time of commencing this work, Shapiro and Dinske (2008) proposed to use a general power-law dependent hydraulic diffusivity of the form  $D(p) \propto p^n$ , which later, has been extended to (Shapiro and Dinske, 2009b)

$$D(p(r; t)) = (n + 1) D_0 p^n(r; t). \quad (1.15)$$

Here,  $n$  is the so-called index of non-linearity which controls the grade of non-linearity on the diffusion. In the limit of  $n = 0$  the diffusivity becomes independent of the pressure and equation 1.14 becomes a linear diffusion equation governed by the constant  $D_0$ . For this linear diffusion limit seismicity triggering has been described in the previous section 1.5. This, however, formally requires that  $D_0$  is replaced by  $D$ . If the index of non-linearity is  $n > 0$ , then the diffusivity depends on the pressure. Consequently,

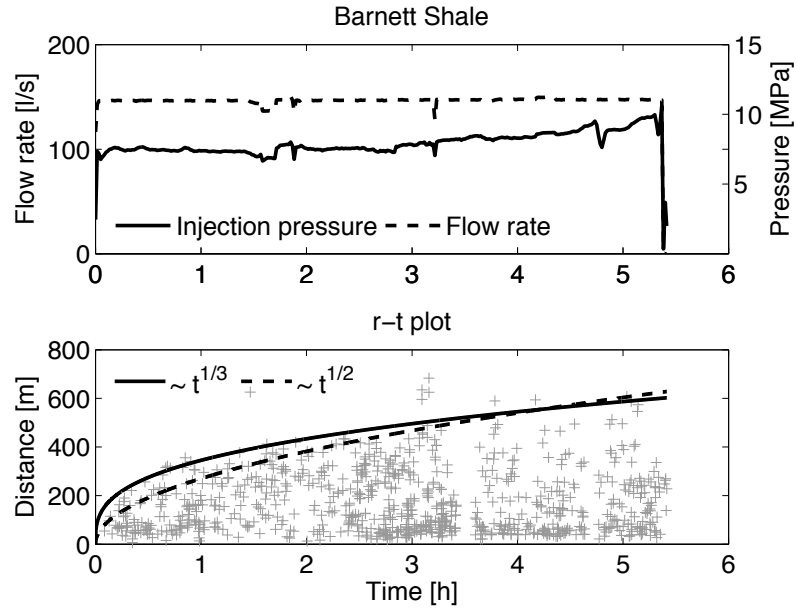


Figure 1.8: Engineering data and  $r - t$  diagram of seismicity being recorded during a hydraulic fracturing treatment in the Barnett Shale, Texas. A cubic root of time dependent triggering front better matches the data compared to a square root envelope (as shown by Shapiro and Dinske, 2008).

$D_0$  becomes a normalizing parameter which should not be interpreted independently. For such a general non-linear diffusional relaxation of the pressure perturbation being governed by a power-law dependent hydraulic diffusivity (equation 1.15) the following relation for the triggering front can be obtained from theoretical considerations (see Shapiro and Dinske, 2009b)

$$r \propto (D_0 Q_I^n t^{n+1})^{\frac{1}{3n+2}}, \quad (1.16)$$

where  $Q_I$  is a constant flow rate of the injection. Considering once more the linear diffusion case of  $n = 0$  the triggering front becomes

$$r \propto \sqrt{D_0 t}. \quad (1.17)$$

This again corresponds to equation (1.10) if  $D_0$  is formally replaced by  $D$ . However, in the other asymptotic limit of a very strong non-linearity, in which  $n \gg 1$ , the triggering front is not any more characterized by a square root but by a cubic root of time dependency

$$r \propto (Q_I t)^{1/3}. \quad (1.18)$$

For seismicity being recorded during a hydraulic fracturing treatment in the Barnett Shale, Shapiro and Dinske (2008) find that such type of a cubic root of time dependent triggering front describes the data better than a square root parabola (Figure 1.8).

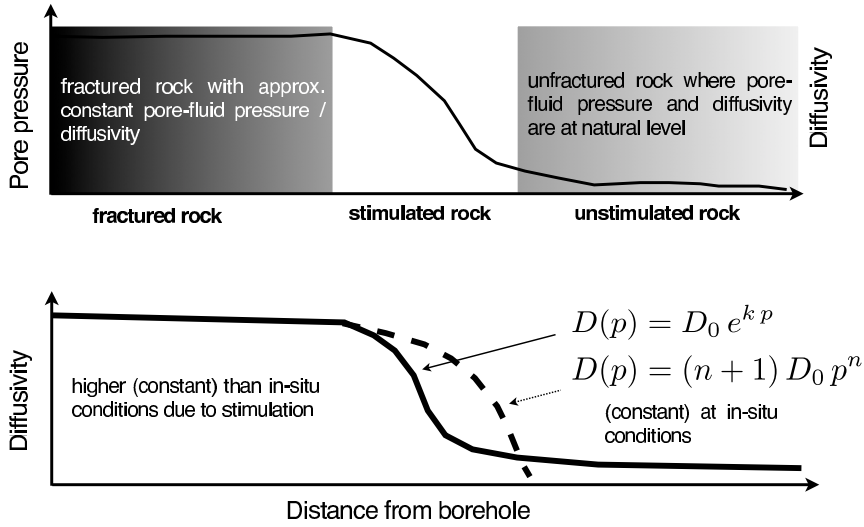


Figure 1.9: Fluid injection-caused distribution of pore pressure and diffusivity as function of the distance from the injection point. Both pressure-dependent diffusivity models are considered to approximate the complicated evolution of hydraulic transport properties during stimulation treatments.

Hence, a non-linear power-law dependent pore pressure diffusion seems to potentially describe seismicity triggering for the situation of a three dimensional hydraulic fracturing with a volumetric opening of pre-existing fractures and fracture networks embedded into an extremely impermeable reservoir rock volume.

Besides the power-law dependent diffusivity relation (equation 1.15), another pressure-dependent diffusivity model has been introduced. Based on the exponential pressure dependence obtained from laboratory experiments (equation 1.3) Hummel and Müller (2008a) propose the following model (see also Müller and Hummel, 2008; Hummel and Müller, 2008b)

$$D(p(r; t)) = D_0 e^{\kappa p(r; t)}, \quad (1.19)$$

where  $\kappa$  again denotes the already introduced permeability compliance. Taking into account this exponential-dependent diffusivity model, they compute pore pressure profiles by solving 1-D and 2-D non-linear diffusion equations. Additionally, they follow the approach of Rothert and Shapiro (2003) and generate synthetic clouds of micro-seismicity which they also analyze in terms of their spatio-temporal characteristics. They find that fitting event clouds with the square root of time dependent triggering front does not allow to conclude that the hydraulic transport is governed by a linear diffusion equation. Distributions of synthetic seismicity based on the exponential-dependent hydraulic transport also show the parabolic character.

## 1.7 Motivation

This thesis provides a comprehensive study about a pressure-dependent hydraulic transport as a model for fluid injection induced earthquakes. For this, both pressure-dependent permeability models will be considered to approximate the complicated stimulation-caused permeability evolution for different rock conditions in the following way (Figure 1.9):

During stimulation including hydraulic fracturing, significant alterations of hydraulic properties occur. These alterations may either be continuous due to the increase of pore pressure or discontinuous due to fracturing. The power-law and exponential relation between pore pressure and permeability is used as a reasonable first order approximation of this complex stimulation-caused permeability evolution. This is motivated by the fact that both models constitute the most rapid pressure increase which, in the case of the exponential relation is even continuous. Simultaneously, both models are also supported by experimental observations from field and laboratory tests.

Integrating numerical simulations and analytical findings, this thesis will provide an extensive investigation on both pressure-dependent permeability models and their impact on the physics and nature of fluid injection induced seismicity triggering. In this way, important open question and problems concerning media with pressure-dependent transport properties will be addressed, such as the following ones:

Is the SBRC approach generally still applicable? What type of diffusivity estimates are provided by the triggering front and the back front? How suitable are the exponential and the power-law model with respect to real injection experiments? How can these models help to improve the stimulation design? What does post-injection induced seismicity tell us about the medium behaviour?

## 1.8 Outline of this thesis

The results obtained during the development of this thesis led to two major publications in *Geophysical Journal International* and *Geophysics* as well as one manuscript which recently has been submitted to *Geophysical Prospecting*. These works hereinafter are referred to as chapters which are briefly introduced in the following.

### Chapter 2

First, a numerical modelling study will be presented. This study aims to explore what type of diffusivity estimates the triggering front provides if the relaxation of the pressure perturbation is governed by non-linear diffusion. For this, the power-law and the exponential pressure-dependent diffusivity model are taken into account. For 1-, 2- and 3-D media non-linear diffusion equations are solved for different pressure depen-

dencies. For the computed pressure fields,  $r-t$  diagrams of synthetic event catalogues are generated and analyzed in terms of their spatio-temporal characteristics.

### Chapter 3

Theoretical relations have shown that a power-law dependent hydraulic transport can lead to a triggering front which is not characterized any more by a square root but by a cubic root of time dependency. Such a behaviour has been observed for seismicity induced during a hydraulic fracturing treatment in the Barnett Shale. Hence, this chapter focuses on the power-law diffusion model and its applicability to hydraulic fracturing induced seismicity. A scaling approach based on a factorized anisotropy and non-linearity is presented which allows to determine the principal components of the permeability tensor. A numerical workflow is presented to compute calibrated flow-rate based pressure profiles. Following this modelling approach synthetic seismicity is generated whose spatio-temporal features are similar as the ones observed in Barnett Shale. The comparison of real and synthetic seismicity even allows to determine and quantify the influence of the pressure dependence.

### Chapter 4

So far, the analysis of spatio-temporal characteristics is focused on the injection phase. However, even after termination of the fluid injection seismic activity can still be monitored for several hours to days. This chapter examines the question what type of diffusivity estimate the back front provides for the more general assumptions of a pressure-dependent hydraulic transport in anisotropic rocks. The aforementioned transformation approach is further generalized to account for any unknown non-linear fluid-rock interaction. Moreover, it is applied to microseismic data from the Ogachi and Fenton Hill fluid injection experiment. The analysis of spatio-temporal characteristics shows that the back front provides an estimate for the minimum principal component permeability tensor. However, as for the triggering front, it is also shown that the temporal dependence of the back front can deviate from the linear diffusion signature. To explore if non-linear pressure diffusion can explain these signatures a numerical modelling is performed. Following chapter 2 both the power-law and the exponential dependent diffusivity model are considered. To account for a post-injection enhanced hydraulic state of the rock a new model of a so-called frozen medium diffusivity is introduced. Following this modelling synthetic seismicity is generated whose spatio-temporal back front features coincide with the ones observed in real data.

### **Perspectives**

Not all ideas that have come up during the course of this thesis could be considered here. However, these ideas represent interesting and promising directions of future research as they will contribute to improve our understanding of the physics of fluid injections and associated earthquakes. Several thoughts will be addressed which could serve as initial step of possible future work.

### **APPENDIX A: SUPPLEMENTARY STUDY**

Finally, another industrial data set is considered. This data set has been provided by an anonymous sponsor of the *PHASE* consortium. It contains a total number of 231 microseismic events which have been recorded during and after a three stage hydraulic fracturing treatment of an unconventional reservoir. However, due to this low number of induced events the data statistics is not sufficient enough to apply the here presented analysis of spatio-temporal characteristics. Additionally, the distribution of induced events indicates that the geometry of the hydraulic fracture can not be considered as a three dimensional volumetric hydraulic fracture. Consequently, this data set could not be considered and analyzed in a way similar to the Barnett Shale (chapter 3). Therefore, this data set has been alternatively analyzed and interpreted in the frame of the hydraulic fracturing interpretation of the *SBRC* approach. This method aims to determine fracture geometry, fluid loss as well as scalar magnitude estimates of rock hydraulic transport properties.



## Chapter 2

# Microseismic estimates of hydraulic diffusivity in case of non-linear fluid-rock interaction <sup>1</sup>

---

<sup>1</sup>This article has been accepted for publication in *Geophysical Journal International* ©: N. Hummel and S. A. Shapiro (2012). Microseismic estimates of hydraulic diffusivity in case of non-linear fluid-rock interaction. 188(3), 1441-1453, <http://dx.doi.org/10.1111/j.1365-246X.2011.05346.x>. Published by Oxford University Press on behalf of The Royal Astronomical Society and Deutsche Geophysikalische Gesellschaft. All rights reserved.

## Summary

As a rule, rock stimulation by fluid injection induces microearthquakes. Assuming that pore-fluid pressure diffusion is responsible for this phenomenon one can use seismicity to estimate the hydraulic properties of rocks. Previously, for the estimation of hydraulic transport properties from the triggering front it has been assumed that they are independent of time and pressure. However, fluid injections can strongly change permeability of rocks (e.g. hydraulic fracturing). In this paper, we investigate what kind of diffusivity estimates are provided by the triggering front in cases where hydraulic transport properties are functions of pore-fluid pressure (i.e. they are changing during the injection). In this case the pressure relaxation results in a non-linear pore-fluid pressure diffusion associated with heterogeneously and time dependent distributed permeability. We consider numerically two models of pressure-dependent hydraulic diffusivity, a power-law- and an exponential law. We generate synthetic microseismicity by solving corresponding 1-, 2- and 3-D non-linear diffusion equations. Our results show that the triggering front provides reasonable estimates of the effective diffusivity approximately corresponding to the hydraulic diffusivity resulting from the stimulation (including hydraulic fracturing) of rocks and thus constitute a significant conceptual update of the seismicity-based reservoir characterization approach.

## 2.1 Introduction

Fluid injections through a borehole into the surrounding rock are frequently used for the development of hydrocarbon as well as geothermal reservoirs. Such operations are performed for enhancing hydrocarbon recovery (Economides and Nolte, 2000) or for creation of Enhanced Geothermal Systems (Majer et al., 2007) and are accompanied by microseismic activity. Here, we follow the approach formerly introduced by Shapiro et al. (1999, 2002) who showed that a diffusional pore-fluid pressure relaxation (i.e. linear fluid-rock interaction) can explain the spatio-temporal characteristics of the observed microseismic activity. Assuming linear pore-fluid pressure diffusion they introduce the so-called SBRC approach (Seismicity-Based Reservoir Characterization) showing that the field-scale hydraulic diffusivity tensor can be estimated from the spatio-temporal distribution of observed microseismicity.

In this paper we extend the SBRC approach to the case where non-linear diffusion is considered to be responsible for triggering seismicity. Like Shapiro and Dinske (2009b) as well as Hummel and Müller (2009) we take into account a hydraulic diffusivity which depends on the pore-fluid pressure. However, in contrast to these two works, we investigate what is the character of the diffusivity that controls the triggering front of fluid injection induced seismicity. We numerically solve non-linear diffusion equations to derive pore-fluid pressure distributions. We subsequently compare the pore-fluid pressures with randomly distributed values of critical pressure assumed to be necessary to trigger seismicity. In this way we define synthetic microseismic events. We analyze the spatio-temporal characteristics of the event clouds in the  $r - t$  domain, where  $r$  is the distance between event location and the injection point as function of the elapsed time  $t$  since beginning of the injection (so-called  $r - t$  plot). We compare diffusivity values derived from two different methods, a heuristic and a computational one. First, we follow the SBRC approach and fit the triggering front parabola to the entire microseismic data set to obtain a heuristic estimate of hydraulic diffusivity. We then compare this diffusivity estimate using a computational method where we calculate the effective diffusivity for a heterogeneous medium created by the non-linear pressure diffusion. Note that in our computation we assume a monotonous increase of pressure in the medium which leads to an increase of the diffusivity. Thus, the largest diffusivity corresponds to the last moment of the injection. This maximal created diffusivity we denote as diffusivity after stimulation.

In the present study we address the question whether the SBRC approach is still applicable to induced seismicity and what kind of hydraulic diffusivity estimates will be provided by the triggering front if the pore pressure diffusion is significantly non-linear.

## 2.2 Methodical background

### 2.2.1 From linear to non-linear fluid-rock interaction

In recent years the interest in fluid injection-induced microseismicity has grown considerably. Using microseismicity in reservoir characterization has become an important tool in the exploration industry. One way of explaining the occurrence of fluid injection-induced microearthquakes is based on a diffusional pore-fluid pressure relaxation induced by the fluid injection (Talwani and Acree, 1985; Shapiro et al., 1997, 1999).

The fluid injection causes an increase of fluid pressure within the connected pore space of the rock. Raleigh et al. (1972) observe that such a rise of pore-fluid pressure can lead to microseismic activity. Pearson (1981) further discusses the relationship between microseismicity and high pore pressures during hydraulic stimulation experiments and conclude that the induced events seem to be caused by shear failure. As a result of hydraulic stimulation the pore-fluid pressure increases which in turn reduces the effective normal stress. Such a reduction of the effective normal stress can lead to rock sliding along pre-existing sub-critically stressed cracks inducing microseismic events (see also Zoback and Harjes, 1997).

Within the SBRC approach Shapiro et al. (1999, 2002) introduce a technique to obtain the in-situ hydraulic diffusivity of the formation using induced microseismicity. Assuming that the pore-fluid pressure relaxation is governed by a constant hydraulic diffusivity (linear fluid-rock interaction) they show that the field-scale hydraulic diffusivity tensor can be estimated from the spatio-temporal distribution of observed microseismicity. The estimation of the hydraulic diffusivity uses the concept of the so-called 'triggering front'. The triggering front provides an approximate outermost envelope of the distances between event locations and the injection point  $r$  as function of the time  $t$  elapsed since beginning of injection ( $r - t$  plot). For a homogeneous and isotropic medium the triggering front is approximately given by

$$r = \sqrt{4\pi Dt}, \quad (2.1)$$

where  $D$  is the scalar hydraulic diffusivity. Shapiro et al. (1997, 1999, 2002) apply the triggering front to several data sets (KTB, Soultz-sous-Forêts, Fenton Hill) and conclude that the SBRC approach provides estimates of hydraulic diffusivity before the stimulation of the rock. Based on the hydraulic diffusivity estimates obtained from the triggering front and the knowledge of poroelastic parameters they furthermore show that the order of magnitude of estimates of hydraulic permeability is in good agreement with independent results.

However, one has understood that the assumption of linear pore-fluid pressure diffusion resulting from a hydraulic diffusivity being independent of pressure is not always

valid. Cornet et al. (2007) conclude from hydraulic tests at the Soultz-sous-Forêts hot-dry-rock site that this assumption is only valid within a restricted pore-fluid pressure window. Laboratory experiments show that the pore-fluid pressure can have a strong impact on the fluid transport properties. Brace et al. (1968) as well as Li et al. (2009) show the significant influence of effective pressure on permeability of granite samples as well as tight gas sandstone samples. Yilmaz et al. (1994) study pore-fluid pressure distribution in fractured and compliant rocks by simulating 1-D pore-fluid pressure profiles with a pressure-dependent permeability. Based on laboratory studies their suggested model shows an exponential relation of permeability on pore-fluid pressure.

On that basis Hummel and Müller (2009) simulate and analyze synthetic clouds of 1- and 2-D microseismicity triggered by a non-linear pore-fluid pressure diffusion using an exponential dependence of diffusivity on pore-fluid pressure

$$D(p(r; t)) = D_0 e^{\kappa p(r; t)}. \quad (2.2)$$

The background medium diffusivity is denoted by  $D_0$ ,  $p$  is the pore-fluid pressure perturbation and  $\kappa$  is the so-called permeability compliance. For large  $\kappa$ , the hydraulic diffusivity will depend strongly on the pressure. For  $\kappa = 0 \text{ Pa}^{-1}$ , the pressure relaxation will be described by a linear diffusion equation. For the permeability compliance  $\kappa$  Hummel and Müller (2009) report values ranging from 0 ... 40  $\text{GPa}^{-1}$  for sandstones and values up to 500  $\text{GPa}^{-1}$  for fractured rocks (see also Daley et al., 2006). Millich et al. (1998) state that for the KTB site the evolution of the in-situ permeability with effective pressure can be described by an exponential relation including a permeability compliance value of 140  $\text{GPa}^{-1}$ .

Based on the philosophy of a diffusional pore-fluid pressure relaxation Shapiro and Dinske (2009b) extend the SBRC approach to non-linear diffusion describing the phenomena of microseismic triggering. They argue that fluid-induced seismicity can occur due to a wide range of processes within two extrema. The one corresponds to stimulation experiments in liquid-saturated rocks with a small-to-modest permeability where the injection pressure is smaller than the minimum principal tectonic stress. In this regime the triggering of microseismicity can be caused by nearly linear diffusion of pore-fluid pressure (linear fluid-rock interaction). The other extremum corresponds to non-linear fluid-rock interaction describing the strong increase of hydraulic transport properties that corresponds to hydraulic fracturing experiments. Such operations are used to actively destroy low-permeability rock masses in order to create highly permeable fracture sets. If fluid is injected into the formation through a perforated well much faster than it can escape into the surrounding rock there is a pressure built-up. At some point the increasing pressure exceeds a certain threshold level and the formation breaks resulting in an opening of tensile 'hydraulic' fractures. In these situations the initial permeability of non-fractured (virgin) rocks can be nearly neglected.

For such a non-linear behaviour Shapiro and Dinske (2009b) propose to use a power-law dependence of diffusivity on pore-fluid pressure

$$D(p(r; t)) = (n + 1) D_0 p^n(r; t), \quad (2.3)$$

where  $n$  is the measure or index of non-linearity. For large  $n$ , the hydraulic diffusivity will depend strongly on the pressure. For  $n = 0$ , the pressure relaxation will be described by a linear diffusion equation with the diffusivity  $D_0$ . Shapiro and Dinske (2009b) show, for example, a case study from Barnett Shale which seems to be well described by such a model.

Mathematically, the permeability compliance  $\kappa$  and the index of non-linearity  $n$  will describe and control the influence of non-linearity on the governing diffusion equation. Physically,  $\kappa$  and  $n$  are properties of the reservoir. Depending on their magnitude they describe a strong pore-fluid pressure dependent diffusivity (equation 2.2 and 2.3) and therefore characterize the fluid-rock interaction of the reservoir. What is the effective diffusivity that controls the propagation of the seismicity front in such a medium? What kind of hydraulic diffusivity estimates does the triggering front provide if hydraulic transport properties are functions of pore-fluid pressure? To answer these questions is the focus of our study.

### 2.2.2 Modelling non-linear pore-fluid pressure diffusion

In our modelling we approximate a real configuration of a fluid injection into a borehole by a point source of pore-fluid pressure perturbation into an initially hydraulically homogeneous and isotropic fluid-saturated medium. The medium is large enough to neglect the interaction of the pore-fluid pressure perturbation with the boundary in the considered time. The spatio-temporal evolution of the pore-fluid pressure perturbation induced by the fluid injection is described according to Shapiro and Dinske (2009b) by the following non-linear diffusion equation:

$$\frac{\partial r^{d-1} p}{\partial t} = \frac{\partial}{\partial r} \left( D(p) r^{d-1} \frac{\partial p}{\partial r} \right). \quad (2.4)$$

This equation is obtained by combining the continuity equation expressing the fluid mass conservation with the Darcy law describing the balance of pore-fluid pressure perturbation and viscous friction force. We neglect anisotropy and consider a spherically symmetric diffusion in a  $d$ -dimensional space where  $r$  describes the radial distance from the injection point. As one can see, equation (2.4) takes into account an arbitrary functional dependence  $D(p)$  of the hydraulic diffusivity on pore-fluid pressure  $p$ . For this functional dependence  $D(p)$  we use the exponential as well as the power-law relation introduced in equation (2.2) and equation (2.3).

In order to obtain the particular spatio-temporal pore-fluid pressure evolution we solve equation (2.4) using finite element methods. Note that the non-linear equation is carried over into a linear diffusion equation for  $\kappa = 0 \text{ Pa}^{-1}$  and  $n = 0$ . Thus, the limit of linear fluid-rock interaction is also included in our modelling.

We use boundary and initial conditions corresponding to a pressure source of magnitude  $p_0$  at the injection point applied instantaneously at  $t = 0$  and remaining constant for all times  $t \geq 0$ :

$$p(r; t < 0) = 0, \quad p(r = 0; t \geq 0) = p_0. \quad (2.5)$$

In the numerical modelling scheme we implement the fluid injection as a Dirichlet-type boundary condition with a constant injection pressure of  $p_0 = 10 \text{ Pa}$ . Therefore, the values of the permeability compliances  $\kappa$  are normalized to the order of  $10^{-1} \text{ Pa}^{-1}$  (according to Yilmaz et al., 1994). For example, for a typical injection pressure of 10 MPa the permeability compliance value of  $\kappa = 140 \text{ GPa}^{-1}$  at the KTB site (Millich et al., 1998) is rescaled to a value of  $0.14 \text{ Pa}^{-1}$  for an injection pressure of 10 Pa. In the same way a permeability compliance value of  $\kappa(p_0 = 10 \text{ MPa}) = 500 \text{ GPa}^{-1}$  (corresponding to a highly fractured rock, Daley et al., 2006) is rescaled to a value of  $\kappa(p_0 = 10 \text{ Pa}) = 0.5 \text{ Pa}^{-1}$ . For the initial background diffusivity  $D_0$  in (2.2) and (2.3) we use a value of  $1 \text{ m}^2 \text{ s}^{-1}$ . Based on the permeability compliance values reported by Hummel and Müller (2009) we use values of  $\kappa = 0, 0.2, 0.4$  and  $0.5 \text{ Pa}^{-1}$ . For the indices of non-linearity  $n$  we use  $n = 0, 1, 2$  and  $3$ .

### 2.2.3 Simulation of synthetic microseismicity

We generate synthetic microseismic event clouds according to the approach of Rothert and Shapiro (2003) and Hummel and Müller (2009). The fluid injection causes the pore-fluid pressure in the rock to increase. This increase in turn decreases the effective normal stress which can lead to a seismic event (Zoback and Harjes, 1997; Bruehl, 2007). The triggering of a seismic event is defined by comparing the pressure perturbation with a synthetic field of randomly distributed critical pressures. We assume that there are pre-existing and randomly distributed critically stressed cracks. To simulate the strength of these cracks the medium is subdivided into cells. Each cell corresponds to a center of a single crack and is characterized by a certain critical pore pressure value  $C$  representing the required pressure perturbation which brings the rock to failure. The value  $C$  is called criticality in the following. Small  $C$ - values correspond to weak cracks, large  $C$ - values correspond to stable cracks. The values of the criticality field  $C$  are equally distributed between  $C_{\min}$  and  $C_{\max}$ . We set the lower bound of  $C$  to  $C_{\min} = 0 \text{ Pa}$ . We restrict the upper bound of  $C$  to the order of the injection source magnitude  $p_0$  and set  $C_{\max} = 10 \text{ Pa}$ . Therefore the critical pore-fluid pressure values are broadly distributed which corresponds to reality (see for example Rothert and Shapiro, 2007). An event is triggered if the pore-fluid pressure exceeds the local criticality value,

$$p(r; t) > C(r). \quad (2.6)$$

The triggering process is confined such that once the pore-fluid pressure exceeded criticality at a certain location the triggering of a later microseismic event is not possible. This constraint excludes the possibility that the rock mass experiences some kind of 'healing'. It approximates the fact that the necessary time for tectonic reloading is much larger compared to the time for the diffusion process of pore-fluid pressure perturbation.

### 2.2.4 Triggering fronts in non-linear media

Following the SBRC approach in the case of a linear fluid-rock interaction the fitting of the triggering front to the upper bound of observed microseismicity provides a large-scale hydraulic diffusivity of the rock (Shapiro et al., 2002). Our aim is to understand what kind of diffusivity estimates a  $r - t$  plot provides in the case of non-linear fluid-rock interaction. Hence, we fit a triggering front parabola to the farthest events of the particular synthetic microseismic event clouds. As a result we obtain a heuristic diffusivity value  $D_h$ .

To explore the behaviour of the triggering front in the case of non-linear fluid-rock interaction defined by equation (2.4) (using 2.2 or 2.3 and 2.5) we start with a dimensional analysis (see for example Barenblatt, 1996). Note that the initial and boundary condition problem we consider here differs from those of Shapiro and Dinske (2009b). In this study we define a constant-pressure boundary problem (see eq. 2.5) while Shapiro and Dinske (2009b) investigate the problem of boundary conditions simulating fluid injection rates.

For the exponential diffusion model (equation 2.2) the relaxation radius  $r_t$  (we will identify  $r_t$  with the triggering front) of the pore-fluid pressure perturbation  $p$  depends on the quantities  $p_0$ ,  $t$ ,  $D_0$ ,  $s_0$  and  $\kappa$ . Here  $s_0$  describes the surface of an effective injection source cavity. Although we theoretically consider the case of a point-injection source, the size of the injection source cavity in our modelling corresponds to the size of the first finite element. The dimensions of these quantities are

$$[p_0] = P, \quad [t] = T, \quad [D_0] = \frac{L^2}{T}, \quad [s_0] = L^2, \quad [\kappa] = \frac{1}{P}. \quad (2.7)$$

$L$ ,  $T$  and  $P$  denote physical dimensions of length, time and pressure. We can construct two dimensionless quantities,  $\Theta_{e1}$  and  $\Theta_{e2}$ :

$$\Theta_{e1} = \frac{D_0 t}{s_0}, \quad (2.8)$$

$$\Theta_{e2} = \kappa p_0. \quad (2.9)$$

$\Theta_{e1}$  describes the influence of time  $t$  and of the surface of the effective injection source cavity  $s_0$ .  $\Theta_{e2}$  describes the experimental setup and depends only on the medium

parameters as well as on the injection source magnitude. Then, the relaxation radius must have the form

$$r_t = \sqrt{D_0 t} f_e(\Theta_{e1}, \Theta_{e2}), \quad (2.10)$$

where  $f_e$  is a function of the variables  $\Theta_{e1,2}$ .

For the power-law diffusion model (equation 2.3) the dimensional analysis works in the same way. The relaxation radius of the pore-fluid pressure perturbation  $p$  depends on the quantities  $p_0$ ,  $t$ ,  $D_0$ , and  $s_0$ . The dimensions of these parameters are

$$[p_0] = P, \quad [t] = T, \quad [D_0] = \frac{L^2}{T P^n}, \quad [s_0] = L^2. \quad (2.11)$$

With these quantities we can construct one dimensionless quantity  $\Theta_{p1}$ :

$$\Theta_{p1} = \frac{D_0 t p_0^n}{s_0}. \quad (2.12)$$

Hence the relaxation radius has the form

$$r_t = \sqrt{D_0 p_0^n t} f_p(\Theta_{p1}), \quad (2.13)$$

where  $f_p$  is a function of the variable  $\Theta_{p1}$ . For both, the exponential - and power-law diffusivity models, the strength of the injection source is given by a surface force density, i.e. pressure.

In 1-D the injection source represents a surface of a half-space. The pressure is distributed along an infinite vertical plane intersecting the distance-axes at the origin. Therefore, the surface area  $s_0$  of the effective injection source becomes infinite large,  $s_0 \rightarrow \infty$ . As a result, the quantity  $\Theta_{e1}$  goes to zero,  $\Theta_{e1} \rightarrow 0$ . Thus, for the exponential diffusion model, the pressure fronts (and, therefore, triggering fronts) are given by

$$r_t \propto \sqrt{D_0 t} f_e(0, \kappa p_0), \quad (2.14)$$

where  $f_e(0, \kappa p_0)$  denotes a function for the limit of  $\Theta_{e1} \rightarrow 0$  and of the parameters  $\kappa p_0$  (i.e.  $\Theta_{e2}$ ). For the power-law diffusion model, the triggering fronts in 1-D are given by

$$r_t \propto \sqrt{t D_0 p_0^n} f_p(0), \quad (2.15)$$

where  $f_p(0)$  is a function for the limit of  $\Theta_{p1} \rightarrow 0$ . In equations (2.14) and (2.15) we assume that the corresponding limits exist. For both models describing non-linear fluid-rock interaction relation (2.14) and (2.15) show a  $\sqrt{t}$ -dependence of the triggering front.

In 2-D the situation is similar. The pressure is distributed across the surface of an infinitely extended cylinder so that  $s_0 \rightarrow \infty$ . This cylinder is vertical to the plane in

which pore-fluid pressure diffusion takes place. As a result  $\Theta_{e1} \rightarrow 0$  and  $\Theta_{p1} \rightarrow 0$ . Thus, triggering fronts for both exponential diffusion model and power-law diffusion model are also described by relations (2.14) and (2.15).

For pore-fluid pressure diffusion in 3-D the pressure is now distributed across the surface area of an effective injection source cavity of a finite radius  $r_0$ . In this case the surface area is limited and does not approach infinity. Moreover, we are interested in a solution for a point injection source, i.e.  $s_0 \rightarrow 0$ . Therefore, we are looking for the asymptotic behaviour of both functions  $f_e(\Theta_{e1}, \Theta_{e2})$  and  $f_p(\Theta_{p1})$  in the limits  $\Theta_{e1} \rightarrow \infty$  and  $\Theta_{p1} \rightarrow \infty$ . For such situations it is more difficult to derive a relation for the triggering front. According to Barenblatt (1996) it is possible that the limits of  $f_e(\Theta_{e1})$  and  $f_p(\Theta_{p1})$ , if they exist, will become either constant or power-law dependent. For the exponential diffusion model we will later numerically demonstrate a  $\sqrt{t}$ -dependent triggering front. Therefore,  $\Theta_{e1}$  is a constant. However, for the power-law diffusion model, our results will show that  $\Theta_{p1}$  depends on an exponent  $m$  so that

$$f_p(\Theta_{p1}) = \left( \frac{D_0 t p_0^n}{s_0} \right)^m. \quad (2.16)$$

In section 2.4 we will return to discuss the relation for the triggering front for the 3-D power-law model in more details.

### 2.2.5 Effective diffusivity

In order to interpret the estimates of heuristic diffusivity obtained from the triggering front we introduce the effective diffusivity. We assume that the diffusivity will not decrease after the stop of the injection. Otherwise we have to consider the so-called back front of seismicity (Parotidis et al., 2004). The fluid injection creates a medium with an increased heterogeneously distributed diffusivity. With the last moment of the injection phase the fluid injection has caused the maximal impact on hydraulic diffusivity which we attempt to represent by an effective diffusivity. This effective diffusivity value is computed for the already stimulated (including hydraulically fractured) medium and represents the corresponding enhanced diffusivity value in a replacing homogeneous medium. The replacement of a heterogeneously distributed diffusivity by a single effective diffusivity value is designed in such a way that the position of a triggering front in the replacing homogeneous medium would approximately coincide with its actual position.

For a steady state one dimensional flow perpendicular to a horizontally layered medium with equal layer thicknesses  $\delta$  the effective diffusivity is calculated according

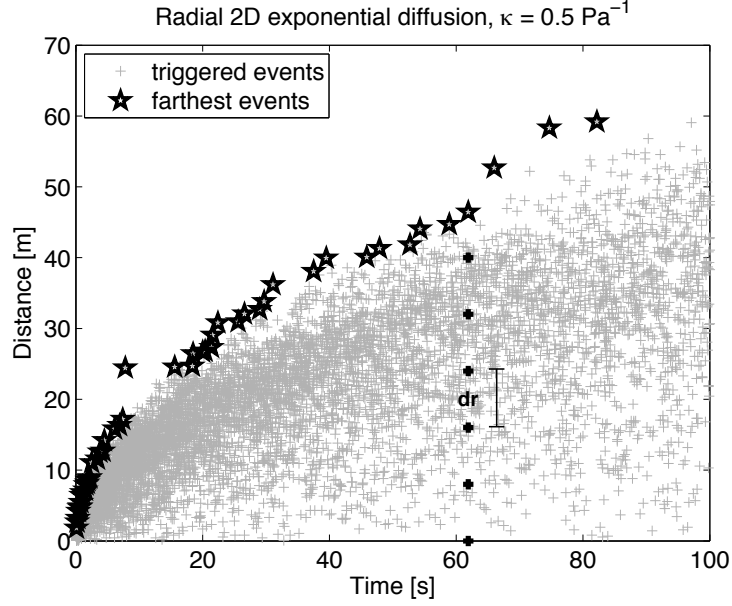


Figure 2.1: Illustration about how we calculate the effective diffusivity of a medium which was stimulated by a non-linear pressure diffusion. This example shows the so-called  $r - t$  plot of microseismic events (grey crosses) based on 2-D exponential pore-fluid pressure diffusion with  $\kappa = 0.5 \text{ Pa}^{-1}$  which have been triggered according to the procedure explained in section 2.2.3. In such a  $r - t$  plot the farthest triggered events (black stars) define the location of the triggering front. For a certain time  $t_{fe}$  the distance of the farthest event from the injection point  $r_{fe}$  is subdivided into equidistant intervals  $dr$ . For this particular time  $t_{fe}$  and distances  $dr$  the corresponding pore-fluid pressure  $p(r; t_{fe})$  is inserted into equation (2.18) in order to calculate the effective diffusivity  $D_{\text{eff}}(r; t_{fe})$ . For all farthest events this calculation leads to a distribution of  $D_{\text{eff}}$ - values which is shown in Figure 2.2.

to (see for example Freeze and Cherry, 1979)

$$D_{\text{eff}} = \frac{\delta_{\text{total}}}{\sum_{i=1}^N \frac{\delta_i}{D_i}} = \left[ \frac{1}{D_1} + \frac{1}{D_2} + \dots + \frac{1}{D_N} \right]^{-1} \frac{\delta_{\text{total}}}{\delta}. \quad (2.17)$$

In this equation  $D_1$ ,  $D_2$  and  $D_N$  denote the diffusivities of the first, second and  $N^{\text{th}}$  layer, whereas  $\delta_{\text{total}}$  describes the overall thickness of the stratified medium. For a particular synthetic microseismic event cloud we calculate the effective diffusivity in the following way. The position of the triggering front describing the envelope of seismicity is defined by the farthest triggered events which are characterized by a certain occurrence time  $t_{fe}$  and distance from the injection point  $r_{fe}$ . For each single farthest event we subdivide its distance from the injection point  $r_{fe}$  into equidistant intervals  $dr$  (Figure 2.1). This spatial subdivision provides an equivalent to the horizontally layered medium. For this particular occurrence time  $t_{fe}$  and all discrete distances from

the injection point  $dr$  we pick up the corresponding pore-fluid pressure  $p(r; t_{fe})$  from the calculated pore-fluid pressure evolution. We insert these pressure values into the appropriate pressure-dependent diffusivity model (equation 2.2 or 2.3) to calculate the effective diffusivity value for this particular farthest triggered event according to

$$D_{\text{eff}}(r_{fe}; t_{fe}) = \left[ \frac{1}{r_{fe}} \int_0^{r_{fe}} \frac{1}{D(p(r; t_{fe}))} dr \right]^{-1}. \quad (2.18)$$

Obviously, if we do not take into account one single farthest event but consider all farthest triggered events of the  $r - t$  plot and if we further calculate the effective diffusivity for each of these events according to equation (2.18) then we will obtain a distribution of effective diffusivity values (Figure 2.2). Before the shut-in of the injection source the last  $D_{\text{eff}}$  value represents the final state of the enhanced diffusivity which results from the hydraulic stimulation. At the same time it corresponds to the maximal impact of the fluid injection on the medium. This largest created diffusivity we denote as diffusivity after stimulation. We insert the last  $D_{\text{eff}}$  value into equation (2.1) to have a comparison to the parabola which uses the single heuristic diffusivity estimate. Therefore, we obtain an 'effective diffusivity parabola' which reads

$$r_{\text{eff}} = \sqrt{4 \pi D_{\text{eff, last}} t}. \quad (2.19)$$

## 2.3 Results

### 2.3.1 Solutions for the pore-fluid pressure

As a result of our modelling we first obtain the spatio-temporal pore-fluid pressure evolutions as solutions of the corresponding non-linear diffusion equation. In the following we analyze these pore-fluid pressure profiles obtained for different permeability compliances  $\kappa$  and indices of non-linearity  $n$ .

For non-linear fluid-rock interaction the pressure perturbation penetrates much deeper into the medium compared to linear fluid-rock interaction driven by  $D_0$  (Figure 2.3). This effect becomes more distinct with increasing non-linearity. It is caused by the pressure enhanced hydraulic diffusivity which strongly increases due to the dependence of pore-fluid pressure on the index of non-linearity  $n$ . As a result the pressure perturbation is able to penetrate a larger distance within the same time compared to the linear diffusion case. In addition, for increasing influence of non-linear fluid-rock interaction, the shape of the pore-fluid pressure profiles changes from a concave-shaped profile to a more and more convex-shaped profile. This behaviour is independent of the diffusion model and quite distinct in 1- and 2-D.

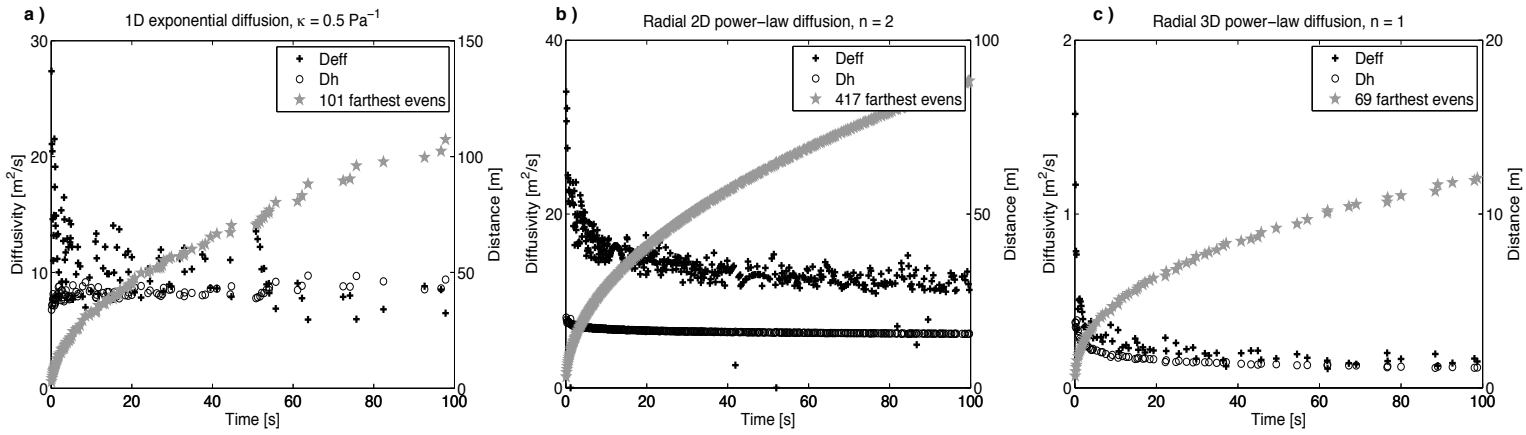


Figure 2.2: Three examples showing the farthest triggered events (stars) together with their corresponding calculated effective diffusivity values (crosses). For comparison we also added the heuristic diffusivity estimates (circles) which are obtained using equation (2.1) for each farthest triggered event. Compared to the heuristic diffusivity estimates the calculated effective diffusivity values are broader distributed. The reason is that according to equation (2.18) the calculation of  $D_{\text{eff}}$  depends on different pore-fluid pressures. As a result of the stimulation experiment the fluid injection causes an enhanced hydraulic diffusivity. At the end of the injection phase the final state of the enhanced diffusivity is represented by the the last effective diffusivity value.

## 2 Microseismic estimates of hydraulic diffusivity in case of non-linear fluid-rock interaction

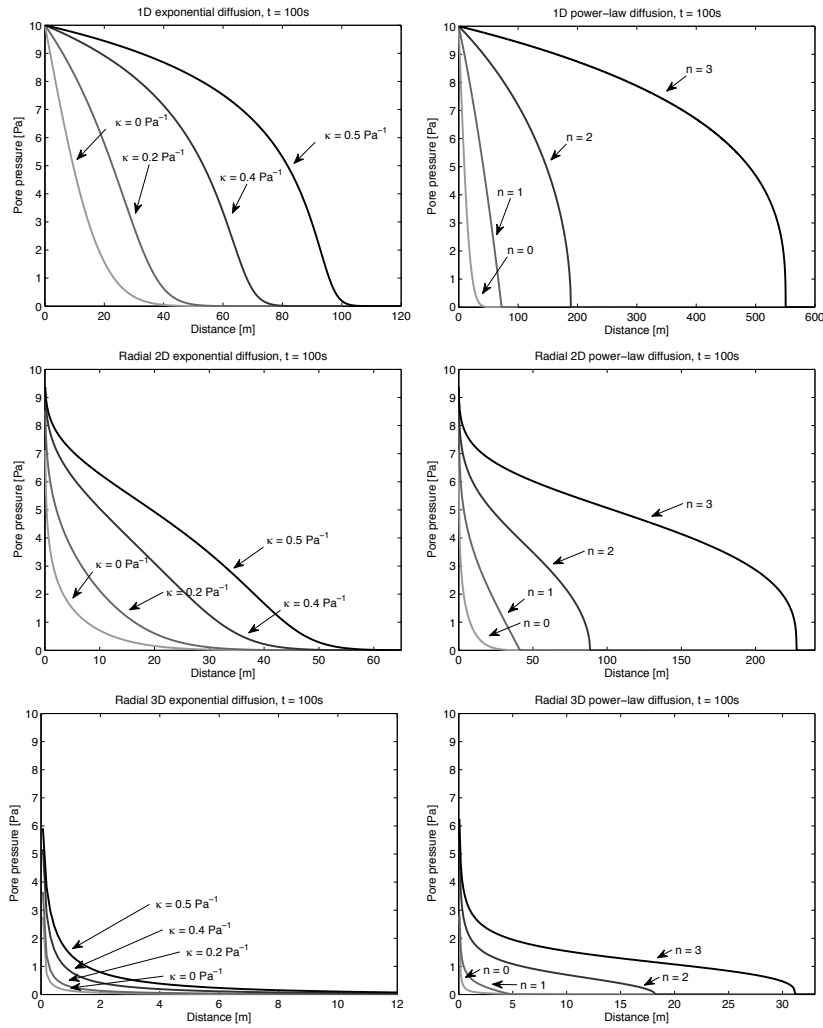


Figure 2.3: Snapshots of pore-fluid pressure profiles for different permeability compliances  $\kappa$  and indices of non-linearity  $n$  after  $t = 100$  s of injection. The left column shows the profiles for the exponential relation in 1-, 2- and 3-D. The right column shows the profiles for the power-law relation, also for 1-, 2- and 3-D media. For  $\kappa > 0 \text{ Pa}^{-1}$  and  $n > 0$  hydraulic diffusivity becomes pressure-dependent and increases strongly (see Figure 2.4). As a result the pore-fluid pressure profiles penetrate deeper into the medium compared to linear diffusion ( $\kappa = 0 \text{ Pa}^{-1}$  and  $n = 0$ ). Due to additional dimension the pore-fluid pressure profiles in 2-D and 3-D are characterized by a large pressure drop in the vicinity of the injection point (geometrical spreading). Comparing the profiles from both pressure-dependent models one can see that the tips of the profiles look different. For the exponential model the pore-fluid pressure profiles are characterized by a smooth transition at the pressure heads. For the power-law model the pressure drops to zero.

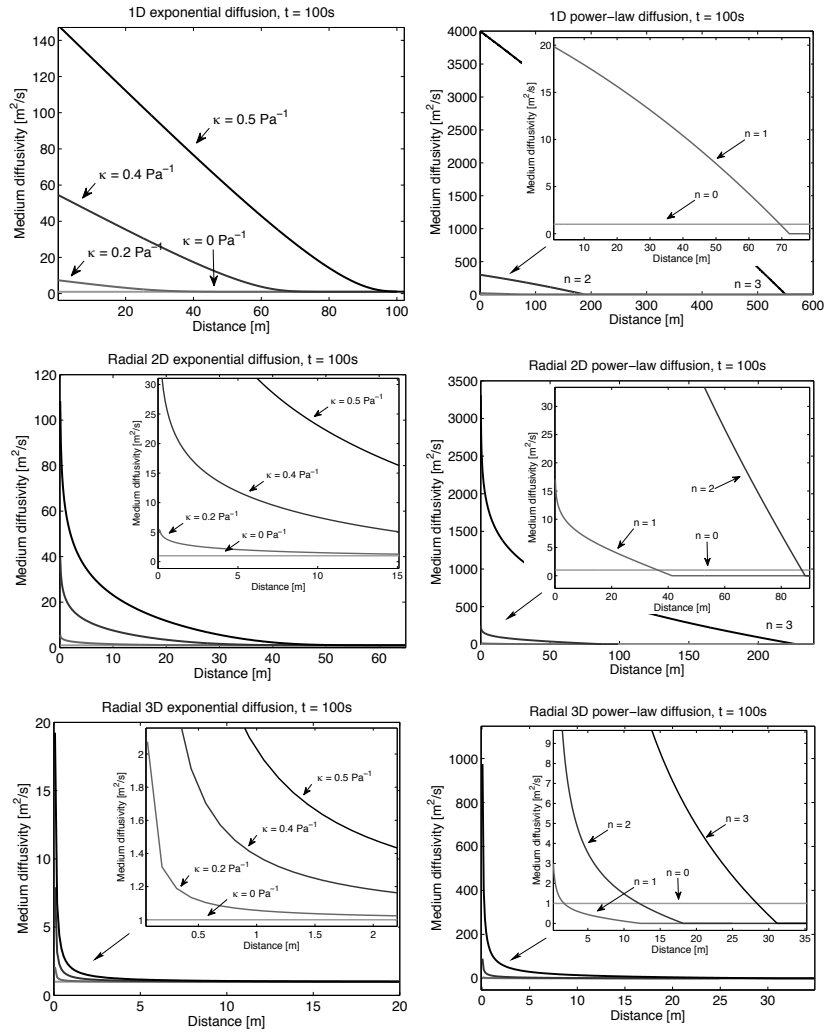


Figure 2.4: Snapshots of the medium diffusivity  $D(p(r; t))$  for different permeability compliances  $\kappa$  (left) and indices of non-linearity  $n$  (right) after  $t = 100$  s of injection. The medium diffusivity is calculated using the pore-fluid pressure evolution shown in Figure 2.3. One can see that the diffusivity strongly increases for increasing  $\kappa$  and  $n$ . For non-linear fluid-rock interaction ( $\kappa > 0 \text{ Pa}^{-1}$  and  $n > 0$ ) and a zero pressure perturbation the minimum diffusivity  $D(p(r; t))$  for the exponential diffusion model is  $D_{\min_e} = 1 \text{ m}^2\text{s}^{-1}$ . For the power-law diffusion model the minimum diffusivity is  $D_{\min_p} = 0 \text{ m}^2\text{s}^{-1}$ .

In 3-D the convex character of the pore-fluid pressure profiles still can be seen for the power-law diffusion model. For the exponential-dependent diffusivity model the permeability compliances  $\kappa$  are too small. However, if  $\kappa$  would be increased up to  $\kappa = 10 \text{ Pa}^{-1}$  the pore-fluid pressure profiles would also develop towards convexity. Regarding the shape of the pore-fluid pressure profiles another characteristic can be observed from their tips. For the exponential diffusion model the pressure profiles are characterized by a smooth transition at the pressure heads (like in the linear diffusion case). For the power-law diffusion model the pressure at the tip of the profiles drops to zero. Finally, the effect of geometrical spreading also appears in the pore-fluid pressure distributions. In 2- and 3-D the pressure perturbation injected with a constant magnitude is able to propagate into additional directions. As a result the pore-fluid pressure profiles are characterized by a strong spatial pressure decay in the vicinity of the injection point.

After analysing the spatio-temporal pore-fluid pressure distributions we now determine the hydraulic diffusivity of the medium  $D(p(r; t))$ . To obtain this medium diffusivity we insert the pressure field  $p(r; t)$  into the corresponding diffusion model (equation 2.2 or 2.3). For linear fluid-rock interaction ( $\kappa = 0 \text{ Pa}^{-1}$  and  $n = 0$ ) the diffusivity within the medium is equal to  $D_0 = 1 \text{ m}^2 \text{ s}^{-1}$  (Figure 2.4). For non-linear fluid-rock interaction ( $\kappa > 0 \text{ Pa}^{-1}$ ,  $n > 0$ ) the minimum medium diffusivity for the exponential model is  $D_{\text{min}_e} = 1 \text{ m}^2 \text{ s}^{-1}$  whereas for the power-law diffusion model the minimum medium diffusivity is  $D_{\text{min}_p} = 0 \text{ m}^2 \text{ s}^{-1}$ . Therefore, we propose that the exponential diffusion model better describes rocks having a non-negligible initial diffusivity. In contrast, the power-law model is more appropriate for rocks with very low permeabilities, such as shales.

### 2.3.2 Diffusivity estimates

From the comparison of the spatio-temporal pore-fluid pressure evolution with a criticality field we generate synthetic clouds of microseismicity (see section 2.2.3). In the following we analyze these clouds in terms of their diffusivity content. The heuristic diffusivity estimates are obtained using equation (2.1) and compared with averaged effective diffusivity values. For linear fluid-rock interaction we do not show the clouds of synthetic microseismicity. The results are consistent with the SBRC approach because in all three dimensions both heuristic diffusivity value  $D_h$  and effective diffusivity value  $D_{\text{eff}}$  are in agreement with the initial medium diffusivity  $D_0$ . We included the corresponding results in the following tables.

#### Exponential diffusion model

The results obtained for the exponential diffusion model (Figure 2.5 and Table 2.1) show that the envelope of the microseismic event cloud is always described by a

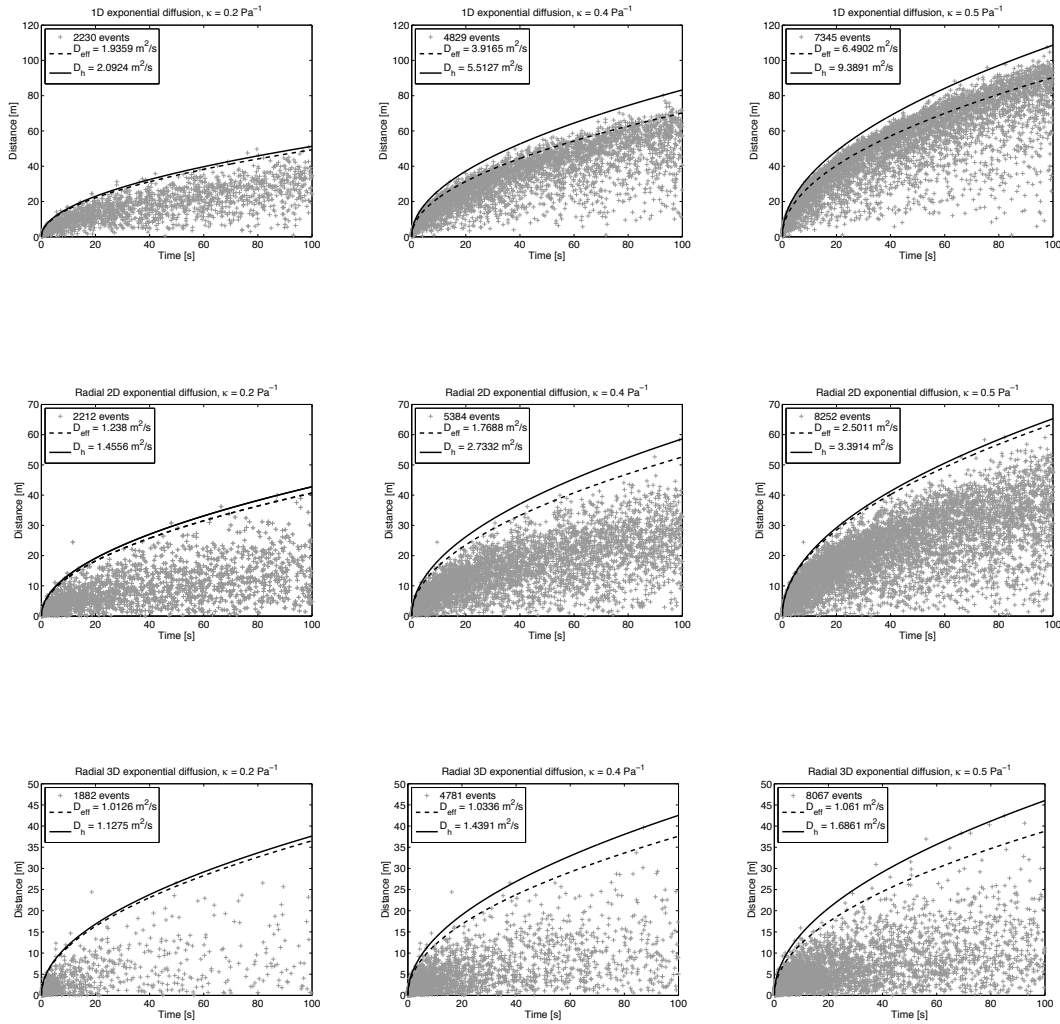


Figure 2.5: Synthetic clouds of microseismicity together with the results of the diffusivity analysis for the exponential diffusion model for 1-D (top), 2-D (middle) and 3-D (bottom). Comparing obtained heuristic diffusivity estimates  $D_h$  with the calculated effective diffusivity values  $D_{\text{eff}}$  one can see that even up to strong non-linear fluid-rock interaction ( $\kappa = 0.5 \text{ Pa}^{-1}$ ) the triggering front still provides reasonable diffusivity estimates. According to dimensional analysis the  $\sqrt{t}$ -dependent triggering front describes the envelope of seismicity - independent of the influence of non-linear fluid-rock interaction and spatial dimension.

parabola proportional to  $\sqrt{t}$ . This behaviour of the triggering front is independent of the influence of non-linearity as well as spatial dimension and agrees with the results obtained from dimensional analysis. Additionally, both heuristic diffusivity estimates and calculated effective diffusivity values increase with increasing non-linear fluid-

## 2 Microseismic estimates of hydraulic diffusivity in case of non-linear fluid-rock interaction

---

Table 2.1: Overview of results of our diffusivity analysis for the exponential diffusion model. Even up to strong non-linear fluid-rock interaction corresponding to a permeability compliance of  $\kappa = 0.5 \text{ Pa}^{-1}$  the heuristic diffusivity estimates  $D_h$  are in good agreement with the calculated effective diffusivity values  $D_{\text{eff}}$ . We conclude that taking into account pressure-dependent diffusivity the triggering front still provides reasonable diffusivity estimates.

Model	exponential diffusion		
Dimension	$\kappa [\text{Pa}^{-1}]$	$D_{\text{eff}} [\frac{\text{m}^2}{\text{s}}]$	$D_h [\frac{\text{m}^2}{\text{s}}]$
1-D	0	1.0	1.2
	0.2	1.9	2.1
	0.4	3.9	5.5
	0.5	6.5	9.4
2-D	0	1.0	1.2
	0.2	1.2	1.5
	0.4	1.8	2.7
	0.5	2.5	3.4
3-D	0	1.0	0.9
	0.2	1.0	1.1
	0.4	1.0	1.4
	0.5	1.1	1.7

rock interaction. Even for the largest value of the permeability compliance  $\kappa = 0.5 \text{ Pa}^{-1}$ , corresponding to a highly fractured rock (see Hummel and Müller, 2009), the heuristic diffusivity estimates are in a good agreement with the calculated effective diffusivity values. In 1-D,  $D_h$  is at most  $1.8 \text{ m}^2 \text{ s}^{-1}$  smaller compared to  $D_{\text{eff}}$ . In 3-D the difference between  $D_h$  and  $D_{\text{eff}}$  is at most  $0.6 \text{ m}^2 \text{ s}^{-1}$ . These results show that even up to strong non-linear fluid-rock interaction the triggering front still provides reasonable diffusivity estimates. However, these are estimates of the  $D_{\text{eff}}$  and not of  $D_0$ !

### Power-law diffusion model

For the power-law model (Figure 2.6 and Table 2.2) the agreement between heuristic and effective diffusivity depends on the magnitude of  $n$ . Heuristic diffusivity estimates and effective diffusivity values show good correlation for indices of non-linearity  $n < 2$  in 1-D and  $n < 3$  in 2-D. For larger  $n$  the heuristic estimates are approximately half as much as the effective values. However, the order of magnitude of the estimates is still the same compared to the effective values. Finally, the envelope of 1- and 2-D synthetic microseismicity is described by the  $\sqrt{t}$ -dependent triggering front (solid parabola). This  $\sqrt{t}$ -behaviour is in agreement with our results obtained

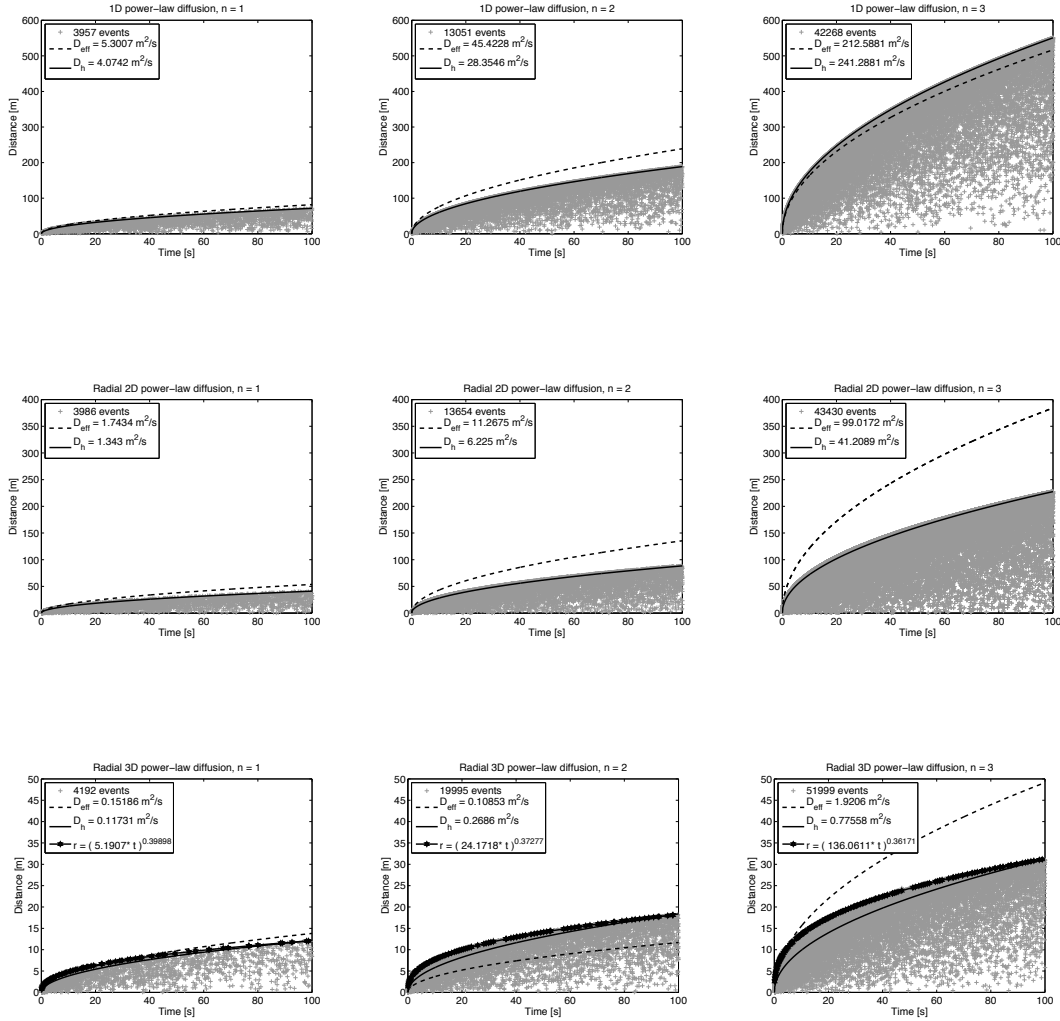


Figure 2.6: Synthetic clouds of microseismicity together with the results of the diffusivity analysis for the power-law diffusion model for 1-D (top), 2-D (middle) and 3-D (bottom). One can see that for 1-D and 2-D the  $\sqrt{t}$ -dependent triggering front (solid parabola) is the envelope of the microseismic event clouds. In 3-D the hexagram marked curved represents a function  $r = At^b$  describing the envelope of seismicity. For all three indices of non-linearity  $n$  the exponents  $b$  corresponds to the theoretically obtained exponents from relation (2.21).

from dimensional analysis. Only for the 3-D case a  $\sqrt{t}$ -dependent parabola (solid curve) is not any more the envelope of the microseismic event clouds. Moreover, the shape of the microseismic event clouds changes and the heuristic diffusivity estimates are smaller than  $D_0$  although the fluid-rock interaction is non-linear.

## 2 Microseismic estimates of hydraulic diffusivity in case of non-linear fluid-rock interaction

---

Table 2.2: Overview of results of our diffusivity analysis for the power-law diffusion model. In general the agreement between heuristic and effective diffusivity is quite good. At most  $D_h$  is half as much as  $D_{\text{eff}}$  but the order of magnitude still remains the same.

Model		power-law diffusion	
Dimension	$n$	$D_{\text{eff}} [\frac{m^2}{s}]$	$D_h [\frac{m^2}{s}]$
1-D	0	1.0	1.2
	1	5.3	4.1
	2	45.4	28.4
	3	212.6	241.3
2-D	0	1.0	1.2
	1	1.7	1.3
	2	11.3	6.2
	3	99.0	41.2
3-D	0	1.0	0.9
	1	0.2	0.1
	2	0.1	0.3
	3	1.9	0.8

## 2.4 Discussion of the results

### 2.4.1 Triggering front signatures

Independent of a linear or non-linear fluid-rock interaction described by both diffusivity models, our results reveal that for 1- and 2-D the triggering front is characterized by a  $\sqrt{t}$ -signature. From the results of the 3-D exponential diffusion case we also obtain a  $\sqrt{t}$ -dependent triggering front. This  $\sqrt{t}$  behaviour is in agreement with dimensional analysis. For this case the function  $f_e(\Theta_{e1})$  in the limit of  $\Theta_{e1} \rightarrow \infty$  becomes constant. Therefore, the triggering front has the form:

$$r_t = \sqrt{D_0 t} f_e(\infty, \Theta_{e2}), \quad (2.20)$$

where  $f_e(\infty, \Theta_{e2})$  denotes a function for the limit of  $\Theta_{e1} \rightarrow \infty$  and  $\kappa p_0$ .

We observe that for the 3-D power-law diffusion case a  $\sqrt{t}$ -dependent triggering front does not any more describe the envelope of synthetic microseismicity. Further, we attempt to find a function describing the  $r_t$ . We look for a function  $r = A t^b$  which describes the envelope of synthetic microseismicity (Figure 2.6) and provides a certain value for the exponent  $b$ . For  $n = 1$  we obtain an exponent of  $b = 0.39$ . For  $n = 2$  the exponent is  $b = 0.37$  and for  $n = 3$  the exponent is  $b = 0.36$ .

In the following we investigate the relationship for the triggering front introduced by Shapiro and Dinske (2009b) which is obtained for another set of boundary conditions simulating a constant fluid injection rate:

$$r_t \propto (D_0 t^{n+1})^{\frac{1}{d n + 2}} . \quad (2.21)$$

The theoretically obtained exponents of relation (2.21) are in agreement with exponents  $b$  obtained from fitting a function  $A t^b$  as envelope of synthetic microseismicity. Such a power-law dependence of the triggering front is in agreement with dimensional analysis. In this particular case the limit of the function  $f_p(\Theta_{p1})$  for  $\Theta_{p1} \rightarrow \infty$  becomes power-law dependent according to equation (2.16). For this asymptotical limit, solutions of the diffusion equation for boundary conditions simulating either a constant pressure source or a constant fluid injection source both coincide which leads to the same relaxation radius of pore-fluid pressure perturbation.

Besides our determination of the scaling behaviour of the triggering front in the case of non-linear diffusion our results constitutes a significant conceptual update of the SBRC approach. Formerly, the triggering front was considered to provide a large scale hydraulic diffusivity estimate of the in-situ rock. However, we demonstrate that the triggering front provides reasonable diffusivity estimates of  $D_{\text{eff}}$  instead of  $D_0$  - even for strong non-linear fluid-rock interaction. In contrast to  $D_0$  this effective diffusivity represents the medium after stimulation (including hydraulic fracturing) of rocks.

## 2.4.2 Assumptions and restrictions of our modelling

Both pressure-dependent hydraulic diffusivity models presented in equation (2.2) and (2.3) and corresponding differential equation (2.4) have the potential to describe fluid injection induced microseismicity based on non-linear pore-fluid pressure diffusion not only for the case of hydrocarbon recovery but also for geothermics. For example based on the exponential diffusion model Hummel and Müller (2009) found microseismic signatures of non-linear pore-fluid pressure diffusion in the case of the massive hydraulic fracturing experiment at Fenton Hill, New Mexico. On the other hand it is very well known that if the injection pressure exceeds the minimum principal stress magnitude, a hydraulic fracture is created. The growth velocity of the hydraulic fracture is mainly controlled by the injection rate, the viscosity of the fluid and the fluid losses through the walls of the fracture. Shapiro et al. (2006) describe hydraulic-fracturing controlled dynamics of microseismic clouds. Such situations, where fluid loss phenomena and fracture growth take place are more complex than our models (2.2) and (2.3). However, situations of an extremely impermeable rock (like for example shales) resulting in a negligible fluid loss from the hydraulically fractured domain is described by equation (2.3). Here  $d = 1$  and  $n \gg 1$  approximately corresponds to a classical hydraulic fracturing without fluid loss. The case of volumetric hydraulic fracture is described for  $d = 3$  and  $n \gg 1$  (Shapiro and Dinske, 2009b). Furthermore both models (2.2) and (2.3) have the same limit of linear pore-fluid pressure

diffusion approximately responsible for triggering microseismic events observable at geothermic sites like for example Basel or Cooper Basin (see also Shapiro and Dinske, 2009b). On the other side, our model has of course a limitation that we only consider monotonically increasing diffusivity (and hence permeability) with pressure. Thus it is unable to take into account possible irregularities in shear-induced dilatancy-related permeability changes like for example an occurrence and pressure-driven dynamic of a large-scale shear failure.

## 2.5 Conclusion

We investigated estimates of hydraulic diffusivity obtained from the triggering front in the case of non-linear fluid-rock interaction. We considered two models for the pressure dependence of hydraulic diffusivity, an exponential model as well as a power-law model which both lead to non-linear diffusion equations. Based on non-linear diffusion we obtained spatio-temporal pore-fluid pressure profiles that differ significantly in shape and magnitude from the profiles resulting from linear fluid-rock interaction. A comparison of the two diffusivity models shows that exponential-dependent diffusion is appropriate to describe the spatio-temporal evolution of the pore-fluid pressure perturbation in rocks having an in-situ non-negligible initial diffusivity. In contrast, the power-law diffusion model is more appropriate for rocks with a very low to almost zero diffusivity such as shales.

Non-linear diffusion, caused by both models describing non-linear fluid-rock interaction, still leads to a distinct and therefore detectable triggering front in the case of a constant injection pressure source. Based on the analytic scaling from dimensional analysis we revealed the character of the triggering front. For an exponential relation between diffusivity and pore-fluid pressure we found a square root temporal dependency of the triggering front as it is the case for linear diffusion. The power-law relation may lead to envelopes of the seismicity that can significantly deviate from the square root behaviour. In other words, a non square root of time-dependent triggering front is a clear indication of a non-linear diffusional pore-fluid pressure relaxation and therefore of a pressure-dependent hydraulic diffusivity.

Finally, the diffusivity analysis presented here leads to a new understanding of the SBRC approach. It also contributes to the important non-linear generalization of this method. Formerly, SBRC was perceived to provide large-scale estimates of hydraulic transport properties of the in-situ rock. However, with the results obtained from our study we clearly demonstrate that the triggering front provides reasonable diffusivity estimates characterizing the medium after a stimulation including a possible hydraulic fracturing of the rock.

## Acknowledgments

The authors thank the sponsors of the *PHASE* consortium for their financial support. We thank the editor and the reviewers Steven Oates and François H. Cornet for their valuable comments.

## 2.6 Appendix: Determination of the effective diffusivity

In the following we explain how we obtain the effective diffusivity averaging. According to Shapiro and Dinske (2009b) the non-linear diffusion equation (2.4) can be derived from two equations. The first one is the continuity equation which expresses the fluid mass conservation

$$\frac{\partial \rho_0 p S}{\partial t} = -\nabla \vec{U} \rho, \quad (2.22)$$

where  $\rho_0$  is the reference fluid density,  $S$  is a poroelastic compliance which is related to porosity and  $\vec{U}$  is the filtration velocity of the fluid. Assuming a spherical coordinate system in a  $d$ - dimensional space with the origin at the injection point, we can neglect the angular dependence and consider only the radial component. With the divergence in cylindrical and spherical coordinates

$$\nabla \vec{U} = \frac{1}{r^{d-1}} \frac{\partial}{\partial r} (r^{d-1} U_r) \quad (2.23)$$

the radial component of the continuity equation gives

$$\frac{\partial \rho_0 p S}{\partial t} = -\frac{1}{r^{d-1}} \frac{\partial (r^{d-1} U_r \rho)}{\partial r}. \quad (2.24)$$

The second equation which is necessary to obtain the non-linear diffusion equation (2.4) is the Darcy law which describes the balance between the viscous friction force and the pore-fluid pressure perturbation

$$\vec{U} = -\frac{\mathbf{k}}{\eta} \nabla p. \quad (2.25)$$

Here,  $\mathbf{k}$  describes the permeability tensor and  $\eta$  is the dynamic viscosity of the pore fluid. If we again suppose spherical symmetry the radial component of the Darcy law is given by

$$U_r = -\frac{k}{\eta} \frac{\partial p}{\partial r}. \quad (2.26)$$

Both,  $k$  and  $p$  depend on the radial distance  $r$  from the injection point. We can rewrite the two equations (2.24) and (2.26) resulting in

$$-r^{d-1} S \frac{\partial p}{\partial t} = \frac{\partial}{\partial r} r^{d-1} U_r \quad (2.27)$$

## 2 Microseismic estimates of hydraulic diffusivity in case of non-linear fluid-rock interaction

---

and

$$-U_r \frac{\eta}{k} = \frac{\partial}{\partial r} p. \quad (2.28)$$

By introducing averaging as well as matrix notation we obtain from equation (2.27) and (2.28)

$$\left\langle \frac{\partial}{\partial r} \begin{pmatrix} r^{d-1} U_r \\ p \end{pmatrix} \right\rangle = \left\langle \begin{pmatrix} 0 & -S r^{d-1} \frac{\partial}{\partial t} \\ -\frac{\eta}{r^{d-1} k(r)} & 0 \end{pmatrix} \begin{pmatrix} r^{d-1} U_r \\ p \end{pmatrix} \right\rangle. \quad (2.29)$$

Here,  $r^{d-1} U_r$  and  $p$  are continuous functions of  $r$ . If we consider a sufficiently small shell of thickness  $\delta r$  both  $r^{d-1} U_r$  as well as  $p$  are constant. Therefore, they can be excluded from the averaging which results in

$$\left\langle \frac{\partial}{\partial r} \begin{pmatrix} r^{d-1} U_r \\ p \end{pmatrix} \right\rangle = \left\langle \begin{pmatrix} 0 & -S r^{d-1} \frac{\partial}{\partial t} \\ -\frac{\eta}{r^{d-1} k(r)} & 0 \end{pmatrix} \right\rangle \begin{pmatrix} r^{d-1} U_r \\ p \end{pmatrix}. \quad (2.30)$$

At this point we strictly follow the theory of homogenisation (see Sanchez-Palencia, 1980) and introduce a second scale  $r_s$  being smaller than  $r$ . On this smaller scale  $r_s$  medium properties like  $k$  and  $S$  do not have to be constant within the shell of thickness  $\delta r$ . Moreover, as a consequence of the nature of the medium,  $k$  and  $S$  can vary significantly within the shell. For the averaging of the matrix containing the medium properties it follows that

$$\left\langle S \right\rangle = S^*, \quad (2.31)$$

$$\left\langle \frac{\eta}{k} \right\rangle = \eta \left\langle \frac{1}{k} \right\rangle = \eta \frac{1}{k^*}. \quad (2.32)$$

In (2.32) we assume that the dynamic viscosity of the pore fluid is constant. It becomes obvious that

$$k^* = \left\langle \frac{1}{k} \right\rangle^{-1}. \quad (2.33)$$

Consequently, for the hydraulic diffusivity we obtain

$$\left\langle \frac{1}{D} \right\rangle^{-1} = \left( \frac{\eta S^*}{k^*} \right)^{-1} = D_{eff}, \quad (2.34)$$

which finally will result in equations (2.17) and (2.18).

To confirm our averaging scheme we consider a numerical simulation. The model for this simulation consists of a 3-D radial symmetric medium with only two layers. The

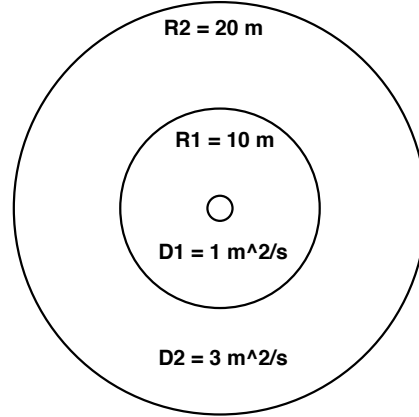
first shell has a thickness of  $R_1 = 10$  m and a homogeneous diffusivity of  $D_1 = 1$  m<sup>2</sup>/s. The second shell also has a thickness of 10 m and a homogeneous diffusivity of  $D_2 = 3$  m<sup>2</sup>/s (Figure 2.7a). For this model we solve equation (2.4) for the linear diffusion limit. Afterwards we perform the same simulation but instead of using a heterogeneous medium characterized by  $D_1$  and  $D_2$  we now consider a hydraulically homogeneous medium with an average hydraulic diffusivity. According to equation (2.17) this effective hydraulic diffusivity is  $D_{\text{eff}} = 1.5$  m<sup>2</sup>/s. The same value is obtained from equation (2.18) which for this particular model takes the following form

$$D_{\text{eff}} = \left[ \left\langle \frac{1}{D} \right\rangle \right]^{-1} = \left[ \frac{1}{(R_2)} \int_0^{R_2} \frac{1}{D} dr \right]^{-1}. \quad (2.35)$$

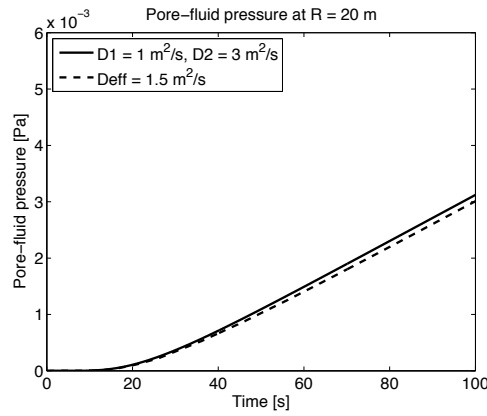
For both simulations we compare the temporal evolution of the pore-fluid pressure perturbation at  $R = 20$  m (see Figure 2.7b). The resulting relative differences are of the order of  $10^{-4}$  which hence confirms the applicability of our averaging.

## 2 Microseismic estimates of hydraulic diffusivity in case of non-linear fluid-rock interaction

---



(a) Model parameters



(b) Resulting temporal pore-fluid pressure evolution evaluated at  $R_2 = 20 \text{ m}$ .

Figure 2.7: (a): Simple radial symmetric model to validate our averaging scheme. The model consists of two layers having the same thickness of 10 m, but different diffusivities  $D_1 = 1 \text{ m}^2/\text{s}$  and  $D_2 = 3 \text{ m}^2/\text{s}$ . (b): Temporal evolution of the pore-fluid pressure perturbation at  $R = 20 \text{ m}$  for two different simulations. First the 3-D diffusion equation (2.4) in the linear diffusion limit is solved using the hydraulically heterogeneous model shown on the left (solid line). Second, the pore-fluid pressure perturbation is calculated for a replacing homogeneous medium with an effective diffusivity of  $D_{eff} = 1.5 \text{ m}^2/\text{s}$  obtained from the averaging scheme (dashed line). As one can see the temporal pore-fluid pressure evolutions from both simulations show good agreement. The small differences in the pore-fluid pressure perturbation are of relative magnitude  $10^{-4}$ .

## Chapter 3

# Non-linear diffusion-based interpretation of induced microseismicity: A Barnett Shale hydraulic fracturing case study <sup>1</sup>

For copyright reasons, this chapter was removed from the digital version.

---

<sup>1</sup>This article has been accepted for publication in *Geophysics*: N. Hummel and S. A. Shapiro (2013). Nonlinear diffusion-based interpretation of induced microseismicity: A Barnett Shale hydraulic fracturing case study. 78(5), B211–B226, <http://dx.doi.org/10.1190/geo2012-0242.1>. Published by the Society of Exploration Geophysicists (SEG).

3 Non-linear diffusion-based interpretation of induced microseismicity:  
A Barnett Shale hydraulic fracturing case study

---

## **Chapter 4**

# **Back front of seismicity induced by non-linear fluid-rock interaction <sup>1</sup>**

---

<sup>1</sup>Submitted to be considered for publication in *Geophysical Prospecting*: N. Hummel and S. A. Shapiro. Back front of seismicity induced by non-linear fluid-rock interaction.

### Summary

Borehole fluid injections are accompanied by microseismic activity not only during but also after termination of the fluid injection. Previously, this phenomenon has been analyzed assuming that the main triggering mechanism is governed by a linear pressure diffusion in a hydraulically isotropic medium. In this context the so-called back front of seismicity has been introduced which allows to characterize the hydraulic transport from the spatio-temporal distribution of post-injection induced events.

However, rocks are generally anisotropic and, in addition, fluid injections can strongly enhance the permeability which then becomes a function of pressure. For such situations, we carry out a comprehensive study about the behaviour and parameterization of the back front. Based on a model of a factorized anisotropic pressure dependence of permeability we present an approach to reconstruct the principal components of the diffusivity tensor. We apply this approach to microseismic data from the Ogachi and Fenton Hill geothermal experiment. Our results show that the back front characterizes the least hydraulic transport.

To investigate the back front of non-linear pore-fluid pressure diffusion we consider numerically a power-law and an exponential dependent diffusivity. To account for a post-injection enhanced hydraulic state of the rock we introduce a model of a frozen (i.e. nearly unchanged after the stimulation) medium diffusivity and generate synthetic seismicity. As for Ogachi and Fenton Hill, we find that for a weak non-linearity and 3-D exponential diffusion the linear diffusion back front is still applicable. However, for a strong non-linear fluid-rock interaction such as the hydraulic fracturing, the back front can significantly deviate from a time dependence of a linear diffusion back front. This is demonstrated for a data set from the Horn River Basin. Hence, the behaviour of the back front is a strong indicator of a non-linear fluid-rock interaction.

## 4.1 Introduction

For the successful development and operation of hydrocarbon and geothermal reservoirs knowledge of the hydraulic transport is of crucial importance. Flow characteristics influence not only the position optimization of cost-effective stimulation and production wells. They also affect the design and completion of borehole fluid injections. Such hydraulic stimulation treatments are performed to increase hydrocarbon recovery or to create Enhanced Geothermal Systems (see for example Economides and Nolte, 2000; Majer et al., 2007). Since fundamental physical processes of borehole fluid injections are still insufficiently understood gathering information about transport properties of rocks under field conditions is still quite difficult.

However, over the past few years, one has understood that promising possibilities for permeability characterization are given as a by-product of hydraulic stimulation treatments. As a consequence of the fluid injection the pore-fluid pressure becomes perturbed. Since most parts of the Earth's crust are in a critically stressed state (Barton et al., 1995; Zoback and Townend, 2001) artificial stress perturbations through fluid injections can cause seismic activity. Nowadays, these induced events are taken into account in a variety of applications such as fracture evaluation mapping (for example Rutledge et al., 1998; Economides and Nolte, 2000) or quantification of the reservoirs seismotectonic conditions for hazard risk analysis (Shapiro et al., 2010). However, these events also can be used for permeability characterization. In particular, understanding the distribution of induced seismicity in space and time provides a substantial contribution in gathering information about the corresponding hydraulic transport.

For instance, Shapiro et al. (1997, 1999, 2002) show that the spatio-temporal characteristics of fluid-injection induced seismicity can be explained by a diffusional relaxation of the pore-fluid pressure perturbation  $p$ . Additionally, they develop a technique to determine hydraulic transport properties from the observed rate of growth of the microseismic cloud. The so-called seismicity-based reservoir characterization (SBRC) approach assumes a linear pressure diffusion to be the main triggering mechanism of fluid injection induced seismicity. Therefore, the hydraulic transport is supposed to be characterized by a constant with time and pressure diffusivity  $D_0$  (i.e. linear fluid-rock interaction).

An estimate of this scalar hydraulic diffusivity  $D_0$  can be derived from the parabolic signature (i.e.  $\sqrt{t}$ -dependence of the envelope) of observed seismicity on  $r - t$  diagrams. For this, the radial distance  $r$  of events from the injection point is plotted versus their corresponding occurrence times  $t$ . In such  $r - t$  diagrams the triggering front approximately describes the outermost envelope of seismicity which is induced during the injection phase. For a homogeneous and isotropic medium the triggering

front is given by the following equation

$$r = \sqrt{4\pi D_0 t}. \quad (4.1)$$

Hence, fitting the parabola described by equation 4.1 as an envelope of induced events allows to characterize the hydraulic transport of a given rock volume.

However, the occurrence of fluid injection induced seismicity is not only limited to the injection phase. Even after termination of the fluid injection seismic activity can still be monitored for several hours to days, as for instance at Barnett Shale (Shapiro and Dinske, 2009a), Basel (Häring et al., 2008; Dinske et al., 2009; Goertz-Allmann and Wiemer, 2013), the Canyonsands (Fischer et al., 2008), Cooper Basin (Baisch et al., 2006), Cotton Valley (Urbancic et al., 1999; Shapiro et al., 2006; Dinske et al., 2010), Fenton Hill (Fehler et al., 1998; Parotidis et al., 2004; Langenbruch and Shapiro, 2010), Soultz-sous-Forêts (Dyer et al., 1994; Parotidis et al., 2004; Langenbruch and Shapiro, 2010) or Ogachi (Kaieda et al., 2010). This phenomenon of post-injection induced seismicity has been studied by Parotidis et al. (2004). In corresponding  $r - t$  diagrams of induced events they observe a domain of seismic quiescence. After shut-in this parabolic aseismic area evolves with increasing time and distance from the injection point. To explain this observation Parotidis et al. (2004) follow the approach formerly introduced by Shapiro et al. (1997, 1999, 2002). They also consider linear pore pressure diffusion as the main triggering mechanism of observed seismicity. However, despite shut-in, the pressure perturbation is still able to increase as a function of time and distance from the injection point until it has reached a certain maximum. Thereafter, the pressure perturbation starts to decrease which, in turn, increases the effective normal stress and leads to a strengthening of induced cracks and fractures. Consequently, seismic events can not be triggered at locations where the pressure has already reached its maximum. This distance from the injection point  $r$  at which seismicity is terminated at a given time  $t$  after the end of the fluid injection at  $t_0$  is described by the back front (Parotidis et al., 2004). For a hydraulically homogeneous and isotropic  $d$ - dimensional medium the back front is given by the following equation

$$r = \sqrt{2d D_0 t \left( \frac{t}{t_0} - 1 \right) \ln \left( \frac{t}{t - t_0} \right)}. \quad (4.2)$$

Hence, fitting the curve described by equation 4.2 as an envelope of the post-injection aseismic area in the  $r - t$  domain allows to determine a scalar hydraulic diffusivity estimate  $D_0$ . For the given assumptions this hydraulic diffusivity estimate corresponds to the one provided by the triggering front.

However, fluid injections like for example hydraulic fracturing treatments can considerably enhance the permeability (Economides and Nolte, 2000). Consequently, it is not sufficient to assume a constant with time and pressure hydraulic transport.

Moreover, permeability becomes a function of the pressure. In this case the fluid-rock interaction becomes strongly non-linear which results in a non-linear pressure diffusion (Shapiro and Dinske, 2009b; Hummel and Müller, 2009; Hummel and Shapiro, 2012, 2013).

Currently, two different models of a pressure-dependent hydraulic transport are discussed in the literature. Both models approximate the complicated stimulation-caused permeability evolution for different rock conditions (Figure 4.1). One is the following power-law model

$$D(p(r; t)) = (n + 1) D_0 p^n(r; t), \quad (4.3)$$

which formerly was introduced by Shapiro and Dinske (2009b). This power-law model approximates the evolution of hydraulic transport properties during fracturing for situations where the initial formation permeability can be nearly neglected (e.g. shales). The quantity  $n$  is called index of non-linearity. It does not only control the grade of non-linearity on the diffusion. Physically,  $n$  is also an effective reservoir property which depends on the lithology, elastic properties, strength, pore space geometry and stress state of rocks. If  $n$  is large, the diffusivity will depend strongly on the pressure. In the limit of  $n = 0$  the diffusivity becomes independent of the pressure which results in a linear pressure diffusion. The corresponding hydraulic transport is then characterized by the constant  $D_0$ . Therefore,  $D_0$  is also a normalizing parameter which should not be interpreted independently.

Shapiro and Dinske (2009b) show that the  $t^{1/2}$  behaviour of equation 4.1 is a particular case of a more general form for the triggering front. Based on the power-law dependent diffusivity model (equation 4.3) this general form also includes the possibility of a  $t^{1/3}$  dependence. For seismicity induced during a hydraulic fracturing treatment in the Barnett Shale Shapiro and Dinske (2009b) demonstrate that such a cubic root of time-dependent triggering front better matches the data than a square root parabola. Consequently, such a triggering front signature is a strong indication for a pressure-dependent hydraulic transport.

Additionally, this observation is confirmed by Hummel and Shapiro (2013). For the power-law dependent diffusivity model (equation 4.3) they generate synthetic non-linear diffusion-based seismicity clouds. For an index of non-linearity  $n = 7$  they observe that the temporal behaviour of the envelope of synthetic seismicity is in agreement with the triggering front behaviour of Barnett Shale seismicity. Their results demonstrate that non-linear pressure diffusion in the fractured domain can explain seismicity triggering. Potentially, such a power-law dependent permeability describes the corresponding fluid transport process during the hydraulic fracturing treatment in the Barnett Shale. Consequently, this power-law model is motivated and supported by real data.

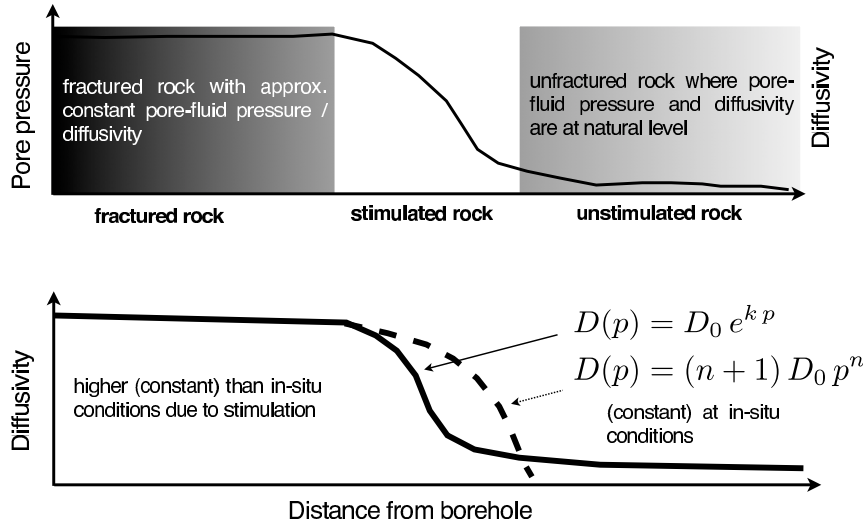


Figure 4.1: Fluid injection-caused distribution of pore pressure and diffusivity as function of the distance from the injection point. To approximate the complicated evolution of hydraulic transport properties during stimulation treatments two pressure-dependent diffusivity models are considered in more detail. The power-law dependent diffusivity model is useful for situations where the initial formation permeability can be almost neglected (e.g. shales). In contrast, the exponential dependent diffusivity model is more appropriate if the initial formation permeability plays a non-negligible role (e.g. granitic rocks).

Alternatively, we also consider an exponential dependence of diffusivity on the pressure perturbation  $p$

$$D(p(r; t)) = D_0 e^{\kappa p(r; t)}. \quad (4.4)$$

Formerly, this model is based on a study of Yilmaz et al. (1994). They analyze pore pressure distribution in fractured and compliant rocks. In the context of fluid injection induced seismicity, the exponential model shown in equation 4.4 was introduced by Hummel and Müller (2009). It is appropriate for rocks having an in-situ non-negligible initial diffusivity (e.g. granitic rocks, geothermal reservoirs). The pressure influence is given by the so-called permeability compliance  $\kappa$ . Table 4.1 shows values of  $\kappa$  reported for different porous rocks and geothermal injection sites. If  $\kappa$  is large the hydraulic diffusivity will strongly depend on pressure. In the limit of  $\kappa = 0 \text{ Pa}^{-1}$  the diffusivity becomes independent of the pressure which results in a linear pressure diffusion. In analogy to the power-law model the corresponding hydraulic transport is then characterized by the constant  $D_0$ .

Both pressure-dependent diffusivity models (equation 4.3 and 4.4) effectively address the impact of a growing hydraulically stimulated domain on the pressure diffusion. Pre-existing joints or planes of weakness can be completely closed at a

Table 4.1: Some documented permeability compliances  $\kappa$  for different porous rocks (obtained from laboratory measurements) and injection sites.

Rock type / Reservoir	Porosity	$\kappa$ [GPa <sup>-1</sup> ]	Reference
Fractured rock		5 ... 400	Yilmaz et al. (1994)
Fractured rock		$\approx 500$	Daley et al. (2006)
E-bei sandstone	0.02 ... 0.11	60 ... 170	Li et al. (2009)
Tight gas sandstone	0.03 ... 0.08	33 ... 115	Walls et al. (1982)
Shale		11 ... 81	Best and Katsube (1995)
Fenton Hill		79 ... 196	Nathenson (1999)
KTB		140	Millich et al. (1998)
Rosemanovs		225 ... 334	Nathenson (1999)

zero injection pressure (for instance,  $D(p(r;t)) = 0$  m<sup>2</sup>/s for  $n > 0$  and  $p(r;t) = 0$  Pa). Consequently, they do not contribute at all to the diffusivity. An increase in pressure can cause these joints to open which then contribute to an enhanced hydraulic transport. For such situations of a non-linear fluid-rock interaction Hummel and Shapiro (2012) explore the nature of hydraulic diffusivity estimates provided by the triggering front. Taking into account different indices of non-linearity  $n$  and permeability compliances  $\kappa$  they compute  $r - t$  diagrams of synthetic event catalogs. Thereafter, they analyze spatio-temporal characteristics of corresponding seismicity clouds. For a pressure-dependent hydraulic transport their results show that the triggering front still provides reasonable diffusivity estimates. However, instead of  $D_0$ , these estimates correspond to an effective diffusivity. This effective diffusivity represents the enhanced heterogeneously distributed diffusivity of the stimulated rock.

However, in addition to a non-linear hydraulic transport most rocks are also elastically and hydraulically anisotropic. Such a nature controls the distribution of microseismicity which is not only caused by an anisotropic permeability. For instance, an anisotropic stress distribution is strongly influenced by an anisotropic elasticity and strength of the rock (see e.g. Langenbruch and Shapiro, 2012). Usually, the anisotropy of hydraulic permeability is much stronger than the anisotropy of elastic properties.

So far, knowledge about non-linear fluid-rock interaction and its impact on induced seismicity is focused on the triggering front. As described above, there are several studies working towards a further generalization of the SBRC approach in the sense of taking into account pressure-dependent transport properties. However, these works only consider the injection phase. In comparison, little is known

about the post-injection phase. This motivated us to comprehensively investigate the termination of seismicity induced by non-linear fluid-rock interaction with a particular focus on corresponding signatures of the back front. To our knowledge such a study has been neither published nor performed. Since the back front has been derived for situations of a constant with time and pressure hydraulic transport within isotropic media the following questions arise: If we consider a hydraulically anisotropic medium what kind of diffusivity estimates are provided by the back front in respect of the permeability tensor? How does the back front look like in media with a pressure-dependent hydraulic transport? How can we use the information of the back front signature for reservoir characterization? What does post-injection induced seismicity tell us about the medium behaviour?

To answer these questions is the subject of our paper. In its first part we focus on improving the understanding of the back front for the case of hydraulically anisotropic media. We will explore what kind of diffusivity estimates are provided by the back front in respect of the corresponding permeability tensor.

In the second part we particularly focus on the back front signatures. We will show that the temporal dependence of the back front does not always have to be the same as in the linear diffusion case. To explain this phenomenon we perform a numerical modelling. We introduce a model of a frozen medium diffusivity to account for a post-injection enhanced hydraulic transport. We then generate clouds of synthetic microseismicity by solving non-linear diffusion equations. We analyze spatio-temporal characteristics of these clouds and find back front signatures which can significantly differ from the ones of the linear diffusion case. In particular, we show that these signatures are in agreement with those observed in real data. Additionally, the comparison of real and synthetic data even allows us to determine the type of fluid-rock interaction in more detail.

### **4.2 Meaning of back front estimates in anisotropic media**

In the following we will focus on the nature of diffusivity estimates provided by the back front. For the data under consideration we will first apply the back front concept to determine a heuristic diffusivity estimate solely from the spatio-temporal distribution of post-injection induced seismicity. Then, we will independently apply the triggering front concept to deduce a diffusivity estimate for the injection phase. Hence, this allows us to directly compare both hydraulic estimates.

However, locations of microseismic events are generally influenced by the anisotropic nature of the rock. Since the back front (equation 4.2) has been derived for hydraulically linear and isotropic media (and we are going to apply it for effective estimates)

we must firstly apply an event cloud transformation. This transformation approach allows to account for an anisotropic hydraulic transport. With this normalization approach we transform clouds of hypocenters of events obtained in a hydraulically anisotropic non-linear medium into a cloud which would be obtained in an equivalent isotropic but still non-linear medium.

For this resulting event cloud we then repeat our analysis of spatio-temporal characteristics. We combine the estimated diffusivity value with scaling factors obtained from the transformation approach to reconstruct the factorized diffusivity tensor. Finally, we compare the original back front diffusivity estimate obtained from the natural event cloud with the reconstructed factorized diffusivity tensor. This allows us to determine what kind of diffusivity estimates are provided by the back front with respect to the underlying anisotropic hydraulic transport. Finally, we will apply this analysis to seismicity recorded during borehole fluid injection experiments at Ogachi (Japan) and Fenton Hill (New Mexico, U.S.).

### 4.2.1 Normalization of microseismic event clouds

Most rocks associated with geothermal and hydrocarbon reservoirs are elastically and hydraulically anisotropic. Usually, the anisotropy of hydraulic permeability is much stronger than the anisotropy of elastic properties. For deeper subsurface rocks like granites, hydraulic anisotropy is mainly caused by the preferred orientation of pre-existing fissures, cracks and fractures. Such small to large scale natural fractures are favorably oriented according to the local stress conditions (Pechinig et al., 1997; Ito, 2003; Häring et al., 2008). In contrast, sedimentary rocks like shales or sandstones have been subjected to deposition. Diagenese including physical, chemical and biological processes leads to compaction, dewatering, cementation, layering and gravity induced alignment (i.e. ordering and sorting) of grains which all changes the composition and texture of such rocks. Additionally, recrystallization due to pressure and temperature causes grains themselves to undergo significant alteration. This does not only change the original sediments, but also leads to the formation of different rocks (Pettijohn, 1948; Larsen and Chilingarian, 1983; Tucker, 2001). Besides these processes on the grain and bedding scale, fracturing and folding due to tectonic activity can lead to well-defined rock domains of different physical properties. However, since hydraulic anisotropy affects the distribution of induced seismicity independently of the existing rock type, anisotropy has to be taken into account when studying back front signatures of induced seismicity.

Hummel and Shapiro (2013) have introduced an event cloud transformation approach which accounts for this anisotropy. It is based on a model of a non-linear and factorized anisotropy of permeability. In what follows we briefly recapitulate this approach which we then further generalize for the case of any unknown non-linear fluid-rock interaction.

A real configuration of a fluid injection into a borehole is approximated by a point source of pore-fluid pressure perturbation into a three dimensional, initially hydraulically homogeneous, anisotropic, non-linear, and fluid-saturated medium. According to Shapiro et al. (1997, 1999) and Shapiro and Dinske (2009b) the spatio-temporal evolution of the pressure perturbation can be derived by considering two different equations. The first is the continuity equation which expresses the conservation of the fluid mass. The second equation, Darcy's law, describes the balance of the pressure perturbation and viscous friction force. The combination of both equations leads to the following differential equation of diffusion:

$$\frac{\partial p}{\partial t} = \nabla \mathbf{D}(p) \nabla p. \quad (4.5)$$

Equation 4.5 describes the distribution of the pressure perturbation in space and time. In the principal coordinate system of the pressure-dependent hydraulic diffusivity tensor,  $\mathbf{D}(p)$  is a diagonal matrix with corresponding tensor components  $D_{ii}(p)$  for  $i = 1, 2, 3$ . Generally, these tensor components  $D_{ii}(p)$  and their pressure dependence do not necessarily have to be mutually similar. Depending on the anisotropy of the rock, the directivity of the hydraulic transport can be arbitrarily different. However, although the anisotropic permeability depends on the geological structure and strength of the rock Hummel and Shapiro (2013) assume that for all three components  $i$  of the permeability tensor in the principal coordinate system the dependence of hydraulic diffusivity on the pressure perturbation is the same. We call such a model a factorized non-linear hydraulic anisotropy. For both the power-law as well as the exponential-dependent diffusivity model this implies the following. Since  $\kappa$  and  $n$  control the pressure influence on the diffusivity both parameters are isotropic quantities. Otherwise, the pressure-dependence would be directional-dependent. Thus, in order to account for a hydraulically anisotropic transport the anisotropy is assumed to affect the parameter  $D_0$ . For these assumptions, the diffusivity tensor can be decomposed (i.e. factorized) into a pressure-dependent part and an anisotropic part:

$$\mathbf{D}(p) = f(p) \begin{pmatrix} D_{011} & 0 & 0 \\ 0 & D_{022} & 0 \\ 0 & 0 & D_{033} \end{pmatrix}. \quad (4.6)$$

The pressure-dependent part is represented by the first factor  $f(p)$ . In general,  $f(p)$  can represent an arbitrary functional dependence on pressure. However, in our case,  $f(p) = (n+1)p^n$  for the power-law model and  $f(p) = e^{\kappa p}$  for the exponential model. This factor  $f(p)$  accounts for the pressure-dependent contribution of pre-existing joints or planes of weakness on the hydraulic transport. It effectively addresses the impact of a growing hydraulically stimulated domain on the pressure diffusion and associated microseismicity. Consequently,  $f(p)$  can be understood as a stimulation impact factor. For the situation of a linear fluid-rock interaction (given by  $n = 0$  and  $\kappa = 0 \text{ Pa}^{-1}$ ) this stimulation impact factor becomes equal to one. For this asymptotic

linear diffusion limit in a hydraulically anisotropic medium the hydraulic transport is completely described by the tensor elements  $D_{011}$ ,  $D_{022}$  and  $D_{033}$ . Hence, this tensorial anisotropy factor controls the directivity of the stimulation and thus the directivity of the hydraulic transport.

However, in reality, the fluid injection creates a medium with an enhanced heterogeneously distributed diffusivity. Additionally, assessing information about  $f(p)$  is quite difficult. The index of non-linearity  $n$  as well as the permeability compliance  $\kappa$  are both usually unknown and difficult to determine. On the basis of numerical simulations such situations have been studied by Hummel and Shapiro (2012). For synthetic non-linear pressure diffusion-based seismicity clouds they analyze the nature of diffusivity estimates which are provided by the triggering front. For this they fit equation 4.1 as envelope of injection induced events. The result of their spatio-temporal analysis shows that the heuristic diffusivity values are meaningful estimates of an effective diffusivity. This effective diffusivity represents the enhanced heterogeneously distributed diffusivity of the stimulated domain. Therefore, we adopt this approach and approximate an unknown non-linear hydraulic transport by an appropriate heuristic diffusivity estimate.

Since we consider a hydraulically anisotropic non-linear medium and a pressure diffusion in the principal coordinate system of the diffusivity tensor the hydraulic transport in each direction can be different. Consequently, for each principal direction, the unknown non-linear hydraulic diffusivity is replaced by the corresponding heuristic diffusivity estimate  $D_{h_{ij}}$ . We note that this replacement does not depend on the non-linearity of the process. In other words, the heuristic diffusivity approximates the effective hydraulic transport independent of the type and magnitude of the stimulation impact factor. Therefore, we approximate equation 4.6 by

$$\mathbf{D}(p) \Big|_{t=t_0} \approx \begin{pmatrix} D_{h_{11}} & 0 & 0 \\ 0 & D_{h_{22}} & 0 \\ 0 & 0 & D_{h_{33}} \end{pmatrix}. \quad (4.7)$$

Following Hummel and Shapiro (2013) we then normalize the anisotropic diffusivity by introducing new coordinates  $[x', y', z']$

$$x' = x \sqrt{\frac{D_{h_{iso}}}{D_{h_{11}}}}, \quad y' = y \sqrt{\frac{D_{h_{iso}}}{D_{h_{22}}}}, \quad z' = z \sqrt{\frac{D_{h_{iso}}}{D_{h_{33}}}}, \quad (4.8)$$

where

$$D_{h_{iso}} = \sqrt[3]{D_{h_{11}} D_{h_{22}} D_{h_{33}}}. \quad (4.9)$$

This normalization reduces the anisotropic diffusion equation to an effective isotropic one. In contrast to the arithmetic mean, the geometric mean-based scaling (equation 4.9) is motivated by the fact that it will be more representative if one

parameter is much larger than others. This is typically the case for situations of a hydraulic fracturing for which this normalization is also valid (Hummel and Shapiro, 2013). There, we often observe a certain preferred direction of the hydraulic transport in which the diffusivity can be significantly larger compared to the other two.

To apply this normalization (equation 4.8) to real microseismic data we first have to identify the directivity of the hydraulic transport. For this we consider the particular shape of the seismicity cloud. Following Hummel and Shapiro (2013) we determine the characteristic dimensions  $L$  from the geometry of the cloud. We first carry out a principal component analysis and rotate the event cloud into the principal coordinate system (PCS). For the corresponding principal  $X$ -,  $Y$ -, and  $Z$  direction we then estimate the characteristic dimensions  $L_{\max}$ ,  $L_{\text{int}}$  and  $L_{\min}$ , respectively. We note that our characteristic lengths represent upper limits as we do not exclude any located event. Consequently, events which may have been triggered by static stress changes are also included. Note also that for microseismic data stress changes are driven by pressure changes. Otherwise their occurrence time would be close to standard seismic arrival times. These characteristic lengths are used to determine scaling factors  $F_{X\text{scal}}$ ,  $F_{Y\text{scal}}$ ,  $F_{Z\text{scal}}$  according to

$$F_{X\text{scal}} = \frac{L_{\max}}{L_{\text{scal}}}, \quad F_{Y\text{scal}} = \frac{L_{\text{int}}}{L_{\text{scal}}}, \quad F_{Z\text{scal}} = \frac{L_{\min}}{L_{\text{scal}}}, \quad (4.10)$$

where  $L_{\text{scal}} = \sqrt[3]{L_{\max} \cdot L_{\text{int}} \cdot L_{\min}}$ . With these scaling factors we finally scale the coordinates of events  $j$  according to

$$X_{\text{transf. } j} = \frac{X_j}{F_{X\text{scal}}}, \quad Y_{\text{transf. } j} = \frac{Y_j}{F_{Y\text{scal}}}, \quad Z_{\text{transf. } j} = \frac{Z_j}{F_{Z\text{scal}}}. \quad (4.11)$$

With these new locations  $X_{\text{transf}}$ ,  $Y_{\text{transf}}$ ,  $Z_{\text{transf}}$  the event cloud is normalized into a cloud which would result in a hydraulically equivalent isotropic but still non-linear medium.

Finally, information about the directionality can be assessed from the scaling factors. The combination of equations 4.8 and 4.11 allows to reconstruct the effective diffusivity along the principal axes of the diffusivity tensor (because both normalizations result in creating isotropic clouds)

$$\begin{aligned} D_{h_{11}} &= F_{X\text{scal}}^2 \cdot D_{h_{\text{iso}}}, \\ D_{h_{22}} &= F_{Y\text{scal}}^2 \cdot D_{h_{\text{iso}}}, \\ D_{h_{33}} &= F_{Z\text{scal}}^2 \cdot D_{h_{\text{iso}}}. \end{aligned} \quad (4.12)$$

This type of renormalization provides the diffusivity evolution in the hydraulically non-linear anisotropic medium. Following Jaeger et al. (2007) hydraulic diffusivity and permeability  $\mathbf{K}$  are related by

$$\mathbf{K} = \mathbf{D} \frac{\mu}{N}, \quad (4.13)$$

where  $N$  is a poroelastic modulus (uniaxial storage coefficient). This poroelastic modulus is related to porosity and different bulk moduli for the pore-fluid, the rock skeleton, the grain material as well as the Biot coefficient. Hence, we are able to characterize the permeability tensor for situations of a fluid injection into a rock with an arbitrary unknown pressure-dependent permeability.

### 4.2.2 Case study: Ogachi, Japan

The purpose of the borehole fluid injection experiment at the Ogachi site, Japan, was to artificially create a shallow geothermal reservoir as a hot-dry-rock (HDR) system (Ito, 2003; Kaieda et al., 2010). For this, a 1000 m deep injection well called OGC-1 was drilled almost vertically into the naturally fractured granitic basement. The last 10 m of the borehole were left uncased in order to have an open hole section from 990 m to 1000 m (Figure 4.2). In 1991, pressurized water was injected into the rock for almost 11 days. Flow rates were increased step-wise up to 13 l/s and caused wellhead pressures of at most 20 MPa (see also Figure 4.10).

As a result of the fluid injection induced seismicity has been recorded and located not only throughout the injection phase but also during the post-injection phase (Figure 4.2). Hence, we are able to analyze spatio-temporal characteristics of both periods. However, since we account for the possibility of a non-linear hydraulic transport, the fluid injection creates a heterogeneously distributed diffusivity. Consequently, the diffusivity estimate provided by both the back front and the triggering front are different from  $D_0$ . Hence, in equation 4.1 and 4.2, we replace  $D_0$  by a heuristic diffusivity estimate  $D_h$ .

To use the two previously described concepts of back front and triggering front we compute the  $r - t$  diagram of induced events (Figure 4.2). This  $r - t$  diagram includes the aseismic domain which evolves with increasing time and distance from the injection point as soon as the fluid injection is terminated. To analyze spatio-temporal characteristics of the post-injection phase we apply the aforementioned back front concept. As a result, we obtain a heuristic diffusivity estimate of  $D_{h_{bf}} = 0.02 \text{ m}^2/\text{s}$ . This scalar heuristic magnitude estimate characterizes the post-injection hydraulic transport within the reservoir rock. However, we note that this estimate does not include information about the directivity of the process. For comparison, we also consider the injection phase and analyze corresponding spatio-temporal features. We fit equation 4.1 as envelope of induced events. As a result, the triggering front provides a heuristic diffusivity estimate of  $D_{h_{tf}} = 0.08 \text{ m}^2/\text{s}$ . According to the results of Hummel and Shapiro (2012) this scalar heuristic magnitude estimate is a sensible estimate of the enhanced heterogeneously distributed diffusivity of the stimulated domain. The corresponding effective hydraulic transport is characterized by a four times larger diffusivity compared to the post-injection phase.

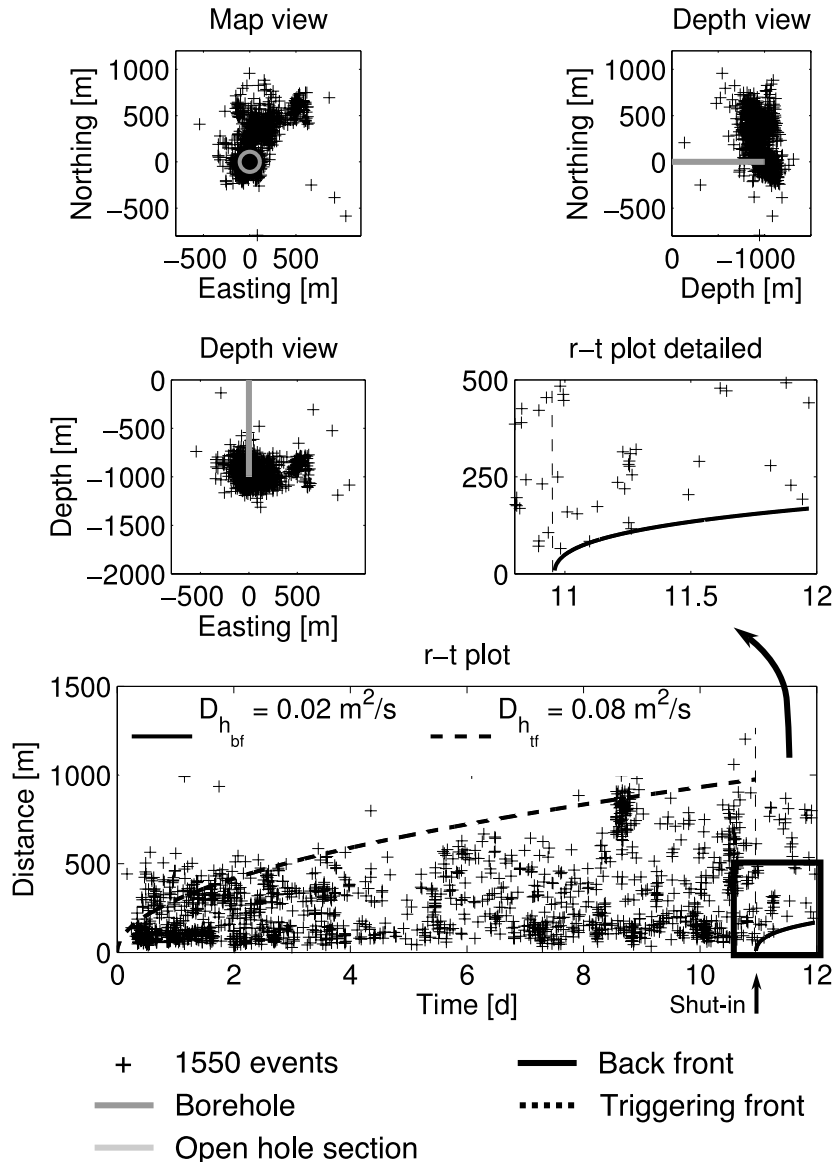


Figure 4.2: Distribution of 1550 induced events recorded during and after the 1991 stimulation experiment at the Ogachi site, Japan. With the termination of the fluid injection a developing domain of seismic quiescence evolves in the  $r - t$  diagram. Although this aseismic area seems to be quite small we note that it still includes almost 24 h of data. The back front (solid curve) provides a heuristic diffusivity estimate which is four times smaller than the diffusivity estimate from the triggering front (dashed parabola). Data are courtesy of H. Kaieda (Central Research Institute of Electric Power Industry, CRIEPI).

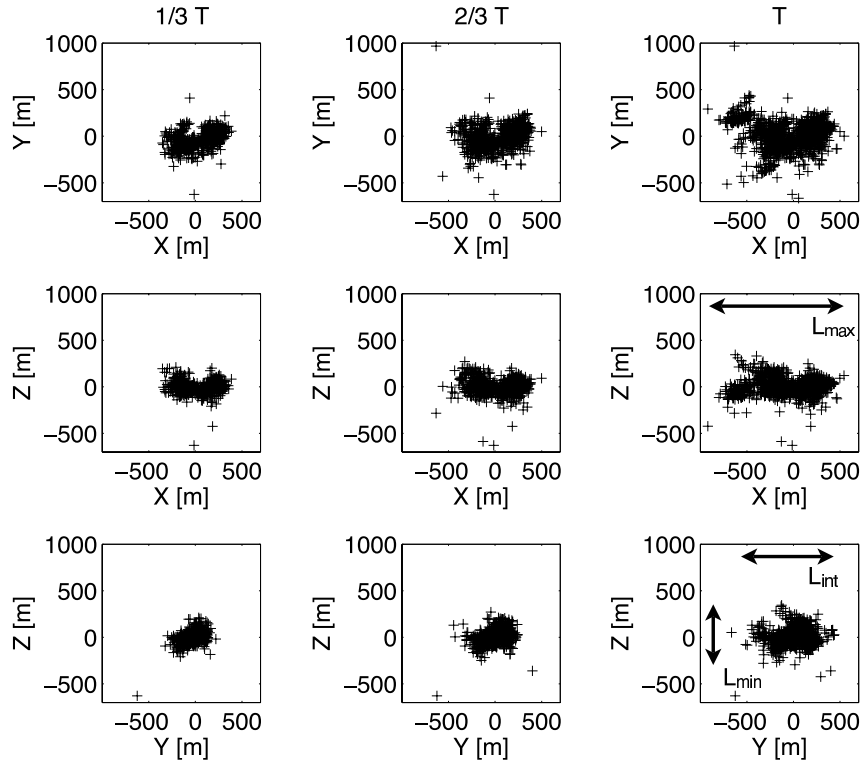


Figure 4.3: Temporal evolution of the seismicity cloud in the principal coordinate system. Vertical and horizontal scales are equal. The double arrows indicate the characteristic lengths of the seismicity cloud. These dimensions are used to reveal the directivity of hydraulic anisotropy and to normalize the event cloud into one which would have occurred in an equivalent isotropic but still non-linear medium.

To explore the cause and meaning of the observed difference between both diffusivity estimates  $D_{\text{hbf}}$  and  $D_{\text{hf}}$  we apply the prescribed transformation approach. For this we consider the seismicity cloud in the principal coordinate system (PCS). To reveal the influence of hydraulic anisotropy on the shape and geometry of the cloud we evaluate its characteristic dimensions  $L$ . We obtain  $L_{\text{max}} = 1142$  m for the  $X$ -direction,  $L_{\text{int}} = 640$  m for the  $Y$ -direction and  $L_{\text{min}} = 490$  m for the  $Z$ -direction (Figure 4.3). Following equation 4.10 these dimensions are used to determine scaling factors. With these normalizing factors we finally transform the original seismicity cloud into a cloud which would result in an equivalent hydraulically isotropic but still non-linear medium. Figure 4.4 shows how well the rescaling obtained from the final shape of the cloud works during the total process time. As the transformed event cloud develops in space and time, their geometry remains almost the same. This supports the model of a non-linear permeability with a factorized anisotropy.

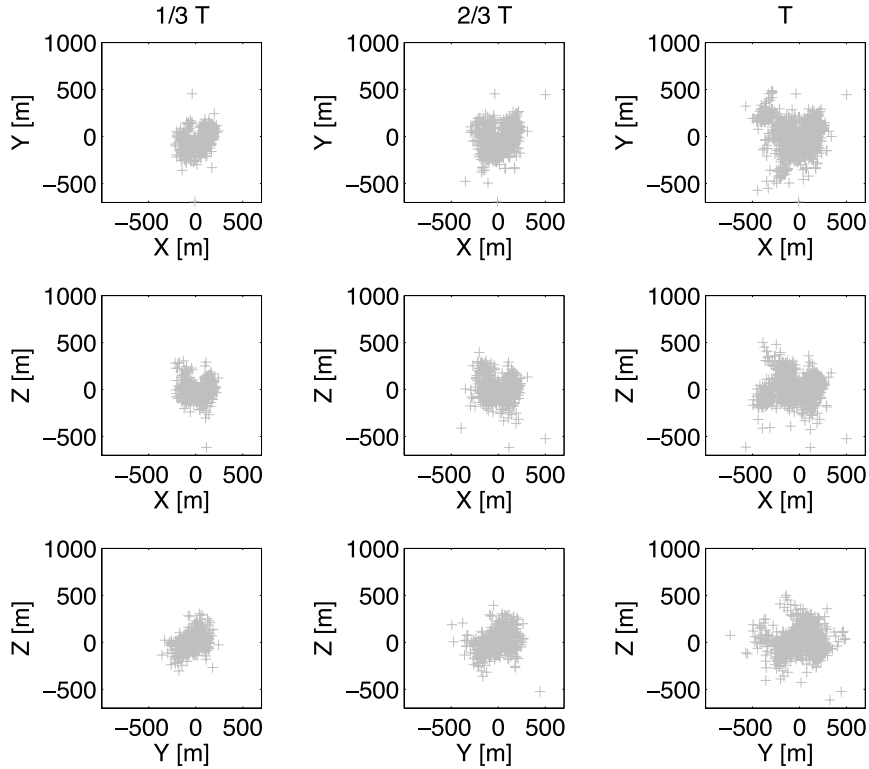


Figure 4.4: Temporal evolution of the normalized event cloud which would be obtained in a hydraulically equivalent isotropic medium. Vertical and horizontal scales are equal and the same as in Figure 4.3. With increasing time  $T$  the seismicity cloud increases in size and number of induced events while its geometry remains almost the same. Note that for all three snapshots the scaling was taken the same.

In the following we consider the transformed event cloud and characterize their spatio-temporal features. For this, we repeat the previous analysis. We first compute the  $r-t$  diagram of transformed seismicity (Figure 4.5). Since this  $r-t$  diagram also includes the aseismic area we fit equation 4.2 as envelope of the domain of seismic quiescence. As a result, the back front provides a heuristic diffusivity estimate of  $D_{\text{h}_{\text{bf}}} = 0.03 \text{ m}^2/\text{s}$ . This estimate is quite close to the corresponding one obtained from the original cloud. In contrast, fitting the triggering front parabola as envelope of induced events provides a heuristic diffusivity estimate of  $D_{\text{h}_{\text{tf}}} = 0.04 \text{ m}^2/\text{s}$ . The comparison of both magnitude estimates  $D_{\text{h}_{\text{bf}}}$  and  $D_{\text{h}_{\text{tf}}}$  shows that the corresponding effective hydraulic transport during and after stimulation is nearly the same.

Finally, the nature of the back front estimate is determined from the renormalization which allows us to identify the directivity of the hydraulic transport. Moreover, it allows to reconstruct the magnitude of the effective hydraulic diffusivity along all

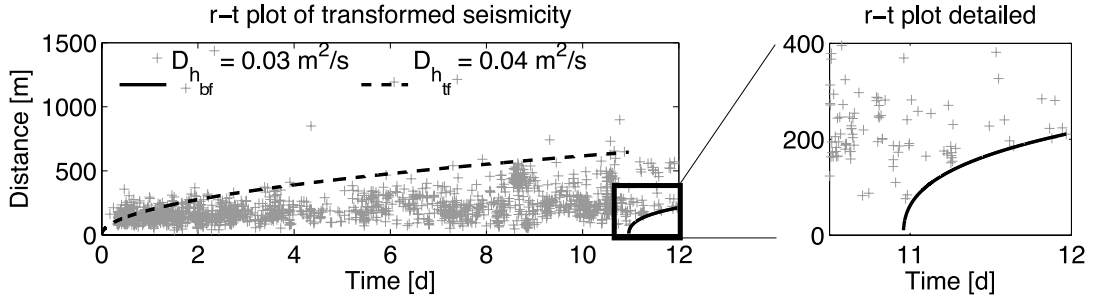


Figure 4.5:  $r - t$  diagram of seismicity which would be obtained in a hydraulically equivalent isotropic medium. For such a medium, the diffusivity estimates obtained from back front and triggering front are in agreement.

three principal axes of the diffusivity tensor. Following equation 12 we use the back front diffusivity estimate of  $D_{h_{bf}} = D_{h_{iso}} = 0.03 \text{ m}^2/\text{s}$  and obtain

$$\mathbf{D} \approx \text{diag}(D_{h_{11}}; D_{h_{22}}; D_{h_{33}}) = \text{diag}(0.08; 0.03; 0.01) \text{ m}^2/\text{s}. \quad (4.14)$$

Within the original hydraulically anisotropic non-linear medium the fastest hydraulic transport takes place in the  $X$  direction. It is characterized by an effective diffusivity of  $0.08 \text{ m}^2/\text{s}$ . For the original seismicity cloud the triggering front provided the same magnitude estimate (see Figure 4.2). As the triggering front describes the envelope of seismicity in the  $r - t$  diagram it separates the already pressure-stimulated area from the non-stimulated virgin rock. Hence, the first induced events which occur at a particular time and radial distance from the injection point must have been triggered by the pressure diffusion along the hydraulically fastest direction. Consequently, the triggering front provides a diffusivity estimate which corresponds to the largest heuristically effective hydraulic diffusivity tensor component. Therefore, the triggering front characterizes the fastest hydraulic transport.

In contrast, the slowest hydraulic transport takes place in the  $Z$  direction. It is characterized by a diffusivity value of  $0.01 \text{ m}^2/\text{s}$ . We recall that the back front has been derived for the assumption that seismic events can not be triggered at locations where the pressure has already reached its maximum. As we consider a hydraulically anisotropic medium in the principal coordinate system of the diffusivity tensor, diffusional-like pressure maxima with different velocities penetrate along the three principal directions as soon as the fluid injection has been terminated. Since the back front describes locations of the latest possible induced events they should have been triggered from the direction with the slowest diffusional relaxation. With  $0.02 \text{ m}^2/\text{s}$  this back front diffusivity estimate is very close to the reconstructed least principal effective diffusivity of  $0.01 \text{ m}^2/\text{s}$ . Consequently, the back front provides a diffusivity estimate which corresponds to the smallest hydraulic diffusivity tensor component.

At last, we convert the diffusivity tensor components into corresponding permeability values. For this we assume a uniaxial storage coefficient of  $N \approx 4.36 \cdot 10^{10}$  Pa and a dynamic fluid viscosity (at 240° C) of  $\mu = 1.2 \cdot 10^{-4}$  Pa · s (see Audigane et al., 2002). Following equation 4.13 we obtain the reconstructed permeability tensor

$$\mathbf{K} = \text{diag}(22; 8.3; 2.8) \cdot 10^{-17} \text{ m}^2. \quad (4.15)$$

Our resulting permeability estimates are in agreement with the ones given in Audigane et al. (2002)

$$\mathbf{K}_{\text{Audigane et al.}} = \text{diag}(23.7; 6.9; 5.0) \cdot 10^{-17} \text{ m}^2. \quad (4.16)$$

### 4.2.3 Case study: Fenton Hill, New Mexico

The purpose of the 1983 Phase II massive hydraulic fracturing (MHF) treatment was to create an artificial geothermal reservoir within a low permeability granitic rock (House, 1987; Fehler, 1989). In December pressurized water was injected for almost 61 h into the rock through an isolated section of the wellbore. This injection interval extended from the casing shoe at a depth of 3531 m (11585 ft) to a sand-barite plug top at a depth of 3550 m (11648 ft) (Figure 4.6). During this stimulation experiment almost 21600 m<sup>3</sup> of water were injected with flow rates high enough to cause wellhead pressures of about 48 MPa (Dreesen and Nicholson, 1985) (Figure 4.10).

As a result of the fluid injection more than 11300 events have been recorded and located with accuracies of 20 m to 30 m (House, 1987) (Figure 4.6). Since the monitoring system was in operation even after termination of the fluid injection seismic activity has also been registered for the post-injection phase. The computed  $r - t$  diagram shows the aseismic domain which evolves with increasing time and radial distance from the injection point as soon as the fluid injection has been terminated.

In the following we analyze spatio-temporal characteristics of the event cloud in the same way as we did for Ogachi. For the post-injection phase the back front (equation 4.2) provides a heuristic diffusivity estimate of  $D_{\text{hbf}} = 0.07 \text{ m}^2/\text{s}$  while for the injection phase the triggering front (equation 4.1) provides a heuristic magnitude estimate of  $D_{\text{htf}} = 0.16 \text{ m}^2/\text{s}$ . Hence, the latter effective hydraulic transport is characterized by a two times larger diffusivity compared to the post-injection phase.

Next, in the PCS, we determine the characteristic dimensions  $L$  of the seismicity cloud to  $L_{\text{max}} = 1033 \text{ m}$ ,  $L_{\text{int}} = 791 \text{ m}$  and  $L_{\text{min}} = 504 \text{ m}$  (Figure 4.7). We note that these dimensions correspond to the volume in which most events have been induced. Very large outliers are not further considered. We then apply the scaling approach to transform the cloud of hypocenters of events obtained in a hydraulically anisotropic non-linear medium into a cloud which would be obtained in an equivalent isotropic but still non-linear medium (Figure 4.8).

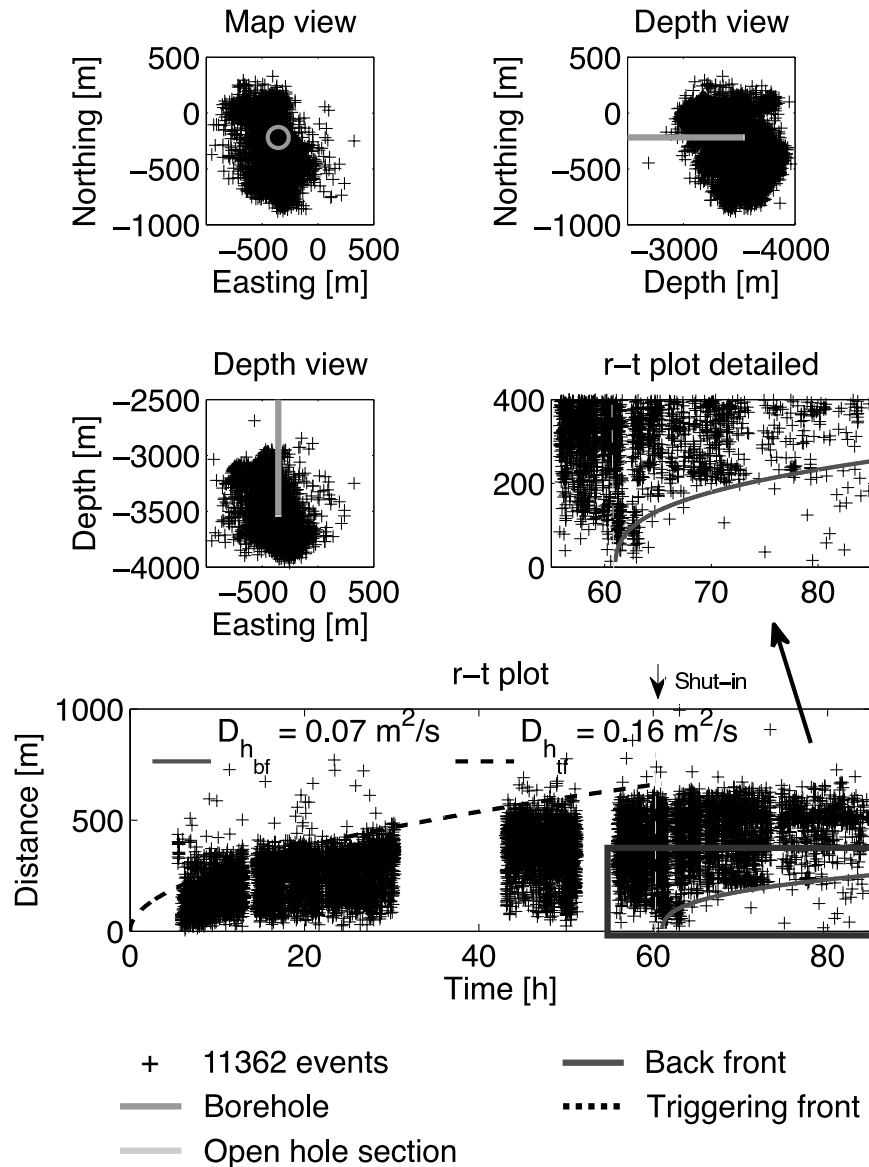


Figure 4.6: Distribution of 11362 induced events recorded during and after the December 1983 massive hydraulic fracturing treatment at Fenton Hill, New Mexico. Due to disruptions in the monitoring system there are three time periods in which seismic events could not be located (Fehler et al., 1998). These three data gaps are clearly visible in the  $r - t$  diagram. Additionally, the  $r - t$  diagram includes the domain of seismic quiescence which evolves with the termination of the fluid injection. The back front (solid parabola) provides a heuristic diffusivity estimate which is two times smaller than the diffusivity estimate from the triggering front (dashed parabola). Data are courtesy of M. Fehler (Los Alamos National Laboratory).

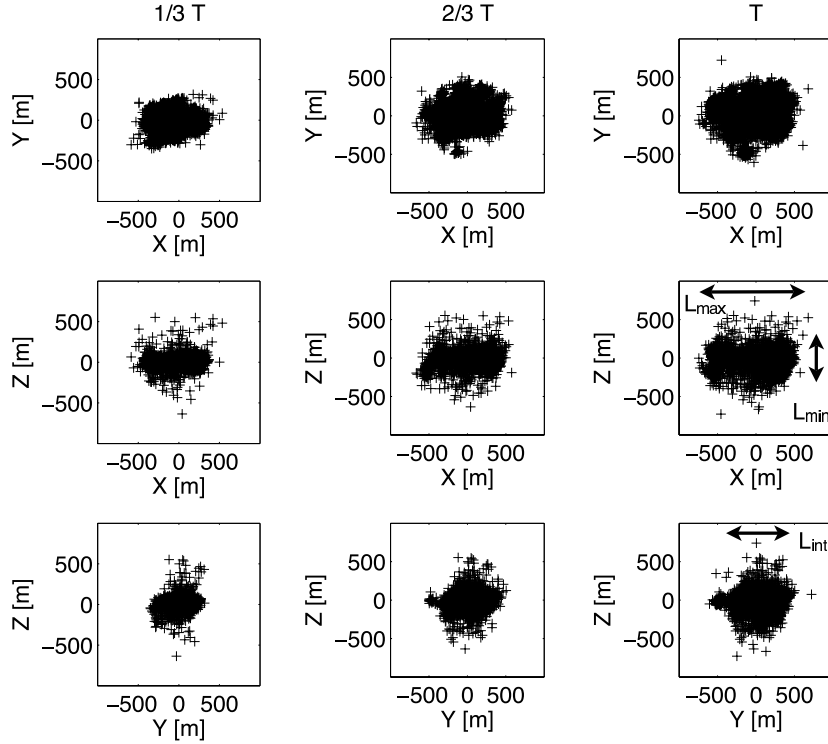


Figure 4.7: Temporal evolution of the seismicity cloud in the principal coordinate system. Vertical and horizontal scales are equal. The double arrows indicate the characteristic lengths of the seismicity cloud. These dimensions are used to reveal the directivity of hydraulic anisotropy and to normalize the seismicity cloud into a cloud which would have occurred in an effective isotropic medium.

For the transformed event cloud, back front and triggering front provide slightly different diffusivity estimates (Figure 4.9). However, with  $D_{\text{hbf}} = 0.07 \text{ m}^2/\text{s}$  and  $D_{\text{htf}} = 0.11 \text{ m}^2/\text{s}$  both estimates are still within one order of magnitude. This difference may be caused by an inaccurate determination of the characteristic dimensions.

Finally, the renormalization allows us to reconstruct the magnitude of the effective hydraulic diffusivity along all three principal axes of the diffusivity tensor. Following equation 12 we use the back front diffusivity estimate of  $D_{\text{hbf}} = 0.07 \text{ m}^2/\text{s}$  and obtain

$$\mathbf{D} = \text{diag}(D_{\text{h11}}; D_{\text{h22}}; D_{\text{h33}}) = \text{diag}(0.14; 0.08; 0.03) \text{ m}^2/\text{s}. \quad (4.17)$$

Within the original hydraulically anisotropic non-linear medium the fastest hydraulic transport takes place in the  $X$  direction. It is characterized by an effective diffusivity of  $0.14 \text{ m}^2/\text{s}$ . If we consider the original event cloud the triggering front provided a magnitude estimate of  $D_{\text{htf}} = 0.16 \text{ m}^2/\text{s}$ . This diffusivity magnitude estimate is close to the reconstructed effective diffusivity along the  $X$  direction. Consequently, we infer that the triggering front provides a diffusivity estimate which corresponds to the

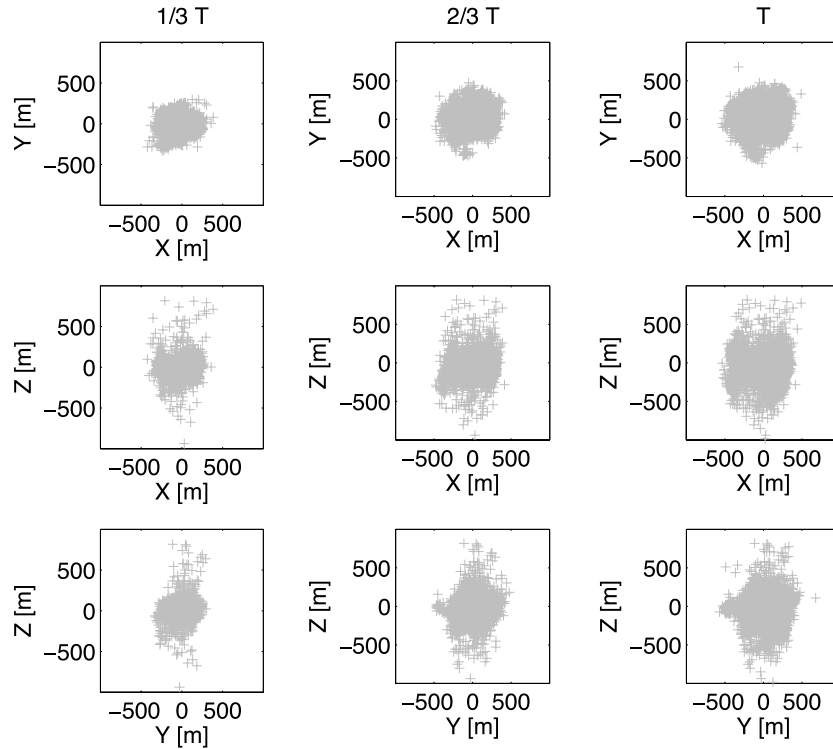


Figure 4.8: Temporal evolution of the normalized event cloud which would be obtained in a hydraulically equivalent isotropic medium. Vertical and horizontal scales are equal and the same as in Figure 4.7. With increasing time  $T$  the seismicity cloud increases in size and number of induced events while its geometry remains almost the same. Note that for all three snapshots the scaling was taken the same.

largest heuristically effective hydraulic diffusivity tensor component.

In contrast, the slowest hydraulic transport occurs in the  $Z$  direction. It is characterized by a diffusivity magnitude of  $0.03 \text{ m}^2/\text{s}$ . For the original event cloud the back front provided a diffusivity estimate of  $D_{\text{h,tf}} = 0.07 \text{ m}^2/\text{s}$ . This magnitude estimate is closer to the value of the moderate hydraulic transport along the  $Y$  direction. However, compared to the smallest diffusivity tensor component the back front estimate is of the same order of magnitude. Since seismic events can not be triggered at locations where the pressure has already reached its maximum, the latest possible events should be triggered along the direction of the slowest hydraulic transport. Thus, we conclude that the back front still provides a diffusivity estimate which corresponds to the smallest hydraulic diffusivity tensor component.

At last, we convert the diffusivity tensor components into corresponding permeability values. For this we assume a uniaxial storage coefficient of  $N \approx 1.68 \cdot 10^{11} \text{ Pa}$  and a dynamic viscosity of the reservoir fluid (salt water at  $150^\circ \text{ C}$ ) of  $\mu = 1.9 \cdot 10^{-4}$

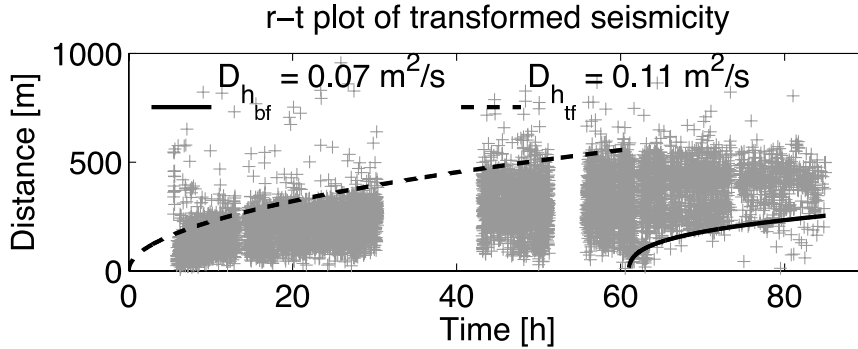


Figure 4.9:  $r - t$  diagram of seismicity which would be obtained in a hydraulically equivalent isotropic medium. For the diffusivity estimates obtained from the back front and the triggering front we observe a difference of one order of magnitude.

$\text{Pa} \cdot \text{s}$  (Shapiro et al., 2002). Following equation 4.13 we compute the reconstructed permeability tensor to

$$\mathbf{K} = \text{diag}(15.8; 9.0; 3.4) \cdot 10^{-17} \text{ m}^2. \quad (4.18)$$

The permeability magnitudes are in agreement with the ones computed from Shapiro et al. (2002).

### 4.3 Back front signatures of non-linear fluid-rock interaction

Previously, we revealed the nature of diffusivity estimates obtained by the back front in the case of hydraulically anisotropic non-linear media. We showed that for such situations the back front characterizes the slowest hydraulic transport (i.e the back front provides an estimate for the minimum principal value of the permeability tensor). So far, our analysis of post-injection induced seismicity is based on the linear diffusion back front formula (equation 4.2). However, in some cases, we observe that this back front does not describe the temporal evolution of post-injection induced events very well. To independently determine the temporal behaviour of the back front and to explore which temporal dependence would be required if the linear diffusion back front does not describe post-injection induced seismicity, we consider a simple power-law type fitting function

$$r(t) = a(t - t_0)^b. \quad (4.19)$$

Both parameters  $a$  and  $b$  are determined by fitting equation 4.19 as envelope of the domain of seismic quiescence. Figure 4.10 shows this best fit function for three different data sets including also Ogachi and Fenton Hill. For both geothermal case studies we observe that the best fit function practically coincides with the linear diffusion back

front curve. The exponents  $b$  are close to 0.36 and 0.33 representing a nearly cubic root of time dependency. This seems to be a good power-law approximation of the exact linear back front (equation 4.2).

However, for the third case study, the situation is different. This third data-set represents a hydraulic fracturing case study from the Horn River Basin. This is for sure a non-linear fluid-rock interaction. The distribution of induced seismicity indicates a classical bi-wing shape hydraulic fracture. For such a fracture its width is by far much smaller compared with its length and height. Hence, the penetration of pressure and treatment fluid into the direction normal to the fracture is typically much smaller as in parallel direction. In terms of the hydraulic transport this fracture therefore can be considered to effectively have a one dimensional geometry. Hence, the 3-D non-linear anisotropic diffusion approximation as we used here for the other case studies are non-applicable. Consequently, the determination of a post-injection phase diffusivity requires the application of the one dimensional (i.e.  $d = 1$ ) back front equation. However, this curve does not describe the spatio-temporal distribution of post-injection induced events very well. In particular, the best fit function describing the envelope of the aseismic area is characterized by a different temporal dependence. Their exponent  $b$  has a magnitude of 0.19. This is very different from  $b \approx 0.33$  as in the linear case. To find out whether a pressure-dependent hydraulic transport can describe these signatures we perform a numerical modelling.

### 4.3.1 Modelling non-linear pore-fluid pressure diffusion

First we compute the spatio-temporal distribution of the pressure perturbation. For this we consider a simplified version of equation 4.5. Following Hummel and Shapiro (2012) we account for a  $d$ - dimensional initially hydraulically homogeneous, isotropic and fluid-saturated medium. For such a medium the pressure evolution is described by the following differential equation of diffusion (see Shapiro and Dinske, 2009b):

$$\frac{\partial r^{d-1} p(r; t)}{\partial t} = \frac{\partial}{\partial r} \left( D(p(r; t)) r^{d-1} \frac{\partial p(r; t)}{\partial r} \right). \quad (4.20)$$

Equation 4.20 is formally one dimensional in terms of the radial distance  $r$ . Consequently, solutions correspond to time-dependent pressure profiles along the radial distance. This significantly simplifies the numerical modelling of non-linear pressure diffusion. However, as a draw-back, we therefore can not take into account possible non-radial heterogeneities near the wellbore and inside of the reservoir. By considering such a hydraulic isotropic medium we are also not able to account for individual fractures or fracture pathways as they are reported for instance at Barnett Shale (Fisher et al., 2002). We account for them in an effective way by replacing the fracture network by a non-linear filtration process. Additionally, equation 4.20 includes a functional dependence  $D(p)$  of the hydraulic diffusivity on the pressure perturbation.

This arbitrary functional dependence accounts for a non-linear Darcy's law which, in our case, contains either the power-law (equation 4.3) or the exponential-dependent diffusivity model (equation 4.4).

To account for post-injection induced seismicity we consider a time-dependent fluid injection. The boxcar-like injection pressure source is realized as a Dirichlet-type boundary condition (see Figure 4.11). It has a duration of  $t = t_0 = 40$  s and a magnitude of  $p_0 = 10$  Pa. Choosing an injection pressure magnitude in the order of  $10^1$  Pa instead of  $10^7$  Pa results in much faster computations and cost-effective solutions. However, this also requires that the permeability compliances  $\kappa$  are normalized to the order of  $10^{-1} \text{ Pa}^{-1}$  (according to Yilmaz et al., 1994). Following Hummel and Shapiro (2012) we account for injection pressure normalized values of  $\kappa = 0.2 \text{ Pa}^{-1}$ ,  $0.4 \text{ Pa}^{-1}$  and  $0.5 \text{ Pa}^{-1}$ . These values cover a wide range of documented permeability compliances, including the case of a highly fractured rock (Table 4.1). In contrast, for the index of non-linearity, we will consider  $n = 1, 2$  and  $3$ .

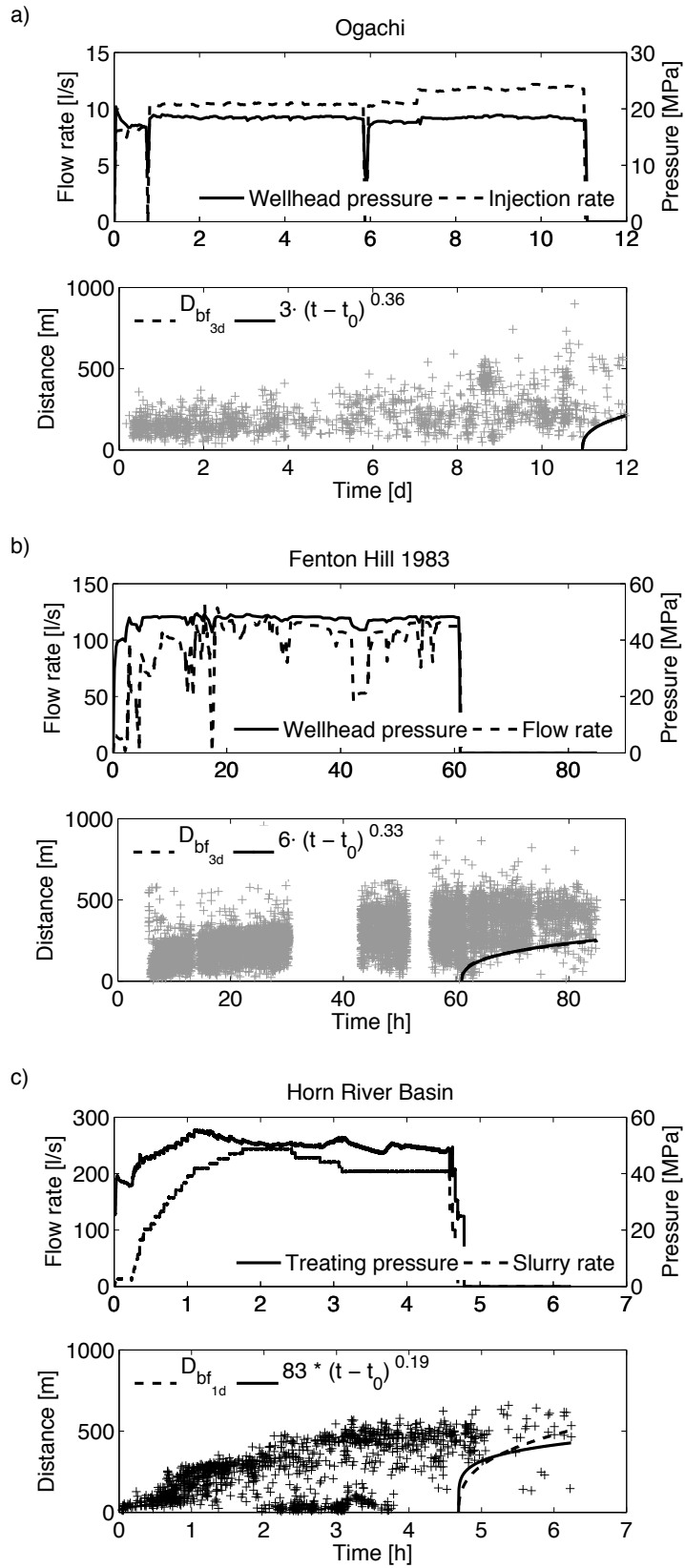
### 4.3.2 Frozen diffusivity model

After termination of the fluid injection the pressure perturbation decreases. In turn, the effective normal stress increases and the rock becomes more stable. Consequently, induced cracks and fractures close. However, fracture closing can be prevented by the use of proppant (Mader, 1989). This is normally the case in hydraulic fracturing treatments which leads to a post-injection enhanced hydraulic permeability (Economides and Nolte, 2000). To approximate the complicated hydraulic behaviour of the medium during as well as particularly after the stimulation and to account for a post-injection enhanced permeability we have to make assumptions about the hydraulic behaviour of the medium.

---

Figure 4.10: For both geothermal case studies Ogachi (a) and Fenton Hill (b) the best fit function (solid curve) practically coincides with the linear diffusion back front (dashed curve). The exponents of the best fit function (solid curve) describing the evolution of post-injection induced seismicity have exponents  $b$  of 0.36 and 0.33. However, for the hydraulic fracturing case study from the Horn River Basin (c) the best fit function describing the domain of seismic quiescence differs from the linear diffusion back front curve. Their power-law approximation has an exponent of magnitude  $b = 0.19$ . This can be seen as an indication of a pressure-dependent hydraulic transport. Data from the Horn River Basin have been donated by a sponsor of the *PHASE* consortium.

### 4.3 Back front signatures of non-linear fluid-rock interaction



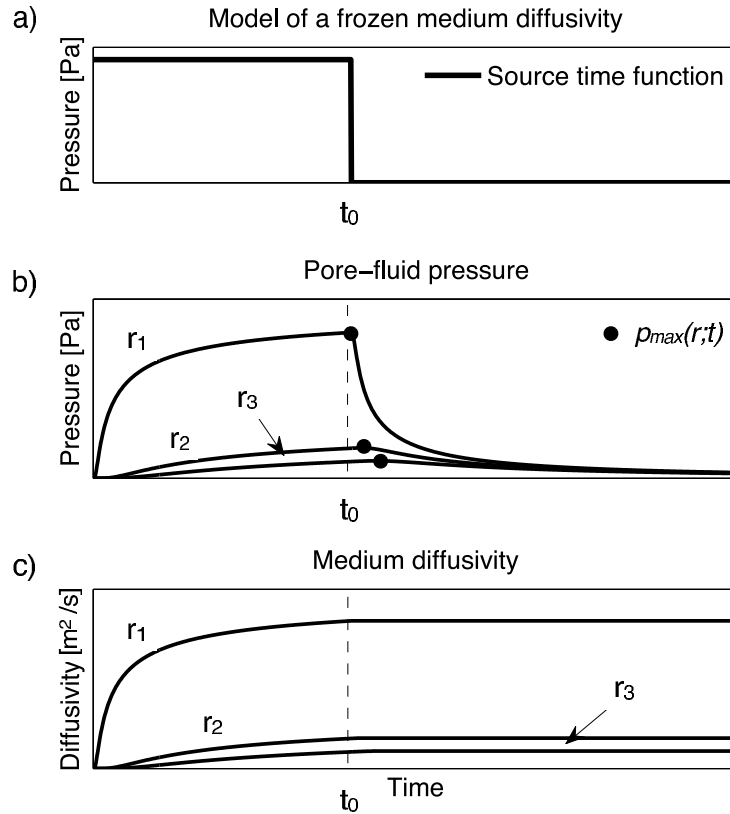


Figure 4.11: (a) Time-dependent injection pressure source function of duration  $t_0 = 40$  s. The horizontal axis represents the time  $t$ . (b) Pore pressure versus time for three different distances  $r$  ( $r_1 < r_2 < r_3$ ). After shut-in (dashed line) the pressure relaxation leads to a diffusional-like pressure wave with maxima  $p_{\max}(r;t)$  (black circles). (c) Medium diffusivity versus time for corresponding distances  $r$ . As soon as the medium diffusivity has reached its maximum  $D_{\max}(p_{\max}(r;t))$  at a certain distance the diffusivity will thereafter remain constant with  $D_{\max}(p_{\max}(r))$ .

For this, we present the following model of a frozen medium diffusivity (Figure 4.11): As a consequence of terminating the fluid injection a diffusional-like pressure wave will penetrate through the medium. At a particular location (i.e. distance from the injection point  $r$ ) and time the pressure perturbation will increase up to a specific maximum  $p_{\max}(r;t)$ . As long as the pressure increases induced cracks and fractures continue to grow. However, as soon as the pressure has reached  $p_{\max}(r;t)$  it starts to decrease. Due to its pressure dependence the medium diffusivity will have a similar behaviour as the pressure and therefore will also increase up to a maximum value  $D_{\max}(p_{\max}(r;t))$ . However, to account for a post-injection enhanced hydraulic diffusivity, we prevent  $D(p(r;t))$  to decrease thereafter. As soon as the medium diffusivity has reached its maximum at a particular cell of our medium the diffusivity will there-

after remain constant with  $D_{\max}(p_{\max}(r))$ . We note that this resulting post-injection enhanced diffusivity is a function of the distance. With increasing distance from the wellbore this modified medium diffusivity decreases from cell to cell. Such a behaviour corresponds to cracks and fractures with a post-injection distance-dependent aperture. Close to the wellbore fractures remain almost open. Thus, they have a high post-injection enhanced diffusivity. As soon as the distance from the borehole increases fractures close and their aperture becomes smaller. Therefore, the diffusivity of the fractures decreases. To our knowledge this is a new type of model to approximate the complicated behaviour of a post-injection enhanced diffusivity.

### 4.3.3 Pore pressure profiles

As a result of our modelling we first obtain the spatio-temporal evolution of the pressure perturbation induced by the fluid-injection. In the following we analyze these pressure profiles which we obtain as solutions of corresponding non-linear diffusion equation 4.20. Figure 4.12 shows six examples of computed pressure fields for both pressure-dependent diffusivity models in 1-, 2- and 3-D media. The remaining pore pressure profiles are included in the appendix.

Up to the end of the injection phase the pressure profiles show the same characteristics as reported in (Hummel and Shapiro, 2012). This includes the effect of geometrical spreading which, for increasing dimension, leads to the spatial pressure decay close to the source. Additionally, with increasing non-linearity, the pressure profiles penetrate deeper into the formation as a result of the pressure enhanced hydraulic diffusivity. For the given magnitudes of  $n$  and  $\kappa$  the medium pressurization is stronger for power-law diffusion than for exponential diffusion (most noticeable in 1-D and 2-D).

With the termination of the fluid injection at the time  $t_0$  the pressure at the source becomes zero. However, the diffusional-like wave is still able to further penetrate into the medium. With increasing distance from the wellbore, the profiles increase up to a specific pressure maximum. Thereafter, they decrease and end up in specifically shaped tips whose geometry depends on the type of non-linear fluid-rock interaction. For the power-law diffusion model the tips of the profiles are characterized by a distinct pressure step. Ahead, the pressure perturbation is still zero and the medium has not yet been pressurized. In contrast, for the exponential diffusion model, the tips of the profiles show a smooth transition. Another interesting feature affects the geometry of the post-injection pressure field itself. The character of the pressure evolution changes with increasing dimension in the following way. In 1-D, the shape of the profiles is characterized by a pressure increase which occupies more than half of the total penetrated distance. Hence, the pressure decrease takes place only over a relatively short distance. In 2-D, the pressure increases up to its maximum over a distance which is nearly the same as required for its decrease. However, in 3-D, the pressure firstly increases stepwise-like in the immediate vicinity of the source and decreases thereafter while occupying most of the penetrating distance.

### 4.3.4 Seismicity triggering and analysis of spatio-temporal characteristics

To generate synthetic clouds of seismic events we follow the approach of Rothert and Shapiro (2003) and Hummel and Müller (2009). The triggering process is realized as a comparison of the computed spatio-temporal pressure evolution with a failure criterion. This statistically distributed failure criterion is described by the so-called criticality field  $C(r)$ . For this we assume that the rock contains pre-existing randomly distributed critically stressed cracks. To realize the strength (or stiffness) of these cracks we subdivide our medium into cells. Each cell corresponds to a centre of an individual crack. We randomly assign each crack to a critical pressure perturbation  $C$  necessary for rock failure. The values of critical pressure perturbations are equally distributed between  $C_{\min}$  and  $C_{\max}$ . In such a way, high criticality values represent stable cracks while small criticality values represent weak and unstable cracks. Hence, if the pressure perturbation exceeds the local criticality value  $C(r)$  an event is generated. We set the lower bound to  $C_{\min} > 0$  Pa and the upper bound to the same order as the injection pressure source,  $C_{\max} = 10$  Pa. In such a way, critical pressures are broadly distributed which corresponds to reality.

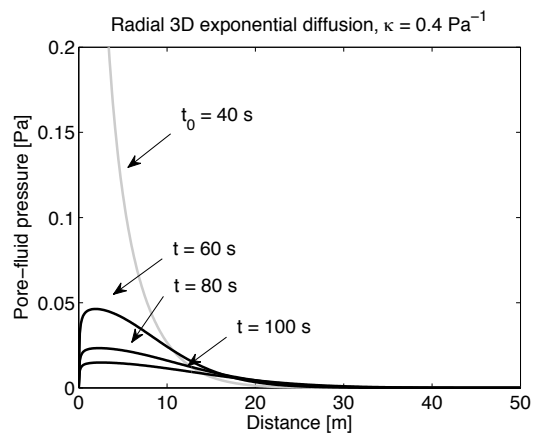
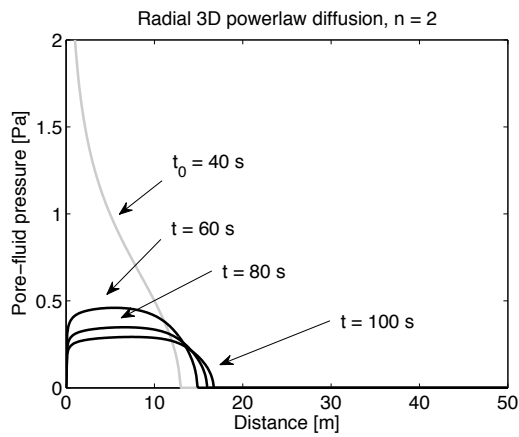
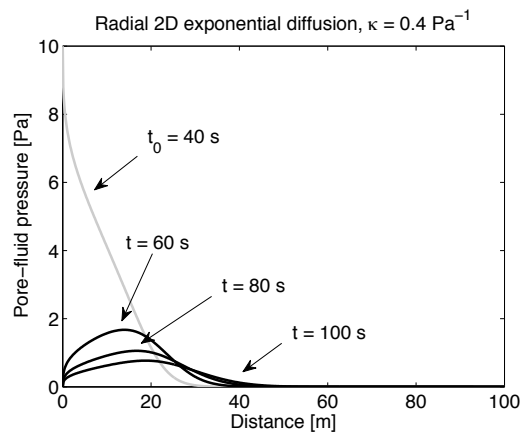
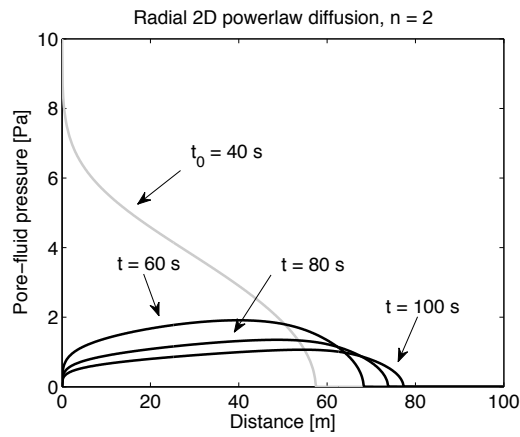
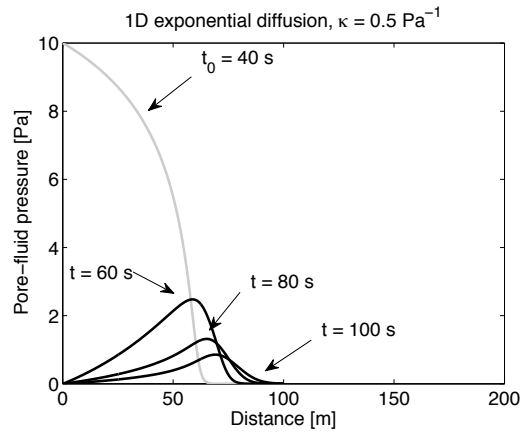
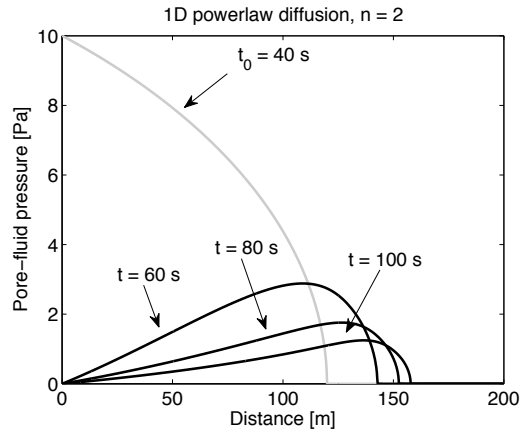
After having generated synthetic event clouds for different non-linear fluid-rock interactions we analyze corresponding spatio-temporal characteristics. In particular, we focus on the back front and its microseismic signatures. For each event cloud, we fit equation (4.2) as envelope of the domain of seismic quiescence in the  $r - t$  diagram. In this way we obtain a heuristic diffusivity estimate  $D_{\text{hbf}}$ .

However, to account for the possibility that the linear diffusion back front curve does not describe the envelope of corresponding aseismic domain very well, we numerically determine at which position the actual back front has to be located.

---

Figure 4.12: Snapshots of pressure profiles for different indices of non-linearity  $n$  and permeability compliances  $\kappa$ . The left column shows examples of profiles for the power-law relation in 1-, 2- and 3-D. The right column shows examples of profiles for the exponential relation, also for 1-, 2- and 3-D media. The light grey profile always represents the pressure state immediately before shut-in at  $t_0 = 40$  s. After termination of the fluid-injection the pressure decreases. However, the diffusional-like pressure wave further penetrates into the medium. While the shape of the pressure profiles depends on the type of non-linear fluid-rock interaction, the spatio-temporal evolution and geometry of post-injection pressure fields is controlled by the frozen medium diffusivity model.

### 4.3 Back front signatures of non-linear fluid-rock interaction



As seismicity triggering is supposed to occur only for increasing pressure perturbations, the actual back front location is defined by tracking the spatio-temporal pressure maxima  $p_{\max}(r; t > t_0)$ . We note that the locations of these pressure maxima depend on the non-linearity of the process. Therefore, the actual position of the back front depends also on the index of non-linearity  $n$  or the permeability compliance  $\kappa$ . Consequently, each event cloud has its own specific domain of seismic quiescence which is confined by a back front of an unknown temporal dependence.

To determine this temporal dependence we consider the already introduced best fit function. By fitting equation 4.19 to the  $r_{p_{\max}} - t_{p_{\max}}$  values we obtain a certain magnitude for the exponent  $b$ . Since this exponent  $b$  controls the temporal dependence of the best fit function it simultaneously provides the requested information about the character of the back front.

Finally, in order to have a comparison to the back front diffusivity estimate  $D_{\text{hbf}}$ , we determine a heuristic diffusivity estimate  $D_{\text{htf}}$  by fitting the triggering front (equation 4.1) as envelope of injection phase induced events. As in the aforementioned case studies of Ogachi and Fenton Hill this heuristic magnitude estimate characterizes the effective hydraulic transport during the stimulation.

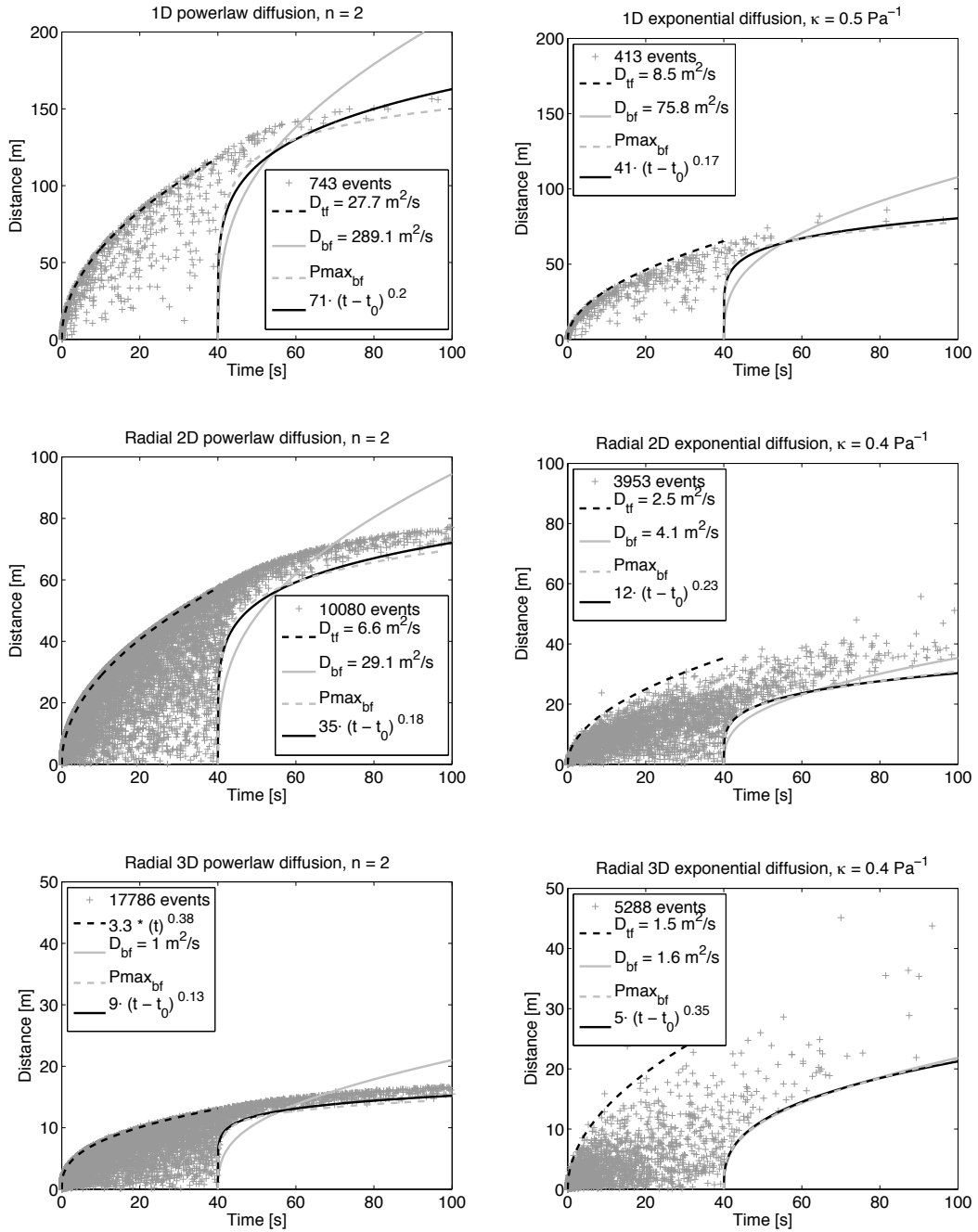
### 4.3.5 Synthetic seismicity

Following the aforementioned triggering approach we compute  $r - t$  diagrams of synthetic seismicity for different indices of non-linearity  $n$  and permeability compliances  $\kappa$  (Figure 4.13). We observe that clouds of seismicity based on the power-law diffusion model show a sharp upper boundary, where simultaneously events strongly accumulate. Ahead, there are no seismic events because the rock has not yet been pressurized.

---

Figure 4.13: Synthetic clouds of microseismic events based on the pressure evolutions shown in Figure 4.12. The accumulation of events at the upper boundary is controlled by the geometry and the tips of the pressure profiles. In most cases the linear diffusion back front (grey solid curve) does not describe the spatio-temporal characteristics of post-injection induced events very well. In order to do so the back front should match the numerically determined location given by the pressure maxima (grey dashed curve). The temporal dependence of such a modified back front can be assessed from the best fit function (black solid curve). Except for a weak non-linearity, the temporal dependence of the back front becomes power-law dependent where the exponents  $b$  decrease with increasing non-linearity. Only for the event cloud based on 3-D exponential diffusion, the linear diffusion back front curve still describes the envelope of corresponding aseismic domain reasonably well.

### 4.3 Back front signatures of non-linear fluid-rock interaction



This distinct upper boundary of the cloud results from the shape of the tips of the pressure profiles. For the power-law model, the pressure at the tips drops to zero and thus clearly separates the already stimulated from the virgin rock. This distinct demarcation is responsible for the sharp upper contour of the cloud. In comparison, seismicity clouds based on the exponential diffusion model have a more diffuse upper boundary. This effect is due to the smooth transition occurring at the tips of corresponding pressure profiles.

With termination of the fluid injection a growing domain of seismic quiescence evolves in corresponding  $r - t$  diagrams. This domain becomes more pronounced as the non-linear fluid-rock interaction increases. However, in most cases, fitting the linear diffusion back front curve (equation 4.2) as envelope of this aseismic area provides unsatisfying results. Except of a very weak non-linearity and three dimensional exponential diffusion, this curve inadequately describes spatio-temporal characteristics of post-injection induced events. In order to compensate this misfit, the back front should have a different temporal dependence. This is confirmed by determining the best fit function for the actual location of the back front. Their exponents  $b$  can have a magnitude down to 0.13.

However, for a very weak non-linearity and 3-D exponential diffusion, the situation is different. For these cases, the linear diffusion back front (equation 4.2) describes the spatio-temporal evolution of corresponding post-injection phase seismicity reasonably well. Simultaneously, the linear diffusion back front therefore practically coincides with the best-fit function. This interesting result is due to the fact that the effect of geometrical spreading is approximately the same or larger compared to the effect of a pressure-dependent permeability. In other words, the non-linearity (i.e. pressure dependence) is too weak to make itself felt against the geometrical spreading. This can be seen best for 3-D exponential diffusion. There, the diffusivity estimates obtained from the linear diffusion back front and the triggering front are in agreement with the initial background medium diffusivity,  $D_{\text{hbf}} \sim D_{\text{htf}} \sim D_0$ . For the case of a zero pressure dependence this background medium diffusivity  $D_0$  would completely describe the corresponding hydraulic transport. Consequently, this causes an ambiguity in terms of the governing fluid pressure transportation. Strictly speaking, fitting event clouds with the linear diffusion back front does not allow to conclude that the process of pore pressure equilibration is only governed by linear diffusion. A pressure-dependent hydraulic transport can lead to nearly the same back front signature. However, practically, this ambiguity is of minor importance. The impact of non-linearity on the diffusion is fairly insignificant and therefore can be almost neglected. We note that for 3-D exponential diffusion and permeability compliances  $\kappa \gg 1$  non-linear effects should become apparent. Admittedly, to our knowledge, such large magnitudes are not reported.

In contrast, we observe an interesting effect for the power-law diffusion models. As soon as we consider 3-D media, we observe that the character of the triggering front changes from a square root behaviour into a more and more cubic root of time dependence. As discussed in Hummel and Shapiro (2012) such a cubic root of time dependence is a distinct indication for a pressure-dependent hydraulic transport (as demonstrated in Hummel and Shapiro, 2013). This, however, should not be confused with the corresponding temporal dependence of the back front. In 3-D media, the aforementioned analysis has shown that a best-fit function with a nearly cubic root of time dependence represents an appropriate power-law approximation for the exact linear diffusion back front. Consequently, the governing post-injection induced hydraulic transport is pressure-independent.

### 4.3.6 Synthetic vs. real seismicity

So far, the modelling of synthetic microseismic back front signatures showed that its temporal dependence can significantly differ from the linear diffusion back front. However, the numerical modelling also allows us to perform parametric studies. In this way, the magnitude of a single quantity is determined in a simple manner by which the real data can be explained best. Since the synthetic event distributions based on the power-law dependent diffusivity model contain a very thin and restricted domain of post-injection phase seismicity, that so far has not been observed in real data, we will not consider these event clouds in the further course of our paper. In contrast, the event distributions based on the exponential diffusion model contain a much wider domain of post-injection induced seismicity. Together with the observation that the synthetic events are distributed more diffusively, these event distributions are already quite close to what we observe in reality. Consequently, the parameter study is about the permeability compliance  $\kappa$ . By repeating our modelling for different values of the permeability compliance we expect to obtain back front signatures which are close to the ones observed at Ogachi, Fenton Hill and the Horn River Basin (Figure 4.10). There, the corresponding power-law approximation of the back front is characterized by a temporal dependence of

$$r_{\text{Ogachi}} = 3 \cdot (t - t_0)^{0.36}, \quad (4.21)$$

$$r_{\text{Fenton Hill}} = 6 \cdot (t - t_0)^{0.33}, \quad (4.22)$$

and

$$r_{\text{Horn River Basin}} = 83 \cdot (t - t_0)^{0.19}. \quad (4.23)$$

As the distribution of induced events for Ogachi and Fenton Hill is clearly three dimensional, we constrain the parameter study to the situation of  $d = 3$ . In contrast, for Horn River Basin, the distribution of induced seismicity suggests an effectively one dimensional hydraulic transport. Consequently, we restrict the parameter study to the situation of  $d = 1$ . Figure 4.14 shows the results of our parameter study together

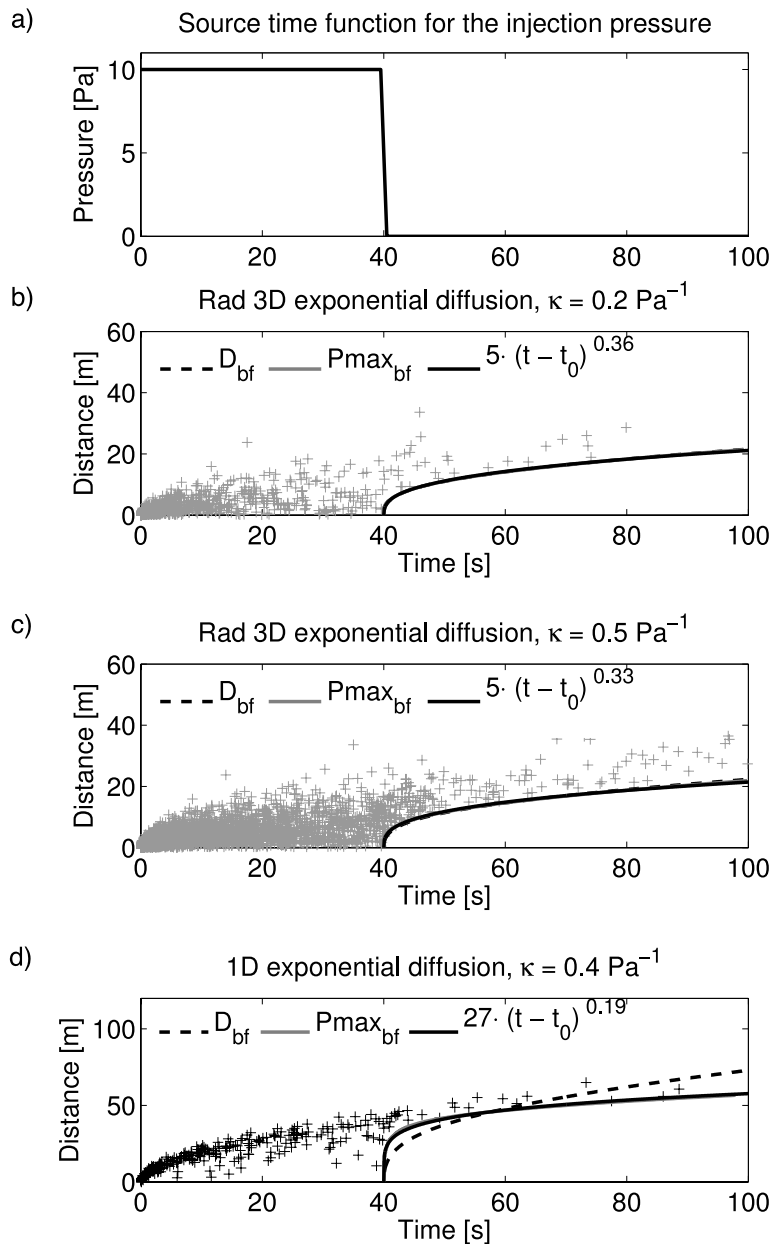


Figure 4.14: Despite the simplified source time function (a) and geometry of our model the spatio-temporal characteristics of synthetic event clouds are in agreement with the ones observed in real data. The parameters of the best fit function obtained for synthetic seismicity in (b), (c) and (d) are consistent with the corresponding ones obtained for Ogachi, Fenton Hill and Horn River Basin (see Figure 4.10 and equations 4.21 to 4.26).

with the analysis of spatio-temporal characteristics. For each data set the power-law approximation of the back front is described by a best fit function according to

$$r_{3D, \kappa=0.2 \text{ Pa}^{-1}} = 5 \cdot (t - t_0)^{0.36}, \quad (4.24)$$

$$r_{3D, \kappa=0.5 \text{ Pa}^{-1}} = 5 \cdot (t - t_0)^{0.33}, \quad (4.25)$$

and

$$r_{1D, \kappa=0.4 \text{ Pa}^{-1}} = 27 \cdot (t - t_0)^{0.19}. \quad (4.26)$$

Although the geometry and numerical modelling are both quite simple we obtain best fit functions that are in agreement with the ones determined for real data. In particular, the temporal dependencies given by the exponents  $b$  even coincide.

In this way, the post-injection hydraulic transport at Ogachi seems to be well described by a three dimensional exponential-dependent diffusion with an injection pressure normalized weak permeability compliance of  $\kappa = 0.2 \text{ Pa}^{-1}$ . For the massive hydraulic fracturing experiment at Fenton Hill, the post-injection hydraulic transport seems to be well described by a three dimensional exponential-dependent diffusion with an injection pressure normalized strong permeability compliance of  $\kappa = 0.5 \text{ Pa}^{-1}$ . If the applied average injection pressure magnitude of about 27 MPa (documented by Brown et al., 1999) is taken into account, the correspondingly renormalized magnitude of  $\kappa$  is recomputed to  $185 \text{ GPa}^{-1}$ . This is in good agreement compared with the reported permeability compliance magnitude of up to  $196 \text{ GPa}^{-1}$  (Table 4.1).

For the Horn River Basin hydraulic fracturing case study, the spatio-temporal characteristics of post-injection induced events seem to be well described by one dimensional exponential diffusion with an injection pressure normalized permeability compliance of  $\kappa = 0.4 \text{ Pa}^{-1}$ . However, for both geothermal case studies we observe, that the linear diffusion back front practically effectively coincides with their nearly cubic root of time-dependent power-law approximation.

Consequently, this leads to the already mentioned ambiguity in terms of the governing hydraulic transport. In contrast to an exponential-dependent pore pressure diffusion, a much simpler linear diffusion type hydraulic transport is also capable to explain the spatio-temporal evolution of post-injection induced events. This has been shown by our synthetic seismicity clouds based on 3-D exponential diffusion. However, the agreement of the obtained permeability compliance with independent results suggest, that at least for Fenton Hill, the hydraulic transport is governed by non-linear diffusion.

### 4.3.7 Frozen versus non-linear hydraulic medium behaviour

Besides the frozen medium diffusivity model, we also implemented and tested another hydraulic medium behaviour. In this realization, the fluid-rock interaction of the post-injection phase remains non-linear. Instead of freezing the local medium diffusivity as soon as the pressure perturbation has reached its maximum, we now explicitly allow  $D(p)$  to decrease thereafter. In other words, the medium diffusivity will imitate the course of the pressure perturbation throughout the entire experiment.

For such a realization we observe a slightly different geometry of the pressure fields, particularly in 1-D and 2-D. The rise and fall of the pressure profiles is more pronounced compared to those based on the frozen medium diffusivity model (Figure 4.15). Although both hydraulic models are realized in a different way, their corresponding pressure profiles and spatio-temporal characteristics are very close to each other, especially in 3-D. This again can be attributed to the strong effect of geometrical spreading which dominates against the influence of non-linearity.

However, despite the fact that the non-linear diffusivity model is easier to numerically implement, it is limited in such a way that it can not really account for a post-injection enhanced hydraulic medium behaviour, especially for situations in which proppant is being used. This is because the realization of a non-linear diffusivity model corresponds to a medium in which fractures close from the injection point into the direction of fracture propagation as soon as the pressure perturbation becomes zero. As this situation corresponds to a less realistic scenario, the non-linear diffusivity model might only be applicable in very special situations. In contrast, the frozen medium diffusivity model captures the physics of a post-injection enhanced hydraulic transport. Hence, as demonstrated before, it is able to explain and to reproduce spatio-temporal characteristics of real stimulation including hydraulic fracturing induced microseismic data.

## 4.4 Conclusion

We studied the termination of seismicity induced by non-linear fluid-rock interaction. For this, we carried out a comprehensive analysis of the behaviour and parameterization of the back front for situations in which permeability is a function of the pressure. To reveal what type of diffusivity estimates are provided by the back front in the case of a hydraulically anisotropic non-linear medium we applied a normalization approach. Based on a real data supported model of a non-linearity and factorized anisotropy this approach allows to reconstruct the principal components of the diffusivity tensor. Analyzing microseismic data being recorded at Ogachi and Fenton Hill we showed that the back front characterizes the least hydraulic transport (i.e the back front provides an estimate for the minimum principal component permeability tensor).

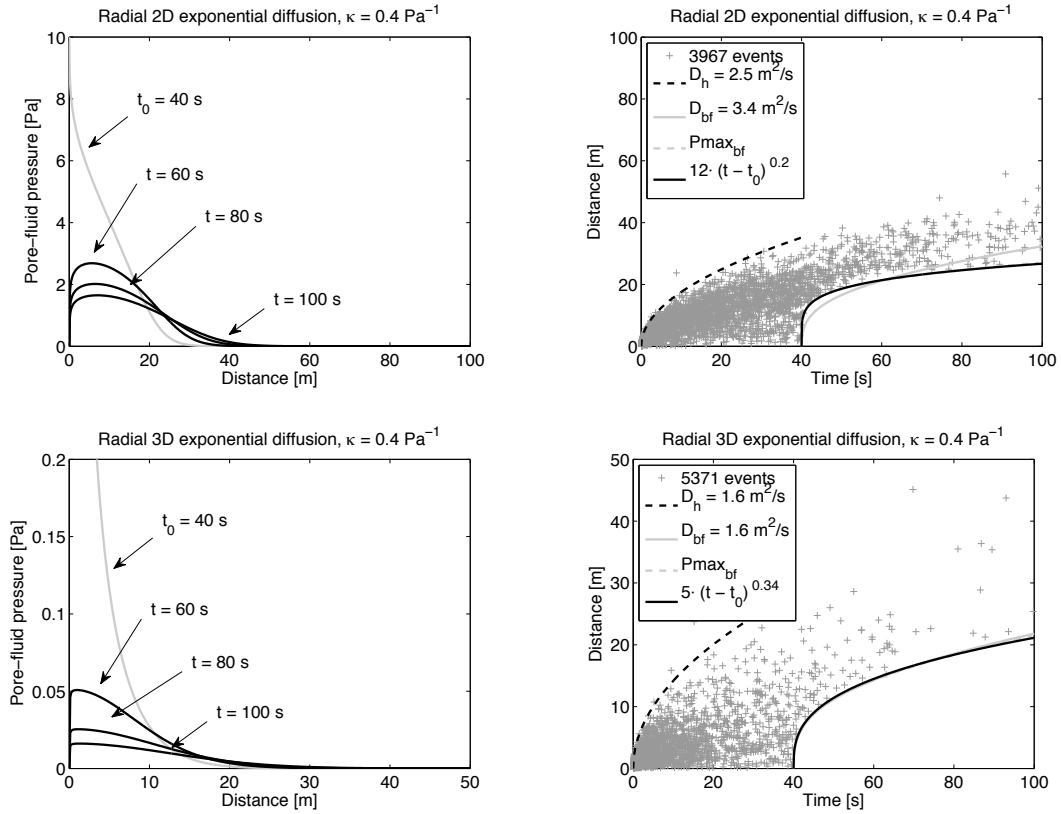


Figure 4.15: Pore pressure profiles and corresponding synthetic event clouds based on the non-linear diffusivity model. Although the geometry of the profiles slightly differs from those of the corresponding frozen medium diffusivity model the spatio-temporal characteristics of both event clouds are almost the same, especially in 3-D. There, the effect of geometrical spreading dominates against the effect of non-linearity. Hence, the linear diffusion back front is in agreement with its nearly cubic root of time-dependent power-law approximation which both well describe spatio-temporal characteristics of post-injection induced seismicity. However, as the non-linear diffusivity model corresponds to a medium realization in which fractures close from the injection point into the direction of the fracture propagation, it is less applicable as the frozen diffusivity model.

Further, we also demonstrated that the linear diffusion back front sometimes does not describe spatio-temporal characteristics of post-injection induced seismicity very well. This is a strong indication for a non-linear fluid-rock interaction. To explain this observation we performed a numerical modelling based on a pressure-dependent hydraulic transport. For the non-linear fluid-rock interaction we considered two models describing a power-law and an exponential pressure dependence of hydraulic diffusivity. Additionally, to account for a post-injection enhanced hydraulic

transport, we introduced a model of a frozen medium diffusivity. After solving corresponding non-linear diffusion equations we generated clouds of synthetic seismicity.

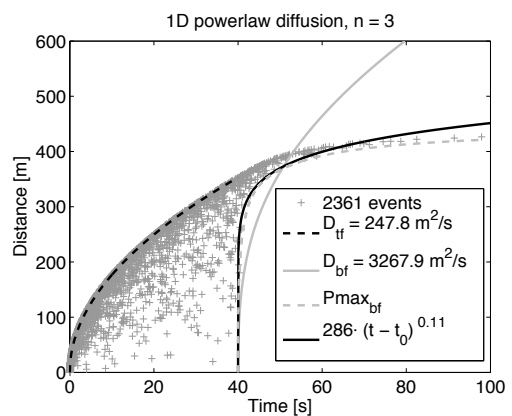
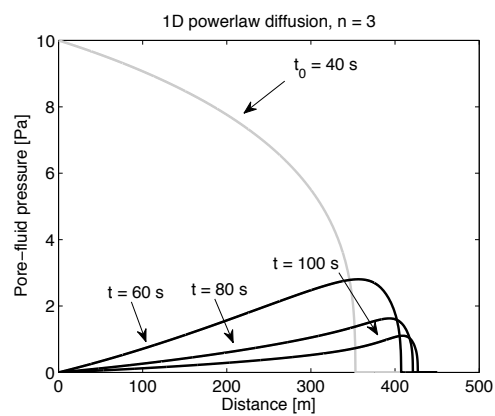
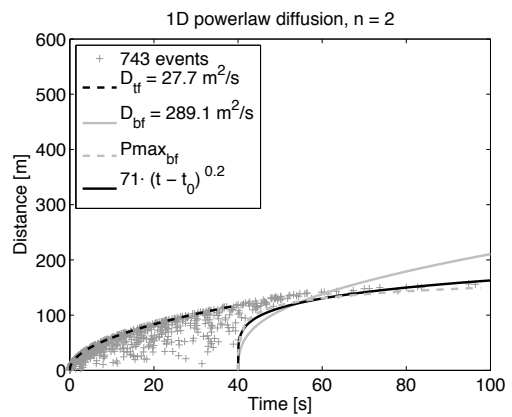
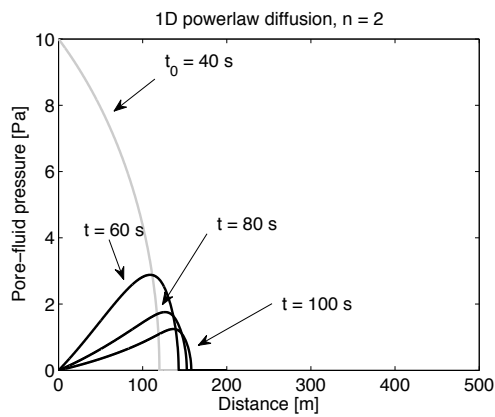
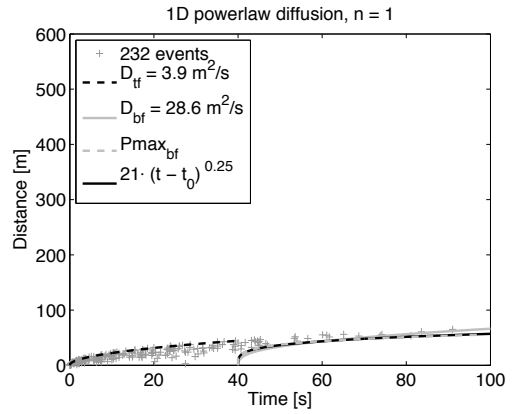
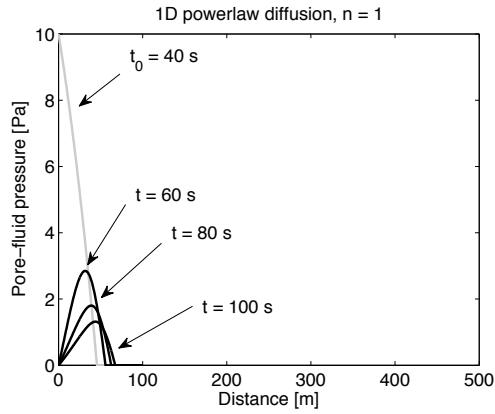
Analyzing their spatio-temporal characteristics, we found that the linear diffusion back front is only applicable for a weak non-linearity and three dimensional exponential diffusion. For such situations, the effect of geometrical spreading dominates against the impact of a pressure-dependent permeability on the diffusion. As a result, the post-injection hydraulic transport can be effectively described by the simpler linear diffusion where a cubic root of time-dependent power-law function is a good approximation of the exact back front. This seems to be the case for the two geothermal case studies Ogachi and Fenton Hill. However, for a strong non-linear fluid-rock interaction like the hydraulic fracturing, the situation is different. There, we revealed that the back front deviates from its linear diffusion signature. This also has been observed in synthetic event clouds, which show similar spatio-temporal characteristics as the ones observed in real data from the Horn River Basin. Consequently, a strong non-linear fluid-rock interaction reveals itself either by a cubic root of time-dependent triggering front or by a back front which deviates from the cubic root of time dependency.

Hence, we conclude that the behaviour of the back front is indicative for the model of non-linear fluid-rock interaction and the model of a frozen permeability. As this frozen medium permeability model accounts for a post-injection enhanced hydraulic transport as well as leads to reproducible real data supported back front signatures, it captures the physics associated with the post-injection hydraulic medium behaviour of borehole fluid injections. Ultimately, non-linear pore pressure diffusion is able to explain seismicity triggering not only for the injection phase but also for the post-injection phase.

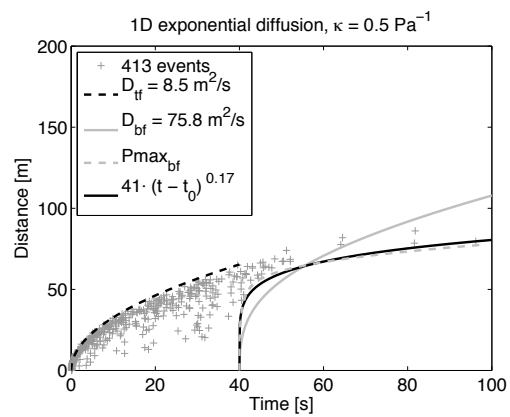
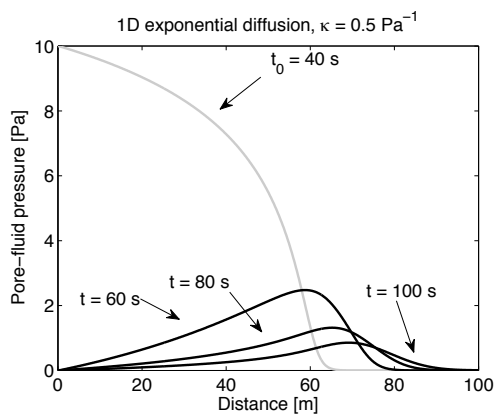
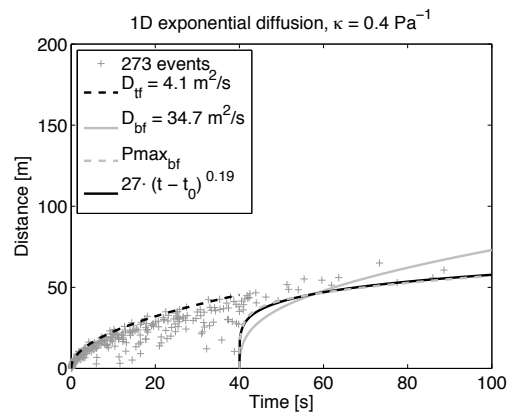
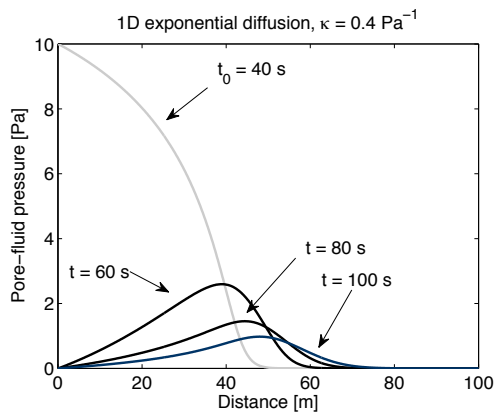
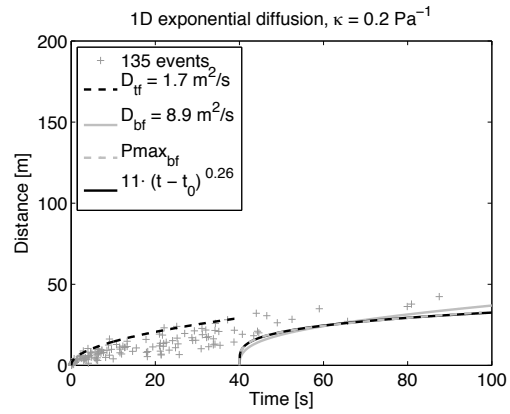
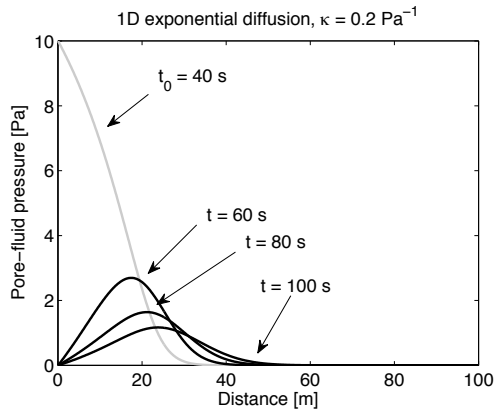
## Acknowledgments

We thank the Federal Ministry for the Environment, Nature Conservation and Nuclear Safety (BMU) as sponsor of the MAGS project (Förderkennzeichen 0325191A-F) and the sponsors of the *PHASE* consortium for supporting the presented research.

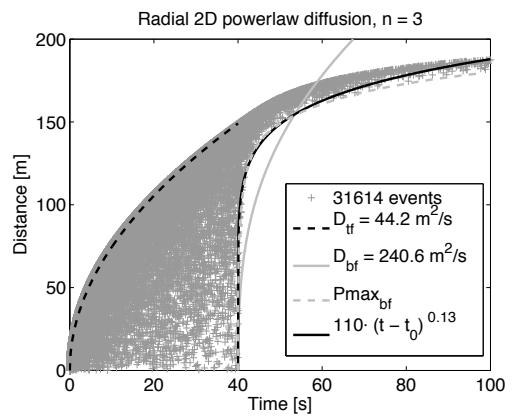
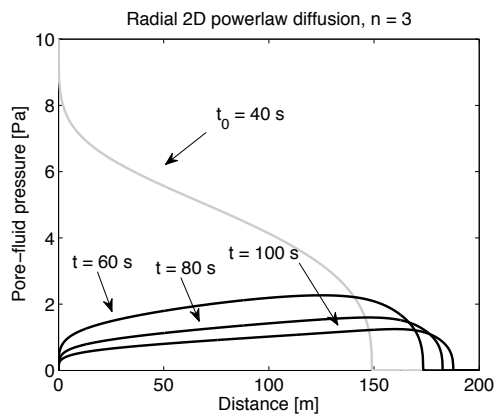
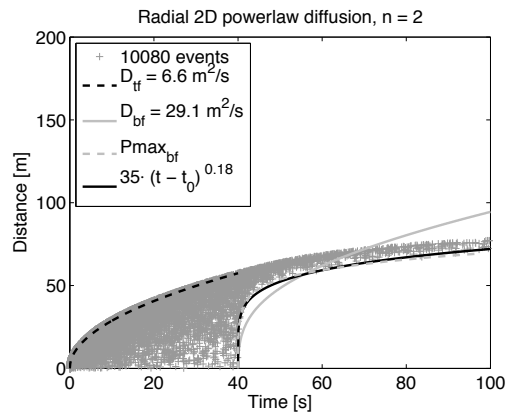
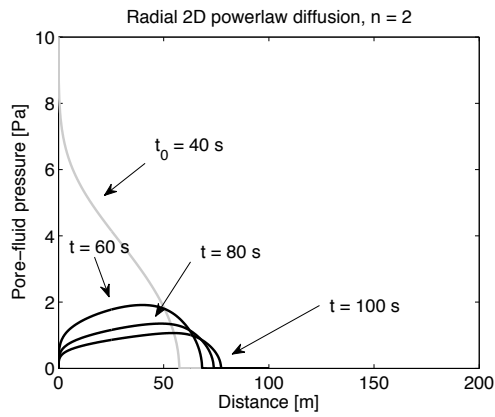
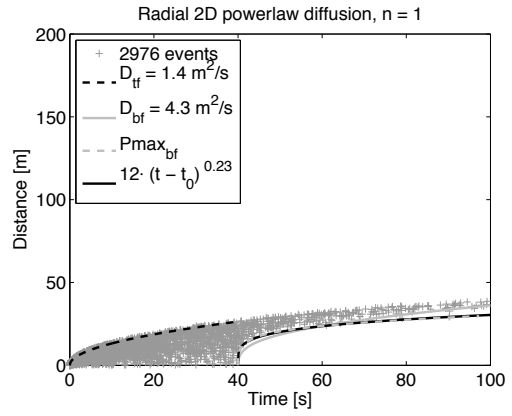
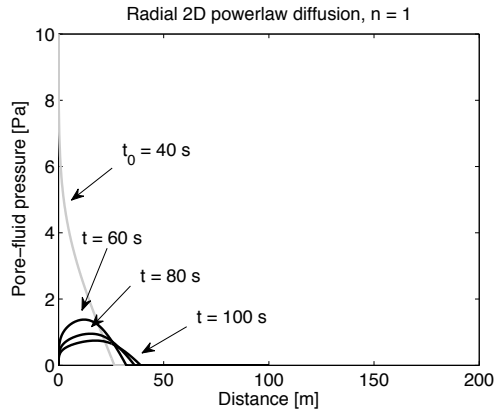
## 4.5 Appendix: Remaining pressure profiles and clouds of synthetic seismicity



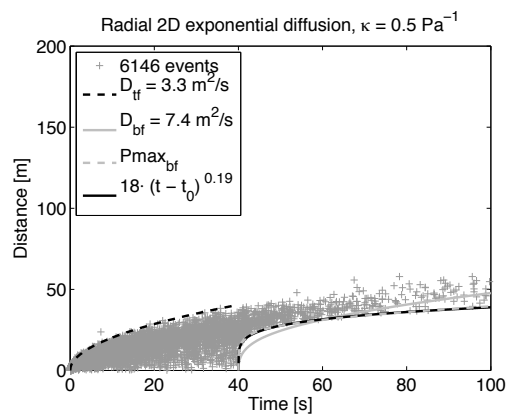
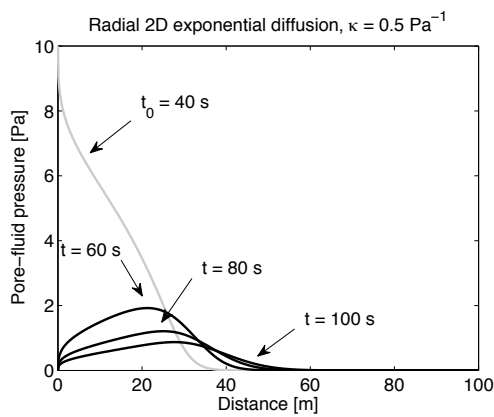
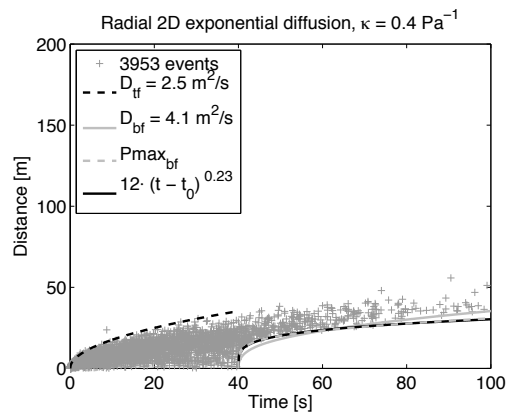
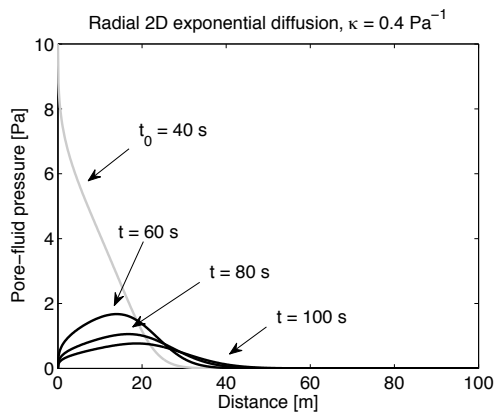
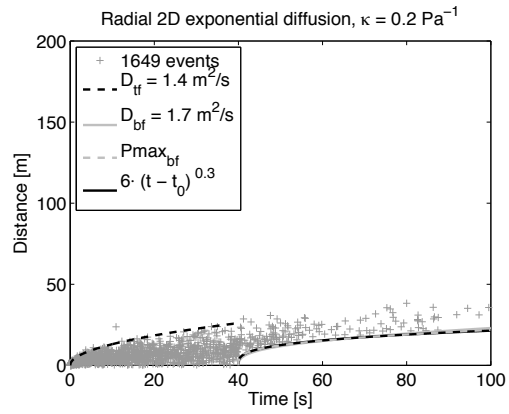
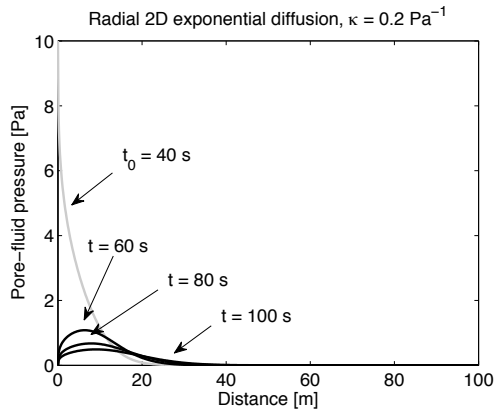
## 4 Back front of seismicity induced by non-linear fluid-rock interaction



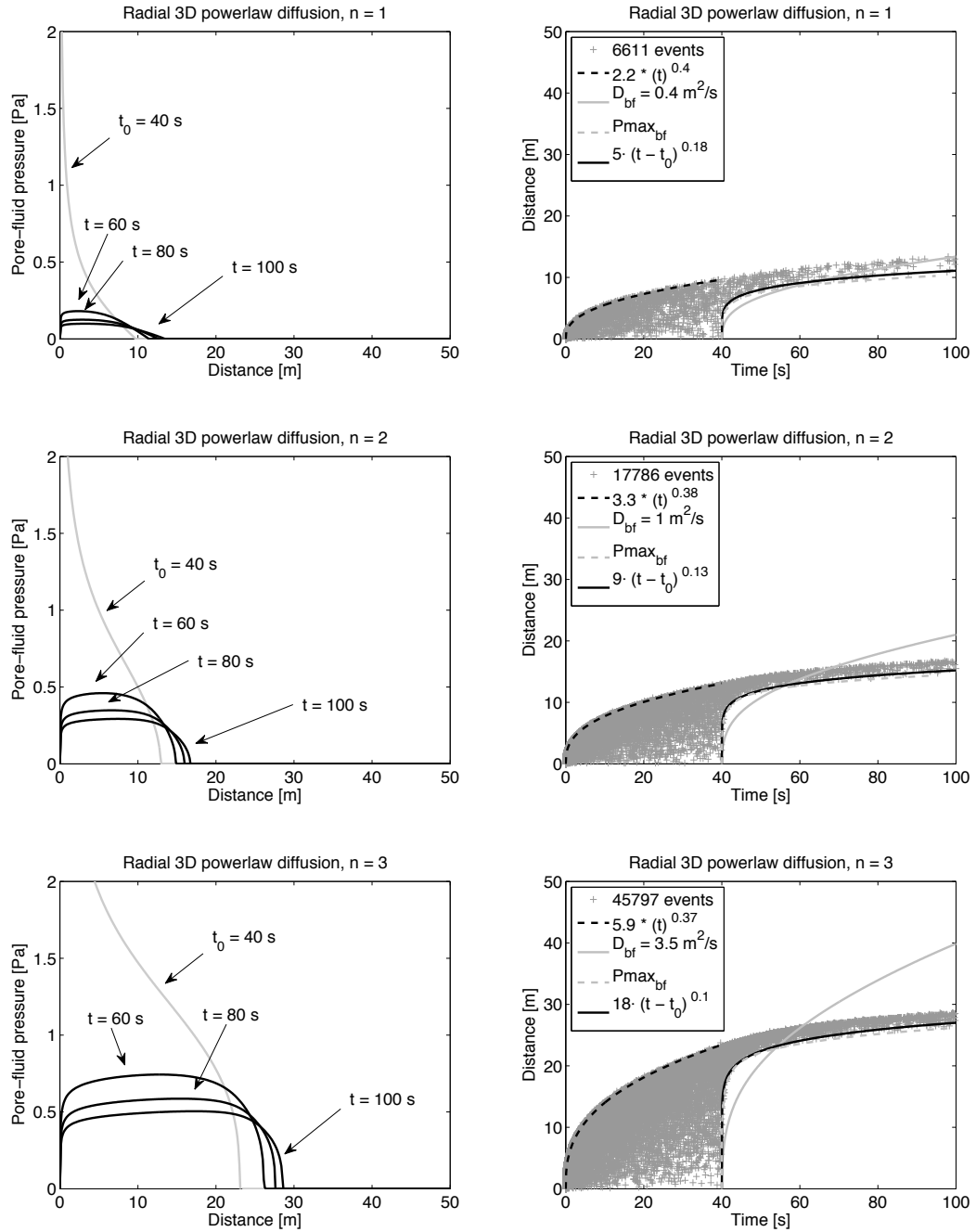
## 4.5 Appendix: Remaining pressure profiles and clouds of synthetic seismicity



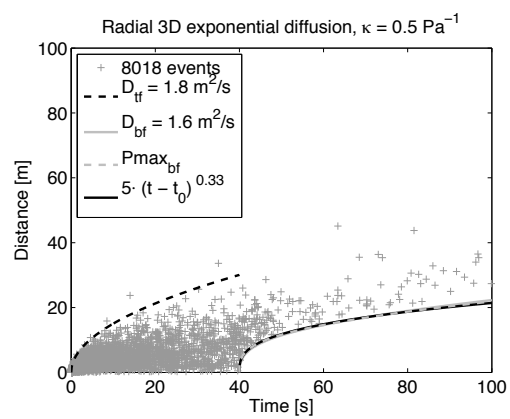
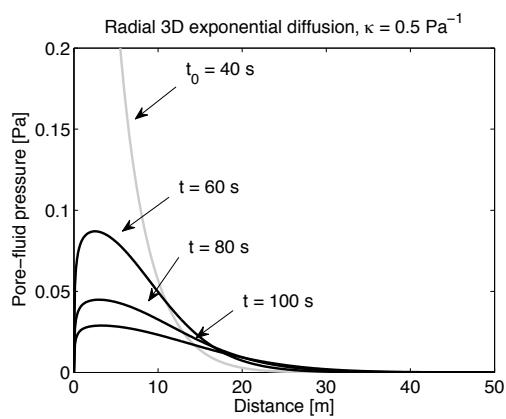
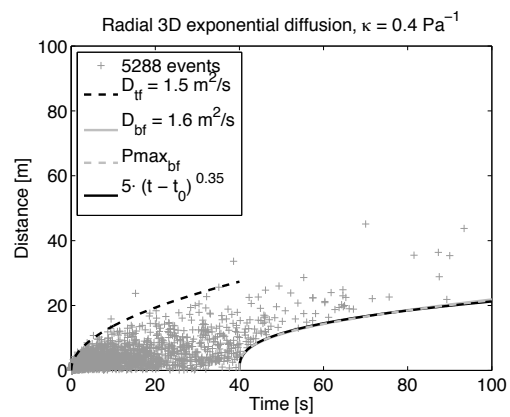
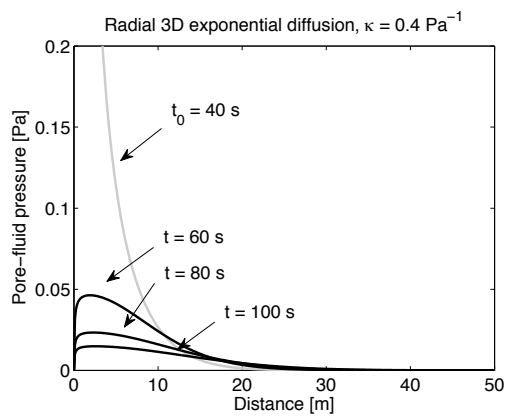
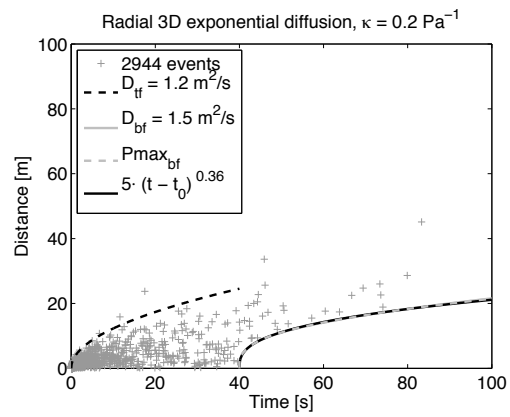
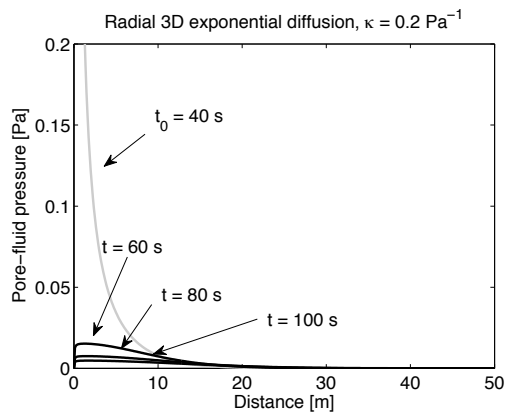
## 4 Back front of seismicity induced by non-linear fluid-rock interaction



## 4.5 Appendix: Remaining pressure profiles and clouds of synthetic seismicity



## 4 Back front of seismicity induced by non-linear fluid-rock interaction



# Chapter 5

## Conclusions and perspectives

This thesis provides a comprehensive study about a pressure-dependent hydraulic transport as a model for fluid injection induced earthquakes. For this, the seismicity-based reservoir characterization (SBRC) approach has been further developed into the direction of the important non-linear generalization. So far, this approach allowed to quantify the in-situ permeability of the stimulated rock volume from the spatio-temporal distribution of induced seismicity. Simultaneously, hydraulic transport properties have been supposed to be constant with time and pressure. However, field and laboratory experiments give evidence of the significant pressure sensitivity of rock hydraulic properties. Since a pressure-dependent diffusivity causes the diffusion equation to become non-linear, this consequently impacts seismicity triggering as well as the estimation of the permeability in a way, which so far has not yet been extensively analyzed and quantified.

Motivated by field and laboratory observations, a power-law and an exponential dependence of the diffusivity on the pressure perturbation were considered in this study. The power-law model was shown to be suitable for situations in which the initial permeability can be almost neglected. In contrast, the exponential model was found to be appropriate for rocks with a non-negligible initial diffusivity. Integrating both models into newly developed numerical simulation workflows, non-linear diffusion equations were solved to generate synthetic distributions of induced events. The analysis of their spatio-temporal characteristics revealed that the triggering front concept still holds for the case of a pressure-dependent hydraulic transport. However, instead of providing an in-situ diffusivity estimate of the rock, the triggering front was found to characterize the medium not before but after stimulation including hydraulic fracturing of the rock.

Furthermore, these numerical experiments also demonstrated that the temporal dependence of the triggering front is governed by the particular model in use. In agreement with scaling relations obtained from dimensional analysis, a linear and exponential-dependent diffusion both lead to a square root of time dependent triggering front. For the power-law diffusion model, this character can yet change into

a cubic root of time dependency. In other words, a time-dependent triggering front which is different from the square root is a clear indication of a non-linear diffusional pressure relaxation and therefore of a pressure-dependent hydraulic diffusivity. Despite its simplicity, this finding provides a practical value-adding opportunity of characterizing the fluid-rock interaction of a reservoir. Therefore, this discovery can be easily implemented into the value chain of the industry which, according to some of the *PHASE* sponsors, has already been the case.

One exemplary event catalog showing such a non-linear fluid-rock interaction is the Barnett Shale hydraulic fracturing data set. This data set has been processed and compared with results from numerical simulations to investigate the applicability of the power-law diffusion model in detail. To account for the effect of hydraulic anisotropy on the distribution of induced events, the real medium was hydraulically approximated by a new model of a non-linear and factorized anisotropic permeability. Although this model assumes that the pressure dependence itself is independent of a specific direction, it is found to be confirmed by the microseismic data under consideration. Based on this factorized model, a normalization approach was developed which transforms clouds of hypocenters of events obtained in a hydraulically anisotropic non-linear medium into a cloud which would be obtained in an equivalent isotropic but still non-linear medium. When applied to Barnett Shale seismicity, the spatio-temporal analysis confirmed that a cubic root of time dependent triggering front better describes the data than a square root parabola.

To explain corresponding spatio-temporal features, numerical simulations based on a power-law dependent nonlinear fluid-pressure diffusion were performed. A new modelling approach was presented which allows to compute calibrated pressure evolutions for (almost) constant flow rate data. This provides an estimate for the uniaxial storage coefficient and therefore permits to compute the permeability evolution inside the fracture stimulated reservoir. Following this approach, synthetic seismicity distributions were generated which show similar spatio-temporal features as the ones from the Barnett Shale. For an index of non-linearity  $n = 7$ , the behaviour of the envelope was found to be in agreement with the triggering front behaviour of Barnett Shale seismicity. Hence, it was proven that non-linear fluid-pressure diffusion in the fractured domain can explain seismicity triggering. Moreover, the hydraulic transport inside the fracture stimulated rock as well as the fluid-rock interaction were quantified in quite detail. The computed permeability values were found to increase up to the order of  $10^{-3}$  -  $10^{-1}$  darcy. Since so far no field data driven values of experience for the index of non-linearity  $n$  were available, a lower bound estimate for this particular case study has been determined.

Finally, the impact of a pressure-dependent hydraulic transport on post-injection induced seismicity was comprehensively explored. For this, the character and parametrization of the back front were analyzed. The application of the further

---

developed aforementioned normalization approach to seismicity induced at Ogachi and Fenton Hill allowed to determine and reconstruct the main components of the permeability tensor. In such a way, an anisotropic hydraulic transport has been quantified from the characteristic geometry of the corresponding seismicity cloud. This enabled to compare the diffusivity estimate obtained from the back front with the components of the reconstructed diffusivity tensor. As the back front was found to provide an estimate for the minimum principal value of the permeability tensor, it therefore characterizes the least hydraulic transport.

However, to explain the observation that for some situations the linear diffusion back front does not describe the temporal evolution of post-injection induced seismicity very well, synthetic seismicity distributions were generated on the basis of numerical simulations. For this, a new model of a so-called frozen medium diffusivity was developed and implemented. This model explicitly accounts for a post-injection enhanced hydraulic transport which is one of the major objectives of hydraulic stimulation including hydraulic fracturing treatments. The analysis of spatio-temporal characteristics of synthetic event distributions showed that the linear diffusion back front is only applicable for a weak non-linearity and three dimensional exponential diffusion. For such situations, the post-injection hydraulic transport can therefore be effectively described by the simpler linear pore pressure diffusion. As observed for the two geothermal case studies of Ogachi and Fenton Hill, a cubic root of time-dependent power-law function is then a reasonable approximation of the exact back front. In contrast, for situations corresponding to a strong non-linear fluid-rock interaction like the hydraulic fracturing, the situation was found to be different. As shown for the Horn River Basin data set, the back front then deviates from its linear diffusion signature.

In such a way, it was proven that the behaviour of the back front is indicative for the model of non-linear fluid-rock interaction and the model of a frozen permeability. As this frozen medium permeability model accounts for a post-injection enhanced hydraulic transport as well as leads to reproducible real data supported back front signatures, it captures the physics associated with the post-injection hydraulic medium behaviour of borehole fluid injections.

Consequently, this comprehensive analysis about a pressure-dependent hydraulic transport as a model for fluid injection induced earthquakes has demonstrated that a non-linear diffusional relaxation of the pressure perturbation is able to explain seismicity triggering for both the injection as well as post-injection phases. The results obtained in this thesis therefore contribute to a better understanding of the physics of borehole fluid injections and associated earthquakes. Hence, integrating these findings into reservoir simulations will provide not only value-adding opportunities for an enhanced data analysis and interpretation. Simultaneously, it will also contribute to a better understanding of fluid migration necessary for the successful management, operation, and exploration of geo-energy resources.

### Perspectives

During the course of this thesis additional ideas for future development emerged. The implementation of these ideas would contribute to further improve our understanding of the physics and processes of borehole fluid injections and associated earthquakes. However, their realization would go beyond the scope of this work. Nevertheless, the presented approach and its results may hopefully stimulate additional research into the following directions.

#### **Transition from power-law to exponential-dependent diffusion model**

This thesis demonstrated that seismicity triggering based on the power-law dependent diffusivity model is supported by real data. As shown in chapter 3, the spatio-temporal characteristics of computed synthetic seismicity distributions were found to almost coincide with the ones obtained for Barnett Shale. However, in contrast to the injection phase, these synthetic event distributions show unusual post-injection characteristics. After termination of the fluid injection the spatio-temporal distribution of synthetic events is limited to a narrow domain. For the aforementioned case studies of Ogachi, Fenton Hill and Horn River Basin, the spatio-temporal distribution of post-injection induced events is much wider. Moreover, such a broader distribution of events also can be observed at Basel (Dinske et al., 2009), Canyon Sands (Fischer et al., 2008), Cotton Valley (Parotidis et al., 2004; Dinske et al., 2010) and Soultz-sous-Forêts (Parotidis et al., 2004). Since such a broader distribution of post-injection induced events is obtained for the exponential diffusion model one could study seismicity triggering caused by a combined non-linear hydraulic transport. Until now, it remains unclear if seismicity triggering can be explained by a power-law dependent pressure diffusion which becomes exponential-dependent as soon as the fluid injection is terminated.

#### **Effect of heterogeneous medium properties**

As current numerical models account for an initially hydraulically homogeneous diffusivity, these existing models can be extended to account for initially heterogeneously distributed medium properties. In this way, combined effects of a pressure-dependent and initially heterogeneously distributed diffusivity on seismicity triggering can be explored. The realization of heterogeneous transport properties can be done according to the approach of Dinske et al. (2013). They first determine the porosity-permeability structure from borehole logging measurements. For this, they follow the works of Pechinig et al. (1997) and Pape et al. (1999). Then, they use the permeability-diffusivity relation of Rudnicki (1986) to finally compute media of a spatially correlated hydraulic diffusivity. Simultaneously, this hydraulic heterogeneity supports the development of flow paths which can cover a wide range of possible causes and origins. For instance, depending on their size, they can represent near-wellbore irregularities as well as embedded small to large-scale fractures. They both contribute to an infiltration-caused enhanced hydraulic transport. By taking into

---

account the pressure dependence of hydraulic diffusivity, these flow paths would additionally become pressure-dependent. Hence, numerical experiments would allow to study such flow-focusing phenomena in more detail.

### **Implementation of other types of boundary conditions**

In addition to the boundary conditions which already have been considered in this thesis, effects of a power-law dependent injection rate on the hydraulic transport can be further investigated. For such injection sources and the power-law dependent diffusivity model Shapiro and Dinske (2009b) already derive theoretical relations for the triggering front behaviour. Based on these theoretical relations further source-related effects on seismicity triggering can be studied if such injection sources are numerically realized. Additionally, following Shapiro and Dinske (2009b), this approach could also be extended to account for the post-injection phase. In such a way, a dimensional analysis could be applied in order to find theoretical relations describing the pressure and injection source-dependent behaviour of the back front.

### **Accounting for fluid losses**

With increasing numerical effort even more complex models can be realized. For instance, one can also go along the direction of realizing an additional secondary pressure-dependent diffusivity. Such a secondary hydraulic diffusivity could effectively describe effects related to fluid losses which play an important role during stimulation experiments and hydraulic fracturing treatments. Especially in the latter case, leak-off highly influences the fracturing efficiency. For example, if not controlled properly, fluid leak-off during hydraulic fracturing treatments can exceed up to 70 % of the injected volume (see for instance Penny et al. (1985); Dinske et al. (2010) and the Appendix A). For conventional reservoirs, this leak-off is governed by the formation matrix (Britt et al., 1994) and can be mitigated by fracturing fluid additives (Hawsey and Jaccobs, 1961; Ely, 1985; Thompson et al., 1992; Mader, 1989; Renpu, 2011). In contrast, for naturally fractured reservoirs, dilating cracks and fissures mainly dominate leak-off which simultaneously becomes pressure-dependent (Warpinski, 1991; Britt et al., 1994; Barree and Mukherjee, 1996). To further explore and account for fluid loss effects on seismicity triggering one can follow the idea of the so-called Carter model. This simple model assumes a hydraulic fracture which is embedded into an infinite homogenous porous medium. Additionally, flow (i.e. leak-off) is supposed to occur only normal to the fracture plane (Howard and Fast, 1957). Hence, as a first order approximation, this flow can be represented by the secondary pressure-dependent diffusivity model acting perpendicular to the orientation of the hydraulic fracture.

### **Realization of a hydraulically non-linear anisotropic 3D medium**

Ultimately, the final challenge for the future will be the successful implementation of a three dimensional hydraulically heterogeneous anisotropic and pressure-dependent

medium. So far, the computational power necessary to resolve the tips of the non-linear pressure profiles has not been available. Hence, the scaling approach has been introduced which transforms clouds of hypocenters from a hydraulically anisotropic medium into a cloud which would be obtained in an equivalent hydraulically isotropic but still non-linear medium. However, since the computational resources are constantly increasing, a future consideration of three dimensional hydraulically heterogeneous anisotropic and pressure-dependent media may become possible.

# PREFACE FOR THE FOLLOWING APPENDIX

In what follows, a supplementary study is presented which has been performed in the frame of the *PHASE* consortium project. An anonymous sponsor provided an industrial data set containing a total number of 231 microseismic events which have been recorded during and after a three stage hydraulic fracturing treatment of an unconventional reservoir.

For situations where hydraulic fracturing treatments considerably enhance the permeability, the hydraulic transport becomes pressure-dependent. Hence, the initial idea was to analyze the spatio-temporal characteristics of this data set according to the methodology elaborated and presented in this thesis. However, due to the low number of induced events the data statistics is not sufficient enough to apply the aforementioned analysis. Additionally, the distribution of induced events indicates that the geometry of the hydraulic fracture is closer to a classical bi-wing shape (see Figure 1.6) than to a three dimensional volumetric one (like for the Barnett Shale presented in Chapter 3). For classical bi-wing shape hydraulic fractures, their width is by far much smaller compared to their length and height. Hence, the penetration of pressure and treatment fluid into the direction normal to the fracture is typically much smaller as in parallel direction. In terms of the hydraulic transport this fracture therefore can be considered to effectively have a one dimensional geometry.

Therefore, this data set has been alternatively analyzed and interpreted in the frame of the hydraulic fracturing interpretation of the *SBRC* approach. This method aims to determine fracture geometry, fluid loss as well as scalar magnitude estimates of rock hydraulic transport properties.

Since the permeability estimates obtained for the reservoir and the fracture body are of crucial importance for the operator, publication of these informations have not been approved. Additionally, some other parts of a prepared manuscript had to be removed as well in order to obtain permission to publish these results in the frame of the annual *PHASE* Report. This, however, can be seen as an indication for the quality of obtained results. Since all three stages have been analyzed in the same manner the following

## Preface for the following Appendix

---

appendix only includes the results which were obtained for the one with the largest number of induced events. To make this appendix mutually consistent with the previous chapters figures have been modified to appear in black and white. Otherwise, the content is identical to the manuscript which has been approved and released for publication.

## **Appendix A**

# **Estimates of fracture geometry and fluid transport properties from hydraulic fracturing induced seismicity <sup>1</sup>**

---

<sup>1</sup>This article has been included in the *PHASE 7<sup>th</sup>* Annual Report: N. Hummel and S. A. Shapiro. A Hydraulic Fracturing Case Study (I): Estimates of fracture geometry and fluid transport properties from hydraulic fracturing induced seismicity.

## A.1 Introduction

We consider microseismic hydraulic fracturing data which has been provided by one of the sponsors of the *PHASE* consortium. Such hydraulic fracturing treatments are massive stimulation operations which are used to enhance the permeability of so-called unconventional reservoirs. The unconventional reservoirs play an increasing role for the worlds growing demand for energy. However, they do not produce economic volumes of oil or gas without assistance. Representatives of unconventional are for example gas shales, coal bed methane or heavy oil. In order to make such reservoirs economically productive steam injections or hydraulic fracturing treatments need to be performed (Economides and Nolte, 2000). In the latter case fluid is injected at high flow rates and pressures through a perforated domain of a wellbore. If the downhole pressure exceeds the minimum principal stress a hydraulic fracture is initiated and propagates in a direction which is determined by the local stress field. As a result of such massive stimulation treatments small magnitude earthquakes are induced. Mapping their hypocentre provides information about fracture orientation (indicating the stress orientation), fracture growth or stimulated rock volume. Recently, reflected waveforms from induced seismicity also have been considered to provide high resolution images of the reservoir in the vicinity of those microseismic events (Reshetnikov et al., 2010). In particular, fluid induced seismicity can be used to obtain information about hydraulic transport properties.

Shapiro et al. (1997, 1999, 2002) introduced the so-called SBRC (seismicity-based reservoir characterization) approach where they follow the philosophy that the occurrence of fluid injection induced microseismicity is based on a diffusional relaxation of the pore pressure perturbation which is induced by the fluid injection. Key parameters of hydraulic transport properties can be estimated with this method. However, in the case of hydraulic fracturing the SBRC approach needs to be modified because the fluid injection can strongly change the permeability of rocks. In the following we refer to the hydraulic fracture interpretation method proposed by Shapiro et al. (2006), Dinske and Shapiro (2007), Shapiro (2008) and Dinske et al. (2010) and provide a short overview of this methodology.

## A.2 Review of the methodology

### A.2.1 Hydraulic fracturing induced seismicity during the injection phase

To understand key features of hydraulic fracturing induced microseismicity a fluid-volume balance is considered. For the case of an incompressible treatment fluid the volume of the injected fluid  $V_{\text{inj}}$  must be equal to the sum of the fluid volume stored in the created hydraulic fracture  $V_{\text{frac}}$  and the volume of fluid which is lost into the surrounding formation  $V_L$ :

$$V_{\text{inj}} = V_{\text{frac}} + V_L. \quad (\text{A.1})$$

For the following analysis the hydraulic fracture is approximated by a straight planar height-fixed fracture confined in a reservoir layer. This 2-D fracture geometry model is known as the PKN (Perkins-Kern-Nordgren) model and has been introduced by Perkins and Kern (1961) and Nordgren (1972). The half-length of the (symmetric) hydraulic fracture  $L$  can be described as a function of the injection time  $t$

$$L(t) = \frac{Qt}{4hC_L\sqrt{2t} + 2hw}, \quad (\text{A.2})$$

where  $Q$  is the average injection rate,  $h$  is the average fracture height,  $w$  is the average fracture width and  $C_L$  is the fluid-loss coefficient. The first term in the denominator depends on the fluid-loss coefficient as well as on  $\sqrt{t}$ . Therefore, this term has a diffusional character and describes the fluid-loss from the fracture walls into the surrounding rock formation. The second term in the denominator describes the geometry of the vertical cross section of the fracture and thus represents the contribution of the effective fracture volume.

Key parameters for reservoir engineering and reservoir simulation can be obtained by considering equation (A.2) for two asymptotic limits. During the initial phase of the injection, the volume of the fluid-loss might be rather insignificant and all the treatment fluid is necessary to create new fracture volume. For this asymptotic the first term in the denominator can be neglected and the half-length of the fracture  $L$  becomes approximately a linear function of the injection time  $t$

$$L(t) \approx \frac{Qt}{2hw}. \quad (\text{A.3})$$

For the early phase of the injection period such a linear dependency of induced microseismic events should be observable in the well known  $r - t$  plot, where the radial distance  $r$  of events from the injection source is plotted as a function of their relative occurrence time  $t$ . The microseismic events should migrate roughly linear with time away from the injection well. Identifying the half-length of the fracture  $L(t)$  from the  $r - t$  plot and the fracture height  $h$  from the depth view projections

of seismicity, one can use the average injection rate  $Q$  to obtain the fracture width  $w$  (see Shapiro et al., 2006).

With the information about the fracture width  $w$  it becomes possible to calculate the fracture volume  $V_{\text{frac}}$  which is equal to  $2 L h w$ . According to equation (A.1) the volume of fluid which is lost into the formation can be determined by the fracture volume  $V_{\text{frac}}$  and the volume of the injected fluid  $V_{\text{inj}}$ . The latter one can be calculated from the engineering data as simple product of the injection rate  $Q$  and the corresponding pumping period  $t_{\text{inj}}$  resulting in  $V_{\text{inj}} = Q t_{\text{inj}}$ . Thus, it is possible to calculate the fluid-loss coefficient from the comparison of the injected fluid volume and the created fracture volume according to

$$C_L = \frac{Q t_{\text{inj}} - 2 L h w}{4 L h \sqrt{2 t_{\text{final}}}}. \quad (\text{A.4})$$

For the long-term injection limit the fluid-loss from the fracture into the formation becomes dominant. In this particular case the second term in the denominator of equation (A.2) can be neglected. The spatio-temporal evolution of the microseismic event cloud should now be characterized by the diffusion like signature where  $r \propto \sqrt{t}$ . In comparison to the fluid-volume balance, information about  $C_L$  can be obtained alternatively using the triggering front concept. Formerly, the triggering front was introduced by Shapiro et al. (2002) and describes an approximate outermost envelope of fluid injection induced microseismicity in the  $r - t$  domain for situations where no dominant hydraulic fracture is created. For a homogeneous isotropic fluid-saturated medium the triggering front is given by

$$r(t) = \sqrt{4 \pi D t}, \quad (\text{A.5})$$

where  $D$  is the scalar hydraulic diffusivity. Taking into account the creation of a hydraulic fracture and neglecting the fracture geometry term equation (A.2) becomes identical to equation (A.5) with an apparent hydraulic diffusivity described by

$$D_{ap} = \frac{Q^2}{128 \pi h^2 C_L^2}. \quad (\text{A.6})$$

To apply the concept of the triggering front time intervals corresponding to interruptions in the fluid injection have to be eliminated. As a result one obtains a composite injection stop corrected  $r - t$  plot where the triggering front now can be fitted as an envelope to the corresponding microseismic event cloud. As a results one determines an estimate of the apparent diffusivity which can be used together with the fracture height from the depth view projections to calculate  $C_L$  according to

$$C_L = \frac{Q}{8 h \sqrt{2 \pi D_{ap}}}. \quad (\text{A.7})$$

One can see that equation (A.7) is independent of the fracture width. Therefore, this methodology can be used to estimate the fluid-loss if the determination of the fracture width and thus the fracture volume is not possible.

The fluid-loss coefficient  $C_L$  can be used in order to determine the permeability of the reservoir  $k_{\text{res}}$ . However, independent information about the viscosity  $\eta$  and the compressibility  $c$  of the reservoir fluid, the reservoir porosity  $\phi$  and the difference between the far-field reservoir pressure (which is assumed to be hydrostatic) and injection pressure  $\Delta p$  is necessary to calculate the reservoir permeability given by

$$k_{\text{res}} = \frac{C_L^2 \pi \eta}{\phi \Delta p^2 c}. \quad (\text{A.8})$$

### A.2.2 Hydraulic fracturing induced seismicity during the post-injection phase

A hydraulic fracture is able to penetrate further into the formation even if the fluid injection is terminated. After shut-in of the injection source a zone of seismic quiescence can be identified in the  $r - t$  plot which is limited by the so-called back front. It is assumed that microseismic events can only be triggered in a domain where the pore pressure perturbation is increasing. Correspondingly, microseismic events can not be triggered anymore at distances  $r_{bf}$  where the pore pressure perturbation already has reached its maximum at the time  $t$ . This distance  $r_{bf}$  from the injection source determines the back front which is given by (Parotidis et al., 2004)

$$r_{bf} = \sqrt{2 D_{bf} t \left( \frac{t}{t_0} - 1 \right) \ln \left( \frac{t}{t - t_0} \right)}. \quad (\text{A.9})$$

Here,  $D_{bf}$  is the hydraulic diffusivity of the fracture and  $t_0$  is the shut-in time. Fitting this back front to the microseismic events in the  $r - t$  plot provides an estimate of the hydraulic diffusivity  $D_{bf}$ . As a result of the fluid injection this fracture body diffusivity should be much larger than the field scale hydraulic diffusivity. With the information about the fracture body diffusivity the fracture body permeability can be calculated according to

$$k_{\text{frac}} \approx D_{bf} c_f \eta_f \phi_{\text{frac}}. \quad (\text{A.10})$$

Note that additional information about the compressibility of the treatment fluid  $c_f$ , the viscosity of the treatment fluid  $\eta_f$  and the fracture body porosity  $\phi_{\text{frac}}$  is necessary to determine the fracture body permeability. Having evaluated both the reservoir permeability and the fracture body permeability it is possible to calculate a dimensionless quantity which is the so-called fracture conductivity (Economides and Nolte, 2000). This fracture conductivity  $C_D$  is a key parameter for hydraulic fracturing design and is given by

$$C_D = \frac{k_{\text{frac}} w}{k_{\text{res}} L}. \quad (\text{A.11})$$

### A.3 Hydraulic fracturing induced microseismic data

One of the sponsors of the *PHASE* consortium provided us with microseismic hydraulic fracturing data. The hydraulic fracturing treatment was performed in a vertical well having a horizontal distance of about 200 m to the vertical observation well. The induced seismicity was monitored using an eight three component sensor array.

In this study we consider one single injection stage of approximately 3 hours which was performed at the treatment well. The aim is to analyze the spatio-temporal dynamics of induced seismicity in order to obtain information about the fracture geometry and the hydraulic characteristics of the reservoir. For this purpose, we used the following data:

- the coordinates  $X$ ,  $Y$  and  $Z$  of the hypocentre of events
- occurrence time  $t$  of events
- engineering data: injection rate and injection pressure
- coordinates of the perforation intervals
- location of the injection well and the observation well.

The hypocentre coordinates  $X$ ,  $Y$ ,  $Z$  are used together with the coordinates of the perforation intervals to calculate the radial distance  $r$  of induced events from the bore-hole. The engineering data are used to determine the relative occurrence time  $t$  of corresponding microseismic events with the onset of the fluid injection and to calculate the volume of injected fluid.

### A.4 Data overview

In order to enhance the permeability of the target reservoir the rock was hydraulically fractured. Both engineering data and induced microseismicity from a hydraulic fracturing treatment in a vertical injection well are shown in Figure (A.1). From the engineering data one can see that flow rates of up to 80 l/s have been used during the injection period which lasted almost 3 h. A small pre-injection test is followed by three mayor injection treatments. Between these main injection cycles the flow rate always drops down to zero. Taking into account the  $r - t$  plot (Figure A.1), one can see a correlation between the injection rate and seismicity.

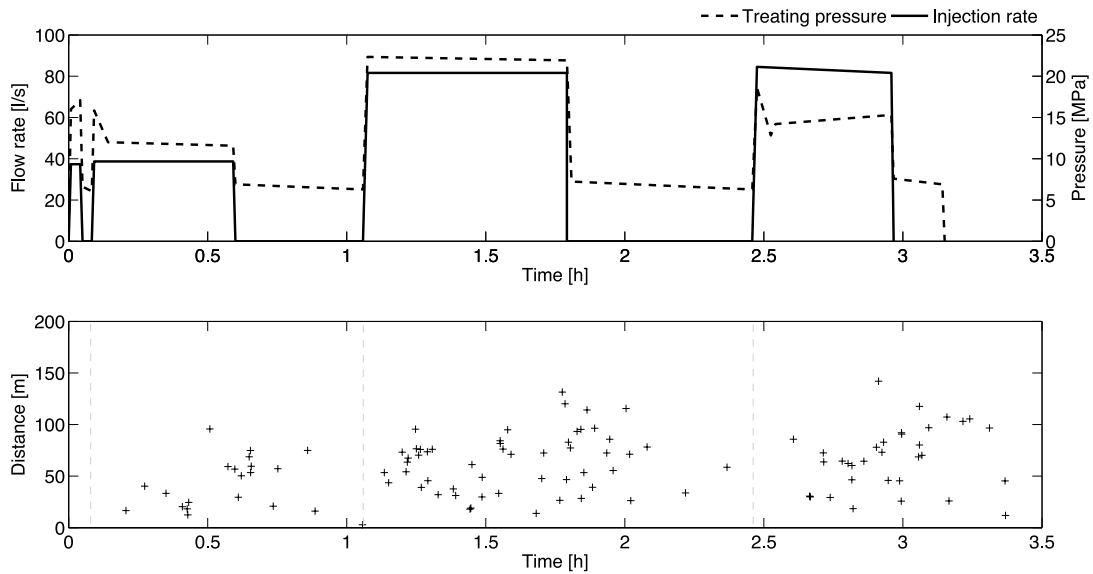


Figure A.1: Engineering data and so-called  $r - t$  plot of hydraulic fracturing induced seismicity. A clear correlation between the onset of injecting fluid into the rock and the onset of seismicity triggering can be observed.

The onset of injecting fluid into the rock is accompanied by the onset of triggering seismicity. After stop of the injection microseismic activity reduces until a new injection cycle starts. Figure A.2 shows two depth view projections and the map view projection of the cloud of induced seismicity. In strike direction the dimension of the microseismic cloud is almost 270 m. Perpendicular to the strike the dimension is approximately 150 m. From the map view projection one can also see that the microseismic event cloud features two patterns. One comprises the injection well and surrounding events which tend to the observation well. The second pattern is located more to the north-east and includes less microseismic events. From the two depth view projections one can read the vertical dimension of the microseismic event cloud, which is almost 60 m. Additionally, the vertical limitation of the cloud is quite confined to a distinct layer. The upper limit of this layer comprises the lower part of the treatment interval.

In order to better understand the spatio-temporal evolution of events we colour-code them according to their occurrence times (Figure A.3). This helps to understand processes of fluid movement and fracture penetration. From the map - and the depth view projection one can see that in the early stage the microseismic events are located westwards of the injection well. With ongoing time the induced seismicity starts to occur below the perforation intervals. Up to the end of the injection phase the microseismic events migrate upwards to shallower depths.

# A Estimates of fracture geometry and fluid transport properties from hydraulic fracturing induced seismicity

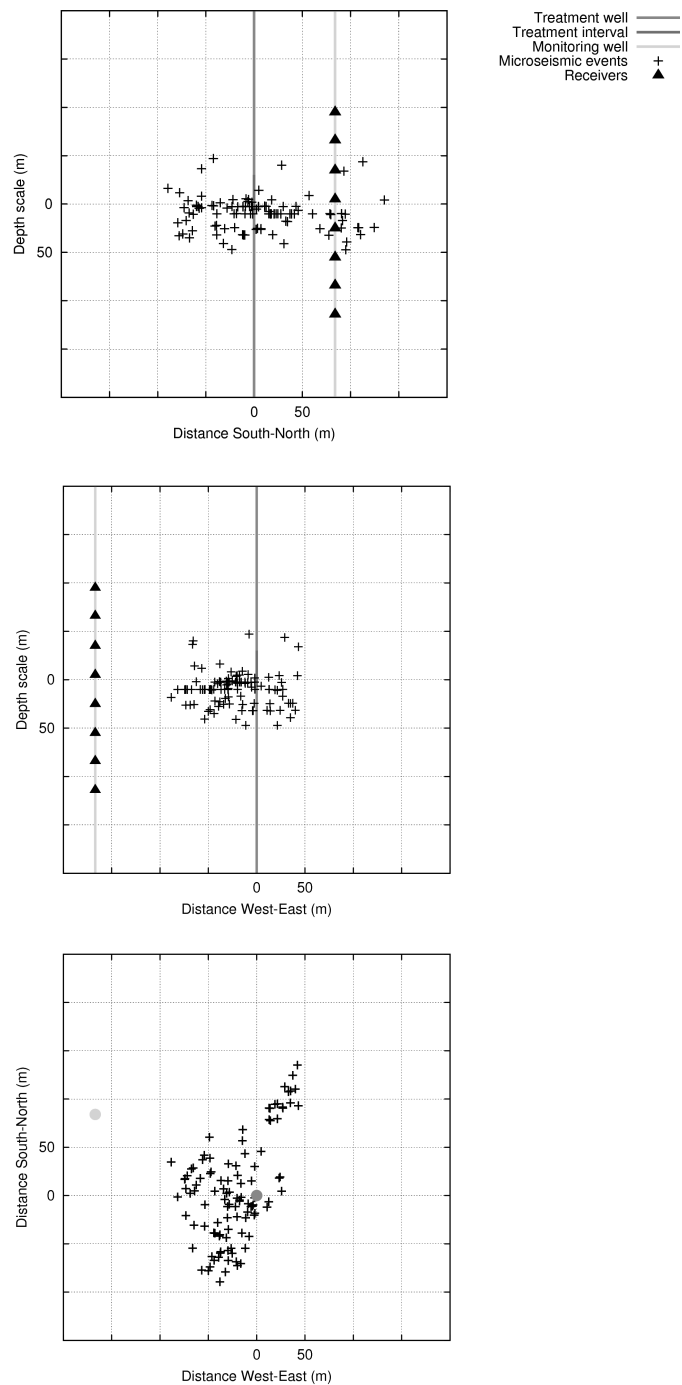


Figure A.2: Overview of 107 hydraulic fracturing induced microseismic events in two depth view projections and a map view projection including injection well and monitoring well. From the depth view projections one can see that the layer which contains most of the seismicity starts at the bottom of the treatment interval.

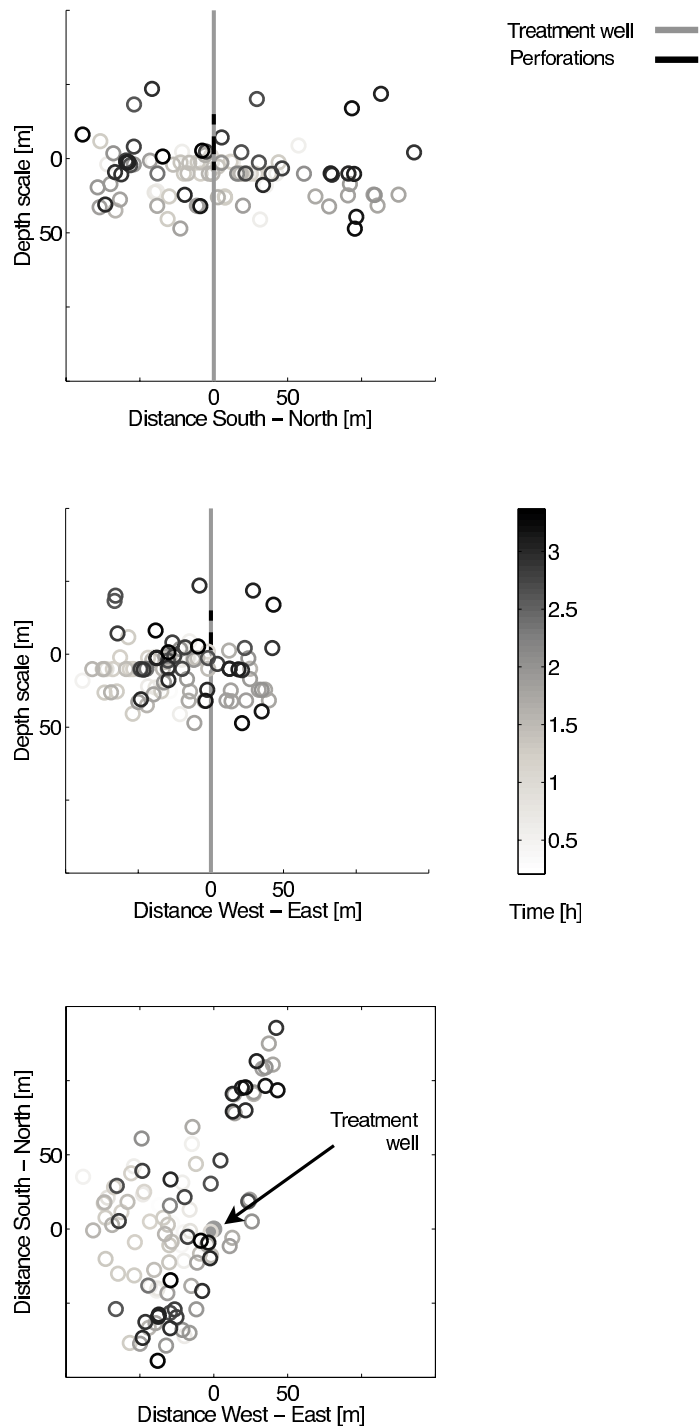


Figure A.3: Temporal evolution of hydraulic fracturing induced microseismic events being colour-coded according to their occurrence times. With ongoing injection the events migrate upwards to shallower depth.

## A.5 Results

### A.5.1 Estimation of fracture geometry

The fracture geometry is an important quantity for reservoir simulation and is a key parameter to provide information about the fracture volume. From the two depth view projections the average height of the hydraulic fracture is about 60 m (Figure A.2). However, in order to estimate the fracture volume (which can significantly differ from the stimulated volume) knowledge of the fracture length and fracture width is mandatory. Rewriting equation (A.3) yields

$$w \approx \frac{Qt}{2hL(t)}, \quad (\text{A.12})$$

which shows that the fracture width  $w$  can be obtained from the injected volume and the cross sectional area of the fracture. As the injected volume can be obtained from the engineering data and the fracture height from the depth view projection, the still unknown parameter is the fracture half length  $L$ . This missing information about  $L$  is obtained from the  $r - t$  plot. For the initial phase of the injection period, where the volume of the fluid-loss is rather insignificant, the half-length of the fracture  $L$  can be approximately described by a function which is linear with the injection time

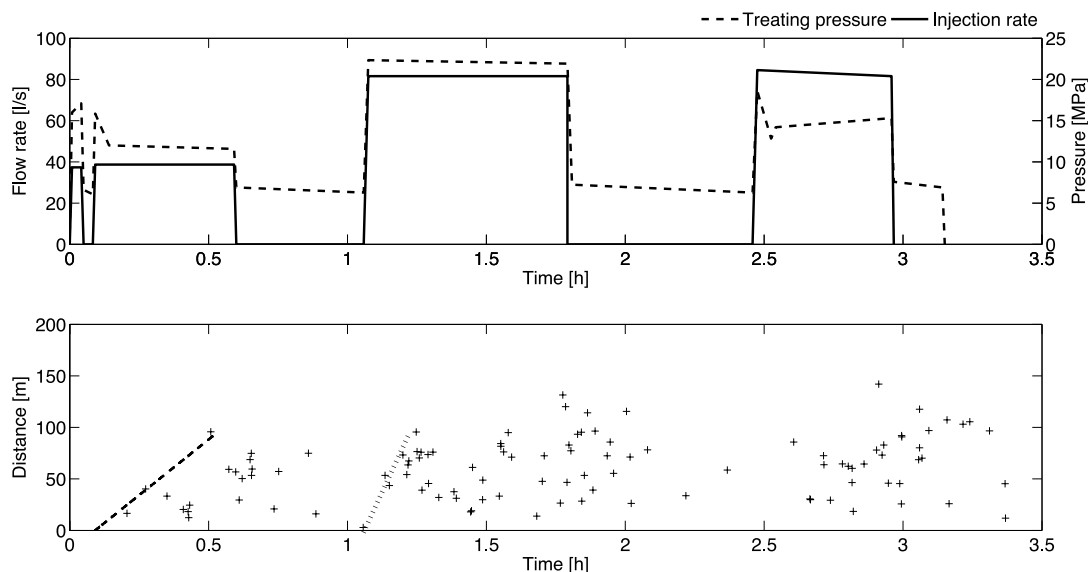


Figure A.4: Engineering data and  $r - t$  plot used for estimating the fracture width. Hereby the half length of the fracture is estimated from the quasi linear growth of the microseismic cloud with ongoing injection time (dashed line). With the onset of the third injection period another quasi linear growth can be observed which can be fitted with the black dotted line. The slope of this line is steeper compared to the first one which is interpreted as a reopening of the formerly created hydraulic fracture.

$t$  (equation A.3). We interpret such a linear with time event migration away from the treatment well as the opening of the hydraulic fracture (Figure A.4). During the first 26 minutes of fracturing a quasi linear growth of the microseismic cloud up to a distance of about 90 m can be observed. Using an average injection rate  $Q$  of about  $0.038 \text{ m}^3/\text{s}$  and a fracture height  $h$  of about 60 m the average fracture width results in

$$w \approx 5.5 \text{ mm} .$$

With the above mentioned values the average velocity of fracture opening and propagation is approximately  $V_{\text{frac}} \sim 0.06 \text{ m/s}$ .

We note here, that even for the third injection cycle starting shortly after a relative injection time of 1 h a second quasi linear growth of the microseismic cloud can be identified. The slope of the fitted trend line is steeper compared to the slope of the first line which indicates a faster fracture propagation process. In our understanding this can be interpreted as reopening and further propagation of the formerly created hydraulic fracture with the corresponding injection phase.

### A.5.2 Estimation of fluid-loss coefficient

For hydraulic fracture design as well as for reservoir and geomechanical modelling minifrac tests provide critical input data. To specify formation leak-off characteristics the fluid-loss coefficient is a necessary and important parameter. According to equation (A.4) the fluid-loss coefficient  $C_L$  can be obtained from a simple fluid volume balance using the injected volume  $V_{\text{inj}}$ , the fracture volume  $V_{\text{frac}}$  and the volume of the fluid which is lost into the formation. The volume of injected fluid can be obtained from the engineering data (Figure A.1). For each injection phase the average injection rate  $Q$  is multiplied with its corresponding duration. For the whole injection treatment the volume of injected fluid is  $446 \text{ m}^3$ . The volume of the created hydraulic fracture is obtained using a final fracture half length of 150 m (from the  $r - t$  plot), a fracture height of about 60 m and the calculated fracture width of 5.5 mm. The fracture volume of  $V_{\text{frac}} = 99 \text{ m}^3$  is the result of injecting  $446 \text{ m}^3$  of fluid. Following the fluid-volume balance this means that 78 % of the injected volume was lost into the rock.

According to equation (A.4) the fluid-loss coefficient can be estimated to

$$C_L \approx 8.5 \cdot 10^{-5} \frac{\text{m}}{\sqrt{\text{s}}} .$$

Another possibility to estimate the fluid-loss coefficient is based on the triggering front (equation A.5). For this purpose the time periods of injection stops have been removed. The fluid-loss coefficient is obtained by fitting equation (A.5) as envelope to the microseismic event cloud in the composite  $r - t$  plot (Figure A.5). Using equation (A.7) with the obtained estimate of the apparent diffusivity  $D_{ap}$ , the fracture height

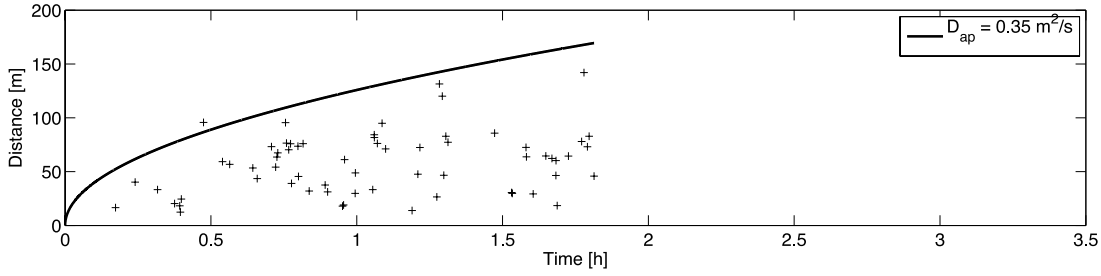


Figure A.5: Composite  $r - t$  plot which is obtained after removing time periods of injection stops. The triggering front provides an apparent hydraulic diffusivity estimate which is used to calculate to fluid-loss coefficient.

of 60 m (from depth view projections) and the average flow rate  $Q = 0.06 \text{ m}^3/\text{s}$ , the fluid-loss coefficient is

$$C_L \approx 8.4 \cdot 10^{-5} \frac{\text{m}}{\sqrt{\text{s}}}.$$

The two estimates of fluid-loss coefficients are in the same order of magnitude and show quite good agreement.

### A.5.3 Estimation of reservoir permeability

With the information about the fluid-loss coefficient it is also possible to estimate the reservoir permeability if additional information about the reservoir fluid, the reservoir porosity and the difference between the far-field reservoir pressure and injection pressure is available (see equation A.8). For the calculation of the reservoir permeability near fracture surface effects on the pressure difference between the fracture and the far field reservoir, like for example filter cakes, are neglected.

### A.5.4 Estimation of fracture body diffusivity

Besides the information of the reservoir permeability the hydraulic fracturing interpretation of the SBRC approach also provides an estimate for the fracture body permeability. The post-injection phase is considered and the spatio-temporal distribution of the microseismic events is analyzed after the shut-in of the injection source at the time  $t_0$ . Figure (A.6) shows the corresponding engineering data and the  $r - t$  plot. After the shut-in time  $t_0$  a domain of seismic quiescence can be identified which is limited by the back front. For this particular case three different back fronts with three different hydraulic diffusivities are shown. The dark grey curve fits the zone of seismic quiescence the best and has a hydraulic diffusivity of  $D_{bf} = 1.5 \text{ m}^2/\text{s}$ . According to equation (A.10) one can estimate the fracture body permeability if information about the compressibility  $c_f$  and viscosity of the treatment fluid  $\eta_f$  as well as the fracture body porosity are available.

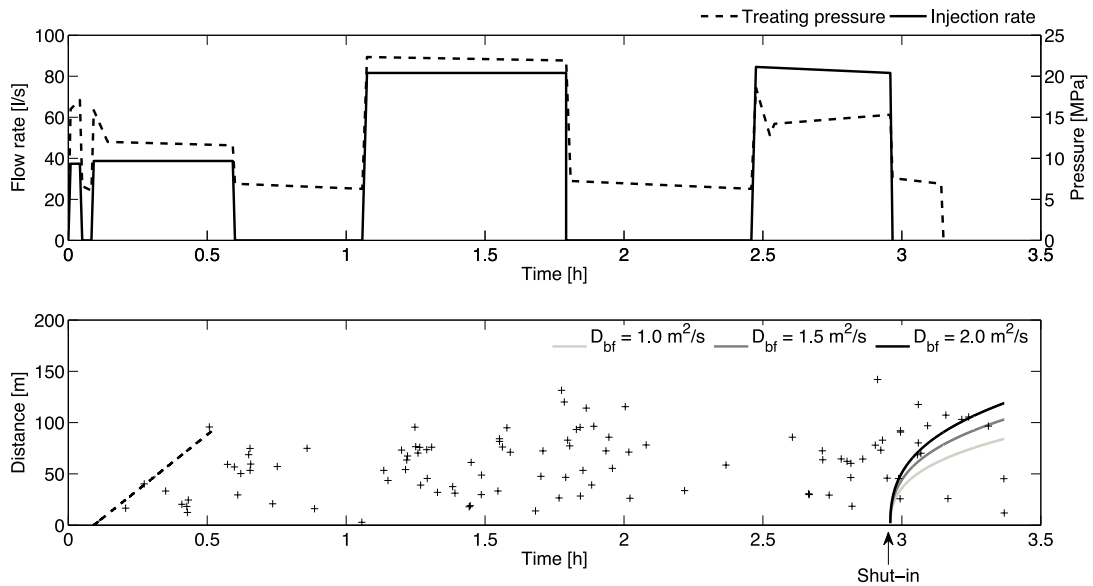


Figure A.6: Engineering data and  $r - t$  plot showing three different fitted back fronts. The dark grey back front characterized by a hydraulic diffusivity of  $1.5 \text{ m}^2/\text{s}$  fits the data best. It can be used to estimate the fracture body permeability if additional information about the treatment fluid and the reservoir is available.

## A.6 Discussion and conclusion

In this study we considered hydraulic fracturing induced microseismic data given by a sponsor of the *PHASE* consortium. We analyzed and interpreted the spatio-temporal dynamics of microseismicity. As a result we determined key parameters for hydraulic fracture design and reservoir simulation which are summarized in Table (A.1). One can see that the fluid-loss coefficients are in excellent agreement although they have been determined using both a fluid-volume balance and a heuristic approach based on the triggering front. We want to point out here, that the one dimensional hydraulic fracture interpretation method provides reasonable results which are comparable with results from Cotton Valley (Shapiro et al., 2006; Dinske and Shapiro, 2007; Dinske et al., 2010).

	Quantity	data set
	# events	107
Fracture geometry	Half-length [m]	150
	Height [m]	60
	Width [mm]	5.5
	Fracture volume [m <sup>3</sup> ]	99
	Injected volume [m <sup>3</sup> ]	446
Reservoir properties	Relative fluid-loss [%]	78
	Fluid-loss coef (FVB) [ $\frac{m}{\sqrt{s}}$ ]	$8.5 \cdot 10^{-5}$
	Fluid-loss coef (fitting) [ $\frac{m}{\sqrt{s}}$ ]	$8.4 \cdot 10^{-5}$
	Backfront diffusivity [m <sup>2</sup> /s]	1.5
Further deliverables	Reservoir permeability	Needs information about viscosity $\eta$ , compressibility $c$ , reservoir porosity $\phi$ and the pressure difference $\Delta p$
	Fracture body permeability	
	Fracture conductivity	

Table A.1: Overview of reservoir parameters obtained from the analysis of spatio-temporal dynamics of hydraulic fracturing induced seismicity.

# References

- Adler, P. M. and Thovert, J.-F. (1999). *Fractures and Fracture Networks*. Kluwer Academic Publishers.
- Ake, J., Mahrer, K., O'Connell, D., and Block, L. (2005). Deep-Injection and Closely Monitored Induced Seismicity at Paradox Valley, Colorado. *Bulletin of the Seismological Society of America*, 95(2):664–683.
- Audigane, P., Royer, J.-J., and Kaieda, H. (2002). Permeability characterization of the Sultz and Ogachi large-scale reservoir using induced microseismicity. *Geophysics*, 67(1):204–211.
- Aylmore, L. A. G. and Quirk, J. P. (1960). Domain or Turbostratic Structure of Clays. *Nature*, 187:1046–1048.
- Baisch, S., Weidler, R., Vörös, R., Wyborn, D., and de Graaf, L. (2006). Induced Seismicity during the Stimulation of a Geothermal HFR Reservoir in the Cooper Basin, Australia. *Bulletin of the Seismological Society of America*, 96(6):2242–2256.
- Baker, T., Granat, R., and Clayton, R. W. (2005). Real-time Earthquake Location Using Kirchhoff Reconstruction. *Bulletin of the Seismological Society of America*, 95(2):699–707.
- Barbier, E. (2002). Geothermal energy technology and current status: an overview. *Renewable and Sustainable Energy Reviews*, 6(1–2):3 – 65.
- Barenblatt, G. (1996). *Scaling, Self-Similarity and Intermediate Asymptotics*. Cambridge University Press, New York, NY.
- Baria, R., Baumgärtner, J., Rummel, F., Pine, R. J., and Sato, Y. (1999). HDR/HWR reservoirs: concepts, understanding and creation. *Geothermics*, 28(4–5):533 – 552.
- Barree, R. D. and Mukherjee, H. (1996). Determination of Pressure Dependent Leakoff and Its Effect on Fracture Geometry. *Proceedings, Society of Petroleum Engineers Annual Technical Conference, Paper 36424*.

## References

---

- Barton, C., A., Zoback, M. D., and Moos, D. (1995). Fluid flow along potentially active faults in crystalline rock. *Geology*, 23(8):683–686.
- Bear, J., de Marsily, G., and Tsang, C.-F. (1993). *Flow and Contaminant Transport in Fractured Rock*. Academic Press, San Diego, California.
- Berkowitz, B. (2002). Characterizing flow and transport in fractured geological media: A review. *Advances in Water Resources*, 25:861–884.
- Bernabe, Y. (1986). The effective pressure law for permeability in Chelmsford granite and Barre granite. *International Journal of Rock Mechanics and Mining Sciences & Geomechanics Abstracts*, 23(3):267–275.
- Bernabe, Y. (1987). The effective pressure law for permeability during pore pressure and confining pressure cycling of several crystalline rocks. *Journal of Geophysical Research*, 92(B1):649–657.
- Bernabe, Y. (1988). Comparison of the Effective Pressure Law for Permeability and Resistivity Formation Factor in Chelmsford Granite. *Pure and Applied Geophysics*, 127(4).
- Best, M. E. and Katsube, T. J. (1995). Shale permeability and its significance in hydrocarbon exploration. *The Leading Edge*, 14(3):165–170.
- Biot, M. A. (1962). Mechanics of Deformation and Acoustic Propagation in Porous Media. *Journal of Applied Physics*, 33(4):1482–1498.
- Birkelo, B., Cieslik, K., Witten, B., Montgomery, S., Artman, B., Miller, D., and Norton, M. (2012). High-quality surface microseismic data illuminates fracture treatments: A case study in the Montney. *The Leading Edge*, 31(11):1318–1325.
- Bohnhoff, M. and Zoback, M. D. (2010). Oscillation of fluid-filled cracks triggered by degassing of CO<sub>2</sub> due to leakage along wellbores. *Journal of Geophysical Research*, 115(B11305).
- Bohnhoff, M., Zoback, M. D., Chiaramonte, L., Gerst, J. L., and Gupta, N. (2010). Seismic detection of CO<sub>2</sub> leakage along monitoring wellbores. *International Journal of Greenhouse Gas Control*, 4(4):687–697.
- Brace, W. F. (1980). Permeability of crystalline and argillaceous rocks. *International Journal of Rock Mechanics and Mining Sciences & Geomechanics Abstracts*, 17(5):241 – 251.
- Brace, W. F., Walsh, J. B., and Frangos, W. (1968). Permeability of granite under high pressure. *Journal of Geophysical Research*, 73(6):2225–2236.

- Britt, L. K., Hager, C. J., and Thompson, J. W. (1994). Hydraulic Fracturing in a Naturally Fractured Reservoir. *Proceedings, Society of Petroleum Engineers Annual Technical Conference, Paper 28717*.
- Brock, W. R. and Bryan, L. A. (1989). Summary Results of CO<sub>2</sub> EOR Field Tests, 1972-1987. *Proceedings, Society of Petroleum Engineers Low Permeability Reservoir Symposium, Paper 18977*.
- Brown, D., DuTeaux, R., Kruger, P., Swenson, D., and Yamaguchi, T. (1999). Fluid circulation and heat extraction from engineered geothermal reservoirs. *Geothermics*, 28:553–572.
- Brown, S. R. (1987). Fluid flow through rock joints: The effect of surface roughness. *Journal of Geophysical Research*, 92(B2):1337–1347.
- Bruel, D. (2007). Using the migration of induced seismicity as a constraint for fractured hot dry rock reservoir modelling. *International Journal of Rock Mechanics & Mining Sciences*, 44:1107–1117.
- Byerlee, J. D. (1978). Friction of rocks. *Pure and Applied Geophysics*, 116:615–626.
- Carnes Jr., P. S. (1966). Effects of Natural Fractures on Directional Permeability in Water Flooding. *Proceedings, Society of Petroleum Engineers Secondary Recovery Symposium, Paper 1423*.
- Clark, J. B. (1949). A hydraulic process for increasing the productivity of oil wells. *AIME Trans.*, 186:1–8.
- Clavaud, J.-B., Mainault, A., Zamora, M., Rasolofosaon, P., and Schlitter, C. (2008). Permeability anisotropy and its relation with porous medium structure. *Journal of Geophysical Research*, 113(B01202).
- Cornet, F. H., Bérard, T., and Bourouis, S. (2007). How close to failure is a granite rock mass at a 5 km depth? *International Journal of Rock Mechanics and Mining Sciences*, 44(1):47–66.
- Cuenot, N., Dorbath, C., and Dorbath, L. (2008). Analysis of the Microseismicity Induced by Fluid Injections at the EGS Site of Soultz-sous-Forêts (Alsace, France): Implications for the Characterization of the Geothermal Reservoir Properties. *Pure and Applied Geophysics*, 165:797–828.
- Dahm, T., Krüger, F., Stammer, K., Klinge, K., Kind, R., and Wylegalla, K. G. J.-R. (2007). The 2004 M<sub>W</sub> Rotenburg, Northern Germany, Earthquake and Its Possible Relationship with Gas Recovery. *Bulletin of the Seismological Society of America*, 97(3):691–704.

## References

---

- Daley, T. M., Schoenberg, M. A., Rutqvist, J., and Nihei, K. T. (2006). Fractured reservoirs: An analysis of coupled elastodynamic and permeability changes from pore-pressure variation. *Geophysics*, 71(5):O33.
- David, C., Wong, T.-F., Zhu, W., and Zhang, J. (1994). Laboratory Measurement of Compaction-induced Permeability Change in Porous Rocks: Implications for the Generation and Maintenance of Pore Pressure Excess in the Crust. *Pure and Applied Geophysics*, 143(1):425–456.
- Davis, S. D. and Pennington, W. D. (1989). Induced seismic deformation in the Cogdell oil field of West Texas. *Bulletin of the Seismological Society of America*, 79(5):1477–1495.
- de Marsily, G. (1986). *Quantitative Hydrogeology*. Academic Press, San Diego, California.
- Dinske, C., Langenbruch, C., Galindo Guerreros, J., and Shapiro, S. A. (2013). Influence of Hydraulic Heterogeneity of Rocks on Pore Pressure Changes induced by Reservoir Stimulations. *Proceedings, European Association of Geoscientists & Engineers Annual Conference, Paper Th1407*.
- Dinske, C. and Shapiro, S. A. (2007). Microseismic signatures of hydraulic fracturing in tight gas sandstones with gel and water based treatment fluids. *3<sup>rd</sup> Annual PHASE Report*, pages 21–38.
- Dinske, C., Shapiro, S. A., and Ladner, F. (2009). Seismicity Based Reservoir Characterization of Basel Geothermal Site. *Proceedings, European Association of Geoscientists & Engineers Annual Conference, Paper P033*.
- Dinske, C., Shapiro, S. A., and Rutledge, J. T. (2010). Interpretation of Microseismicity Resulting from Gel and Water Fracturing of Tight Gas Reservoirs. *Pure and Applied Geophysics*, 167:169–182.
- Dong, J.-J., Hsu, J.-Y., Wu, W.-J., Shimamoto, T., Hung, J.-H., Yeh, E.-C., Wu, Y.-H., and Sone, H. (2010). Stress-dependence of the permeability and porosity of sandstone and shale from TCDP Hole-A. *International Journal of Rock Mechanics & Mining Sciences*, 47(7):1141–1157.
- Dreesen, D. S. and Nicholson, R. W. (1985). Well completion and operations for MHF of Fenton Hill HDR Well EE-2. *Trans. Geotherm. Res. Coun.*, 9(II):89 – 94.
- Dullien, F. A. L. (1992). *Porous Media: Fluid Transport and Pore Structure*. Academic Press, San Diego, California, 2<sup>nd</sup> edition.
- Durucan, S. and Edwards, J. (1986). The effects of stress and fracturing on permeability of coal. *Mining Science and Technology*, 3(3):205 – 216.

- Dyer, B., Juppe, A., and Jones, R. H. (1994). Microseismic results from the European HDR Geothermal Project at Soultz-sous-Forets, Alsace, France. *CSM Associated Ltd.*, IR03/24.
- Eberhart-Phillips, D. and Oppenheimer, D. H. (1984). Induced seismicity in The Geysers Geothermal Area, California. *Journal of Geophysical Research*, 89(B2):1191–1207.
- Economides, M. J. and Nolte, K. G. (2000). *Reservoir Stimulation*. John Wiley & Sons, Inc, New York.
- Elders, W., Bird, D., Williams, A., and Schiffman, P. (1984). Hydrothermal flow regime and magmatic heat source of the Cerro Prieto geothermal system, Baja California, Mexico. *Geothermics*, 13(1–2):27 – 47.
- Ely, J. W. (1985). *Stimulation Treatment Handbook: An Engineer's Guide to Quality Control*. Pennwell Publishing Company.
- Evans, J. P., Forster, C. B., and Goddard, J. V. (1997). Permeability of fault-related rocks, and implications for hydraulic structure of fault zones. *Journal of Structural Geology*, 19(11):1393–1404.
- Evans, K. F., Zappone, A., Kraft, T., Deichmann, N., and Moia, F. (2012). A survey of the induced seismic responses to fluid injection in geothermal and CO<sub>2</sub> reservoirs in Europe. *Geothermics*, 41(0):30 – 54.
- Farouq Ali, S. M. (1974). Current status of steam injection as a heavy oil recovery method. *Journal of Canadian Petroleum Technology*, 13(1).
- Farouq Ali, S. M. and Abad, B. (1976). Bitumen recovery from oil sands, using solvents in conjunction with steam. *Journal of Canadian Petroleum Technology*, 15(3).
- Fehler, M., House, L., Phillips, W. S., and Potter, R. (1998). A method to allow temporal variation of velocity in travel-time tomography using microearthquakes induced during hydraulic fracturing. *Tectonophysics*, 289:189–201.
- Fehler, M. C. (1989). Stress Control of Seismicity Patterns Observed During Hydraulic Fracturing Experiments at the Fenton Hill Hot Dry Rock Geothermal Energy Site, New Mexico. *International Journal of Rock Mechanics and Mining Sciences & Geomechanics Abstracts*, 26(34):211 – 219.
- Fischer, T., Hainzl, S., Eisner, L., Shapiro, S. A., and Le Calvez, J. (2008). Microseismic signatures of hydraulic fracture growth in sediment formations: Observations and modeling. *Journal of Geophysical Research*, 113(B02307).

## References

---

- Fisher, M. K., Heinze, J. R., Harris, C. D., Davidson, B. M., Wright, C. A., and Dunn, K. P. (2004). Optimizing Horizontal Completion Techniques in the Barnett Shale Using Microseismic Fracture Mapping. *Proceedings, Society of Petroleum Engineers Annual Technical Conference, Paper 90051*.
- Fisher, M. K., Wright, C. A., Davidson, B. M., Goodwin, A. K., Fielder, E. O., Buckler, W. S., and Steinsberger, N. P. (2002). Integrating Fracture Mapping Technologies to Optimize Stimulations in the Barnett Shale. *Proceedings, Society of Petroleum Engineers Annual Technical Conference, Paper 77441*.
- Freeze, R. and Cherry, J. (1979). *Groundwater*. Rentice-Hall Inc. Englewood Cliffs, NJ.
- Gale, J. F. W., Reed, R. M., and Holder, J. (2007). Natural fractures in the Barnett Shale and their importance for hydraulic fracture treatments. *AAPG Bulletin*, 91(4):603–622.
- Gangi, A. F. (1978). Variation of whole and fractured Porous Rock Permeability with Confining pressure. *International Journal of Rock Mechanics and Mining Sciences & Geomechanics Abstracts*, 15(5):249–257.
- Ghabezloo, S., Sulem, J., S., G., and Martineau, F. (2009). Effective stress law for the permeability of a limestone. *International Journal of Rock Mechanics and Mining Sciences*, 46(2):297 – 306.
- Gibbins, J. and Chalmers, H. (2008). Carbon capture and storage. *Energy Policy*, 36(12):4317–4322.
- Gibbs, J. F., Healy, J. H., Raleigh, C. B., and Coakley, J. (1973). Seismicity in the Rangely, Colorado, area: 1962-1970. *Bulletin of the Seismological Society of America*, 63(5):1557–1570.
- Gilfillan, S. M. V., Lollar, B. S., Holland, G., Blagburn, D., Stevens, S., Schoell, M., Cassidy, M., Ding, Z., Zhou, Z., Lacrampe-Couloume, G., and Ballentine, C. J. (2009). Solubility trapping in formation water as dominant CO<sub>2</sub> sink in natural gas fields. *Nature*, 458(7238):614–618.
- Goertz-Allmann, B. P. and Wiemer, S. (2013). Geomechanical modeling of induced seismicity source parameters and implications for seismic hazard assessment. *Geophysics*, 78(1):KS25–KS39.
- Grechka, V., Mazumdar, P., and Shapiro, S. A. (2010). Predicting permeability and gas production of hydraulically fractured tight sands from microseismic data. *Geophysics*, 75(1):B1–B10.
- Gudmundsson, J. S. and Lund, J. W. (1985). Direct uses of earth heat. *International Journal of Energy Research*, 9(3):345–375.

- Guéguen, Y., Gavrilenko, P., and Le Ravalec, M. (1996). Scales of rock permeability. *Surveys in Geophysics*, 17(3):245–263.
- Guéguen, Y. and Palciauskas, V. (1994). *Introduction to the Physics of Rocks*. Princeton University Press, Princeton.
- Häring, M. O., Schanz, U., Ladner, F., and Dyer, B. C. (2008). Characterisation of the Basel 1 enhanced geothermal system. *Geothermics*, 37:469 – 495.
- Haszeldine, R. S. (2009). Carbon Capture and Storage: How Green Can Black Be? *Science*, 325(5948):1647–1652.
- Hawsey, J. D. and Jacocks, C. L. (1961). The use of fluid-loss additives in hydraulic fracturing of oil and gas wells. *Proceedings, Society of Petroleum Engineers California Regional Meeting, 2-3 November, Bakersfield*.
- Healy, J. H., Hamilton, R. M., and Raleigh, C. B. (1970). Earthquakes induced by fluid injection and explosion. *Tectonophysics*, 9:205–214.
- Healy, J. H., Rubey, W. W., Griggs, D. T., and Raleigh, C. B. (1968). The Denver Earthquakes. *Science*, 161(3848):1301–1310.
- Holditch, S. A. (2003). The increasing role of unconventional reservoirs in the future of the oil and gas business. *Journal of Petroleum Technology*, 55(11):34–37.
- Holditch, S. A. (2009). Stimulation of Tight Gas Reservoirs Worldwide. *Proceedings, Offshore Technology Conference, OTC 20267–PP*.
- Holt, T., Jensen, J.-I., and Lindeberg, E. (1995). Underground storage of CO<sub>2</sub> in aquifers and oil reservoirs. *Energy Conversion and Management*, 36(6–9):535 – 538. Proceedings of the Second International Conference on Carbon Dioxide Removal.
- Hornby, B. E., Schwartz, L. M., and Hudson, J. A. (1994). Anisotropic effective-medium modeling of the elastic properties of shales. *Geophysics*, 59(10):1570–1583.
- House, L. (1987). Locating microearthquakes induced by hydraulic fracturing in crystalline rock. *Geophysical Research Letters*, 14(9):919 – 921.
- Howard, J. and Fast, C. R. (1957). Optimum fluid characteristic for fracture extension. *Drilling Production and Practice, American Petroleum Institute*, pages 261–270.
- Hubbert, M. K. and Willis, D. G. (1957). Mechanics of hydraulic fracturing. *AIME Petroleum Trans.*, 210:153–166.

## References

---

- Hummel, N. and Müller, T. M. (2008a). Microseismic Signatures of Nonlinear Pore Pressure Diffusion. *70<sup>th</sup> EAGE Conference & Exhibition, Extended Abstracts*, P022.
- Hummel, N. and Müller, T. M. (2008b). Microseismic signatures of nonlinear pore pressure diffusion. In *SEG Technical Program Expanded Abstracts 2008*, pages 1382–1386. Society of Exploration Geophysicists.
- Hummel, N. and Müller, T. M. (2009). Microseismic signatures of non-linear pore-fluid pressure diffusion. *Geophysical Journal International*, 179(3):1558–1565.
- Hummel, N. and Shapiro, S. A. (2012). Microseismic estimates of hydraulic diffusivity in case of non-linear fluid-rock interaction. *Geophysical Journal International*, 188(3):1441–1453.
- Hummel, N. and Shapiro, S. A. (2013). Nonlinear diffusion-based interpretation of induced microseismicity: A Barnett Shale hydraulic fracturing case study. *Geophysics*, 78(5):B211–B226.
- Ito, H. (2003). Inferred role of natural fractures, veins, and breccias in development of the artificial geothermal reservoir at the Ogachi Hot Dry Rock site, Japan. *Journal of Geophysical Research: Solid Earth*, 108(B9):n/a–n/a.
- Jaeger, J. C., Cook, N. G. W., and Zimmerman, R. (2007). *Fundamentals of Rock Mechanics*. Wiley-Blackwell, 4<sup>th</sup> edition.
- Jaupart, C. and Mareschal, J. (2010). *Heat Generation and Transport in the Earth*. Cambridge University Press.
- Jones, L. E. A. and Wang, H. F. (1981). Ultrasonic velocities in Cretaceous shales from the Williston basin. *Geophysics*, 46(3):288–297.
- Kaieda, H., Sasaki, S., and Wyborn, D. (2010). Comparison of Characteristics of Micro-Earthquakes Observed During Hydraulic Stimulation Operations in Ogachi, Hijiori and Cooper Basin HDR Projects. *Proceedings of World Geothermal Congress, Bali, Indonesia, 25–29 April, 2010*.
- Kranz, R. L., Frankel, A. D., Engelder, T., and Scholz, C. H. (1979). The permeability of whole and jointed barre granite. *International Journal of Rock Mechanics and Mining Sciences & Geomechanics Abstracts*, 16(4):225–234.
- Kwon, O., Kronenberg, A. K., Gangi, A. F., Johanson, B., and Herbert, B. E. (2004). Permeability of illite-bearing shale: 1. Anisotropy and effects of clay content and loading. *Journal of Geophysical Research*, 109(B10205).

- Lahaie, F., Boyer, E., Grasso, J. R., and Fourmaintraux, D. (1998). Production as a Tool to Control the Efficiency of Reservoir Fracturing: The Lacq Case-Study. *Proceedings, SPE/ISRM Rock Mechanics in Petroleum Engineering, Paper 47318*.
- Langenbruch, C. and Shapiro, S. A. (2010). Decay rate of fluid-induced seismicity after termination of reservoir stimulations. *Geophysics*, 75(6):MA53–MA62.
- Langenbruch, C. and Shapiro, S. A. (2012). Modelling of Fracture Strength Distribution in Elastically Heterogeneous Rocks. *Proceedings, European Association of Geoscientists & Engineers Annual Conference, Paper C043*.
- Larsen, G. and Chilingarian, V. (1983). *Developments in sedimentology: Diagenese in sediments and sedimentary rocks*, 2. Elsevier Science.
- Lay, T. and Wallace, T. C. (1995). *Modern Global Seismology*. International Geophysics. Academic Press.
- Lee, C.-H. and Farmer, I. W. (1993). *Fluid Flow in Discontinuous Rocks*. Chapman & Hall.
- Lescanne, M., Hy-Billiot, J., Aimard, N., and Prinnet, C. (2011). The site monitoring of the Lacq industrial CCS reference project. *Energy Procedia*, 4:3518 – 3525. 10th International Conference on Greenhouse Gas Control Technologies.
- Li, M., Bernabé, Y., Xiao, W. I., Chen, Z.-Y., and Liu, Z.-Q. (2009). Effective pressure law for permeability of E-bei sandstones. *Journal of Geophysical Research*, B07205.
- Liu, H.-H. and Rutqvist, J. (2010). A New Coal-Permeability Model: Internal Swelling Stress and Fracture–Matrix Interaction. *Transport in Porous Media*, 82(1):157–171.
- Lonardelli, I., Wenk, H.-R., and Ren, Y. (2007). Preferred orientation and elastic anisotropy in shales. *Geophysics*, 72(2):D33–D40.
- Lund, J. W. (2007). Characteristics, development and utilization of geothermal resources. *Bulletin Geo-Heat Center*, 28(2):1–9.
- Macaulay, R. C., Krafft, J. M., Hartemink, M., and Escovedo, B. (1995). Design of a steam pilot in a fractured carbonate reservoir - qarn alam field, oman. *Proceedings, Society of Petroleum Engineers International Heavy Oil Symposium, Paper 30300*.
- Mader, D. (1989). *Hydraulic Proppant Fracturing and Gravel Packing*. Developments in Petroleum Science. Elsevier Science.
- Majer, E. L., Baria, R., Stark, M., Oates, S., Bommer, J., Smith, B., and Asanuma, H. (2007). Induced seismicity associated with Enhanced Geothermal Systems. *Geothermics*, 36:185–222.

## References

---

- Mathieson, A., Midgley, J., Dodds, K., and Wright, I. (2010). CO<sub>2</sub> sequestration monitoring and verification technologies applied at Krechba, Algeria. *The Leading Edge*, 29(2):216–222.
- Maxwell, S. C. and Urbancic, T. I. (2001). The role of passive microseismic monitoring in the instrumented oil field. *The Leading Edge*, 20(6):635–639.
- Maxwell, S. C., Waltmann, C. K., Warpinski, N. R., Mayerhofer, M. J., and Boroumand, N. (2009). Imaging Seismic Deformation Induced by Hydraulic Fracture Complexity. *SPE Res Eval & Eng*, 12(1):48–52.
- Mayerhofer, M. J., Bolander, J. L., Williams, L. I., Pavy, A., and Wohlhart, S. L. (2005). Integration of Microseismic-Fracture-Mapping Fracture and Production Analysis With Well-Interference Data To Optimize Fracture Treatments in the Overton Field, East Texas. *Proceedings, Society of Petroleum Engineers Annual Technical Conference, Paper 95508*.
- Mayerhofer, M. J., Lolon, E. P., Youngblood, J. E., and Heinze, J. R. (2006). Integration of Microseismic-Fracture-Mapping Results With Numerical Fracture Network Production Modeling in the Barnett Shale. *Proceedings, Society of Petroleum Engineers Annual Technical Conference, Paper 102103*.
- McDonal, F. J., Angona, F. A., Mills, R. L., Sengbush, R. L., Van Nostrand, R. G., and White, J. E. (1958). Attenuation of shear and compressional waves in pierre shale. *Geophysics*, 23(3):421–439.
- McMechan, G. A. (1982). Determination of source parameters by wavefield extrapolation. *Geophysical Journal International*, 71(3):613–628.
- Meng, Z., Zhang, J., and Wang, R. (2011). In-situ stress, pore pressure and stress-dependent permeability in the Southern Qinshui Basin. *International Journal of Rock Mechanics & Mining Sciences*, 48(1):122–131.
- Millich, E., Neugebauer, H. J., Huenges, E., and Nover, G. (1998). Pressure dependence of permeability and earth tide induced fluid flow. *Geophysical Research Letters*, 25(6):809–812.
- Mohr, C. O. (1914). *Abhandlungen aus dem Gebiet der Technischen Mechanik*. Ernst und Sohn, Berlin, 2<sup>nd</sup> edition.
- Moore, D. E., Lockner, D. A., and Byerlee, J. D. (1994). Reduction of Permeability in Granite at Elevated Temperatures. *Science*, 265(5178):1558–1561.
- Morrow, C. A. and Lockner, D. A. (1997). Permeability and porosity of the Illinois UPH 3 drillhole granite and a comparison with other deep drillhole rocks. *Journal of Geophysical Research*, 102(B2):3067–3075.

- Morrow, C. A., Moore, D. E., and Byerlee, J. D. (1984). Permeability Changes in Crystalline Rocks Due to Temperature: Effects of Mineral Assemblage. *MRS On-line Proceedings Library*, 44.
- Morrow, C. A., Moore, D. E., and Lockner, D. A. (2001). Permeability reduction in granite under hydrothermal conditions. *Journal of Geophysical Research: Solid Earth*, 106(B12):30551–30560.
- Müller, T. M. and Hummel, N. (2008). Nonlinear Pore Pressure Diffusion and Associated Microseismicity in Rocks with Pressure-dependent Permeability. *70<sup>th</sup> EAGE Conference & Exhibition, Extended Abstracts*, B042.
- Muraoka, H., Uchida, T., Sasada, M., Yagi, M., Akaku, K., Sasaki, M., Yasukawa, K., Ichi Miyazaki, S., Doi, N., Saito, S., Sato, K., and Tanaka, S. (1998). Deep geothermal resources survey program: igneous, metamorphic and hydrothermal processes in a well encountering 500°C at 3729 m depth, Kakkonda, Japan. *Geothermics*, 27(5–6):507 – 534.
- Nathenson, M. (1999). The dependence of permeability on effective stress from flow tests at hot dry rock reservoirs at Rosemanowes (Cornwall) and Fenton Hill (New Mexico). *Geothermics*, (28):315–340.
- Nicholson, C. and Wesson, R. L. (1992). Triggered earthquakes and deep well activities. *Pure and Applied Geophysics*, 139(3/4):561–578.
- Nordgren, R. P. (1972). Propagation of a vertical hydraulic fracture. *SPE J.*, 12(8):306–314.
- Novakowski, K. S., Evans, G. V., Lever, D. A., and Raven, K. G. (1985). A Field Example of Measuring Hydrodynamic Dispersion in a Single Fracture. *Water Resources Research*, 21(8):1165–1174.
- Novakowski, K. S., Lapcevic, P. A., Voralek, J., and Bickerton, G. (1995). Preliminary interpretation of tracer experiments conducted in a discrete rock fracture under conditions of natural flow. *Geophysical Research Letters*, 22(11):1417–1420.
- Nur, A. M., Walls, J. D., Winkler, K., and DeVilbiss, J. (1980). Effects of Fluid Saturation on Waves in Porous Rock and Relations to Hydraulic Permeability. *Society of Petroleum Engineers Journal*, 20(6):450–458.
- Osborn, S. G., Vengosh, A., Warner, N. R., and Jackson, R. B. (2011). Methane contamination of drinking water accompanying gas-well drilling and hydraulic fracturing. *Physical Sciences - Environmental Sciences*, 108(20):8172–8176.
- Othake, M. (1974). Seismic activity induced by water injection at Matsushiro, Japan. *Journal of Physics of the Earth*, 22:163–176.

## References

---

- Ottmöller, L., Nielsen, H. H., Atakan, K., Braunmiller, J., and Havskov, J. (2005). The 7 May 2001 induced seismic event in the Ekofisk oil field, North Sea. *Journal of Geophysical Research: Solid Earth*, 110(B10).
- Pape, H., Clauser, C., and Iffland, J. (1999). Permeability prediction based on fractal pore-space geometry. *Geophysics*, 64(5):1447–1460.
- Parotidis, M., Shapiro, S. A., and Rothert, E. (2004). Back front of seismicity induced after termination of borehole fluid injection. *Geophysical Research Letters*, 31(L02612).
- Pearson, C. (1981). The relationship between microseismicity and high pore pressure during hydraulic stimulation experiments in low permeability granitic rocks. *Journal of Geophysical Research*, 86:7855–7864.
- Pechinig, R., Haverkamp, S., Wohlenberg, J., Zimmermann, G., and Burkhardt, H. (1997). Integrated log interpretation in the German Continental Deep Drilling Program: Lithology, porosity, and fracture zones. *Journal of Geophysical Research*, 102(B8):18363–18390.
- Penny, G. S., Conway, M. W., and Lee, W. (1985). Control and Modeling of Fluid Leakoff During Hydraulic Fracturing. *Journal of Petroleum Technology*, 37(6).
- Perkins, T. K. and Kern, L. R. (1961). Width of hydraulic fractures. *Journal of Petroleum Technology*, 13(9):937–949.
- Pettijohn, F. J. (1948). A Preface to the Classification of the Sedimentary Rocks. *The Journal of Geology*, 56(2).
- Plumb, R. A. and Hickman, S. H. (1985). Stress-induced borehole elongation: A comparison between the four-arm dipmeter and the borehole televiewer in the Auburn Geothermal Well. *Journal of Geophysical Research*, 90(B7):5513–5521.
- Polak, A., Elsworth, D., Yasuhara, H., Grader, A. S., and Halleck, P. M. (2003). Permeability reduction of a natural fracture under net dissolution by hydrothermal fluids. *Geophysical Research Letters*, 30(20):1–4.
- Potter, R. M., Robinson, E. S., and Smith, M. C. (1974). Method of extracting heat from dry geothermal reservoirs. *US Patent No 3786858*.
- Raleigh, C. B., Haley, J. H., and Bredehoeft, J. D. (1972). Faulting and crustal stress at Rangely Colorado. *Flow and fracture of rocks, Geophysical Monograph, American Geophysical Union*, 16:275–284.
- Raleigh, C. B., Healy, J. H., and Bredehoeft, J. D. (1976). An Experiment in Earthquake Control at Rangely, Colorado. *Science*, 191(4233):1230–1237.

- Rasmuson, A. and Neretnieks, I. (1986). Radionuclide Transport in Fast Channels in Crystalline Rock. *Water Resources Research*, 22(8):1247–1256.
- Raven, K. G., Novakowski, K. S., and Lapcevic, P. A. (1988). Interpretation of field tracer tests of a single fracture using a transient solute storage model. *Water Resources Research*, 24(12):2019–2032.
- Renpu, W. (2011). *Advanced Well Completion Engineering*. Gulf Professional Publishing, 3<sup>rd</sup> edition.
- Reshetnikov, A., Kummerow, J., Shapiro, S. A., Assanuma, H., and Häring, M. (2010). Microseismic Imaging of a Hydraulic Reservoir Stimulation: Basel. *6<sup>th</sup> Annual PHASE Report*, pages 23–33.
- Rothert, E. and Shapiro, S. A. (2003). Microseismic monitoring of borehole fluid injections: Data modeling and inversion for hydraulic properties of rocks. *Geophysics*, 68(2):685–689.
- Rothert, E. and Shapiro, S. A. (2007). Statistics of fracture strength and fluid-induced microseismicity. *Journal of Geophysical Research*, 112(B04309).
- Rudnicki, J. W. (1986). Fluid mass sources and point forces in linear elastic diffusive solids. *Mechanics of Materials*, 5:383–393.
- Rutledge, J. T. and Phillips, W. S. (2003). Hydraulic stimulation of natural fractures as revealed by induced microearthquakes, Carthage Cotton Valley gas field, east Texas. *Geophysics*, 68(2):441–452.
- Rutledge, J. T., Phillips, W. S., and Mayerhofer, M. J. (2004). Faulting Induced by Forced Fluid Injection and Fluid Flow Forced by Faulting: An Interpretation of Hydraulic-Fracture Microseismicity, Carthage Cotton Valley Gas Field, Texas. *Bulletin of the Seismological Society of America*, 94(5):1817–1830.
- Rutledge, J. T., Phillips, W. S., and Schuessler, B. K. (1998). Reservoir characterization using oil-production-induced microseismicity, Clinton County, Kentucky. *Tectonophysics*, 289:129–152.
- Sanchez-Palencia, E. (1980). *Non-Homogeneous Media and Vibration Theory*. Springer Verlag, New York, NY.
- Sayers, C. M. (2005). Seismic anisotropy of shales. *Geophysical Prospecting*, 53(5):667–676.
- Scholz, C. H. (2002). *Mechanics of Earthquake and Faulting*. Cambridge University Press, New York, NY., 2<sup>nd</sup> edition.

## References

---

- Schubert, G., Turcotte, D., and Olson, P. (2001). *Mantle Convection in the Earth and Planets 2 Volume Set*. Cambridge University Press.
- Seeburger, D. A. and Zoback, M. D. (1982). The distribution of natural fractures and joints at depth in crystalline rock. *Journal of Geophysical Research: Solid Earth*, 87(B7):5517–5534.
- Shapiro, S. A. (2008). Microseismicity - a tool for reservoir characterization. EAGE Publications, Houten.
- Shapiro, S. A., Audigane, P., and Royer, J.-J. (1999). Large-scale *in situ* permeability tensor of rocks from induced microseismicity. *Geophysical Journal International*, 137(1):207–213.
- Shapiro, S. A. and Dinske, C. (2008). Microseismicity of Non-linear Fluid-rock Interactions - From Geothermic Stimulations to Fracturing of Barnett Shales. *70<sup>th</sup> EAGE Conference & Exhibition, Extended Abstracts*, B041.
- Shapiro, S. A. and Dinske, C. (2009a). Fluid-induced seismicity: Pressure diffusion and hydraulic fracturing. *Geophysical Prospecting*, 57(2):301–310.
- Shapiro, S. A. and Dinske, C. (2009b). Scaling of seismicity induced by nonlinear fluid-rock interaction. *Journal of Geophysical Research*, 114(B9).
- Shapiro, S. A., Dinske, C., Langenbruch, C., and Wenzel, F. (2010). Seismogenic index and magnitude probability of earthquakes induced during reservoir fluid stimulations. *The Leading Edge*, 29:304–309.
- Shapiro, S. A., Dinske, C., and Rothert, E. (2006). Hydraulic-fracturing controlled dynamics of microseismic clouds. *Geophysical Research Letters*, 33(14).
- Shapiro, S. A., Huenges, E., and Borm, G. (1997). Estimating the crust permeability from fluid-injection-induced seismic emission at the KTB site. *Geophysical Journal International*, 131(F15 - F18).
- Shapiro, S. A., Rentsch, S., and Rothert, E. (2005). Characterization of hydraulic properties of rocks using probability of fluid-induced microearthquakes. *Geophysics*, 70(2):F27–F33.
- Shapiro, S. A., Rothert, E., Rath, V., and Rindschwentner, J. (2002). Characterization of fluid transport properties of reservoirs using induced microseismicity. *Geophysics*, 67(1):212–220.
- Sheriff, R. E. (2002). *Encyclopedic Dictionary of Applied Geophysics*. Society of Exploration Geophysicists, 4<sup>th</sup> edition.

- Smith, M. C. (1983). A history of hot dry rock geothermal energy systems. *Journal of Volcanology and Geothermal Research*, 15(1–3):1 – 20.
- Somerton, W. H., Söylemezoğlu, I. M., and Dudley, R. (1975). Effect of stress on permeability of coal. *International Journal of Rock Mechanics and Mining Sciences & Geomechanics Abstracts*, 12(5–6):129 – 145.
- Stevenson, D. (2004). Earth science: Inside history in depth. *Nature*, 428:476–477.
- Summers, R., Winkler, K., and Byerlee, J. (1978). Permeability changes during the flow of water through westerly granite at temperatures of 100° – 400°C. *Journal of Geophysical Research: Solid Earth*, 83(B1):339–344.
- Talebi, S., Nechtschein, S., and Boone, T. J. (1998). Seismicity and Casing Failures Due to Steam Stimulation in Oil Sands. *Pure and Applied Geophysics*, 153:219–233.
- Talwani, P. and Acree, S. (1985). Pore pressure diffusion and the mechanism of reservoir-induced seismicity. *Pure and Applied Geophysics*, 122:947–965.
- Teng, T. L., Real, C. R., and Henyey, T. L. (1973). Microearthquakes and water flooding in Los Angeles. *Bulletin of the Seismological Society of America*, 63(3):859–875.
- Tenzer, H. (2001). Development of hot dry rock technology. *Bulletin Geo-Heat Center*, 32(4):14–22.
- Terzaghi, K. (1936). The shearing resistance of saturated soils and the angle between planes of shear. In *Int. Conf. Soil Mech. Found. Eng.*, volume 1, pages 54–56. Harvard University Press, Cambridge, MA.
- Thompson, J. E., Gregory, G., and Gerbrandt, D. (1992). New Continuous-Mix Process for Gelling Anhydrous Methanol Minimizes Hazards. *Journal of Petroleum Technology*, 44(7):832–839.
- Thurber, C. H. and Rabinowitz, N. (2000). *Advances in Seismic Event Location*. Modern Approaches in Geophysics. Springer.
- Tiab, D. and Donaldson, E. C. (2004). *Petrophysics*. Elsevier, Gulf Professional Publishing, 2<sup>nd</sup> edition.
- Tiller, F. M. (1955). The role of porosity in filtration. Part 2. Analytical equations for constant rate filtration. *Chemical Engineering Progress*, 51:282–290.
- Tucker, M. E. (2001). *Sedimentary Petrology: An Introduction to the Origin of Sedimentary Rocks*. Wiley-Blackwell.

## References

---

- Urbancic, T., Shumila, V., and Rudledge, J. (1999). Determining hydraulic fracture behavior using microseismicity. *Vail Rock '99, 37<sup>th</sup> U.S. Rock Mechanics Symposium, Vail, Colorado*.
- Vaughan, P. J., Moore, D. E., Morrow, C. A., and Byerlee, J. D. (1986). Role of cracks in progressive permeability reduction during flow of heated aqueous fluids through granite. *Journal of Geophysical Research: Solid Earth*, 91(B7):7517–7530.
- Vidic, R. D., Brantley, S. L., Vandenbossche, J. M., Yoxtheimer, D., and Abad, J. D. (2013). Impact of Shale Gas Development on Regional Water Quality. *Science*, 340.
- Viegas, G., Baig, A., Coulter, W., and Urbancic, T. (2012). Effective monitoring of reservoir-induced seismicity utilizing integrated surface and downhole seismic networks. *First Break*, 30(7):77–81.
- Walls, J. D., Nur, A. M., and Bourbie, T. (1982). Effects of Pressure and Partial Water Saturation on Gas Permeability in Tight Sands: Experimental Results. *Journal of Petroleum Technology*, 34(4):930–936.
- Walsh, J. B. (1981). Effect of pore pressure and confining pressure on fracture permeability. *International Journal of Rock Mechanics and Mining Sciences & Geomechanics Abstracts*, 18(5):429–35.
- Warpinski, N. R. (1991). Hydraulic Fracturing in Tight, Fissured Media. *Journal of Petroleum Technology*, 43(2).
- Warpinski, N. R., Branagan, P. T., Peterson, R. E., Wohlhart, S. L., and Uhl, J. E. (1998). Mapping Hydraulic Fracture Growth and Geometry Using Microseismic Events Detected by a Wireline Retrievable Accelerometer Array. *Proceedings, Society of Petroleum Engineers, SPE Gas Technology Symposium, Paper 40014*.
- Warpinski, N. R., Kramm, R. C., Heinze, J. R., and Waltmann, C. K. (2005). Comparison of Single- and Dual-Array Microseismic Mapping Techniques in the Barnett Shale. *Proceedings, Society of Petroleum Engineers Annual Technical Conference, Paper 95568*.
- Waters, G. A., Lewis, R. E., and Bentley, D. C. (2011). The Effect of Mechanical Properties Anisotropy in the Generation of Hydraulic Fractures in Organic Shales. *Proceedings, Society of Petroleum Engineers Annual Technical Conference, Paper 146776*.
- Wenk, H.-R., Lonardelli, I., Franz, H., Nihei, K., and Nakagawa, S. (2007). Preferred orientation and elastic anisotropy of illite-rich shale. *Geophysics*, 72(2):E69–E75.

- Witherspoon, P. A., Wang, J. S. Y., Iwai, K., and Gale, J. E. (1980). Validity of Cubic Law for fluid flow in a deformable rock fracture. *Water Resources Research*, 16(6):1016–1024.
- Yilmaz, O., Nolen-Hoeksema, R. C., and Nur, A. (1994). Pore pressure profiles in fractured and compliant rocks. *Geophysical Prospecting*, 42:693–714.
- Zemanek, J., Glenn, E., Norton, L., and Caldwell, R. (1970). Formation evaluation by inspection with the borehole televiewer. *Geophysics*, 35(2):254–269.
- Zimmerman, R. W. and Bodvarsson, G. S. (1996). Hydraulic conductivity of rock fractures. *Transport in Porous Media*, 23(1):1–30.
- Zoback, M. D., Barton, C. A., Brudy, M., Castillo, D. A., Finkbeiner, T., Grollimund, B. R., Moos, D. B., Peska, P., Ward, C. D., and Wiprut, D. J. (2003). Determination of stress orientation and magnitude in deep wells. *International Journal of Rock Mechanics & Mining Sciences*, 40(7–8):1049–1076.
- Zoback, M. D. and Harjes, H. P. (1997). Injection-induced earthquakes and crustal stress at 9 km depth at the KTB deep drilling site, Germany. *Journal of Geophysical Research*, 102:18477 – 18491.
- Zoback, M. D. and Townend, J. (2001). Implications of hydrostatic pore pressures at high crustal strength for the deformation of intraplate lithosphere. *Tectonophysics*, 336:19–30.
- Zoback, M. D. and Zinke, J. C. (2002). Production-induced Normal Faulting in the Valhall and Ekofisk Oil Fields. *Pure and Applied Geophysics*, 159:403–420.
- Zoback, M. D. and Zoback, M. L. (2002). State of stress in the earth's lithosphere. In William H.K. Lee, Hiroo Kanamori, P. C. J. and Kisslinger, C., editors, *International Handbook of Earthquake and Engineering Seismology*, volume 81, Part A of *International Geophysics*, pages 559–568. Academic Press.

## References

---

# List of Figures

	<b>Page</b>
<b>Chapter 1 – General introduction</b>	<b>1</b>
1.1 Simplified sketch of rocks consisting of grains and pores . . . . .	2
1.2 Range of permeability magnitudes for different types of rocks. . . . .	3
1.3 Permeability $k$ as a function of effective pressure . . . . .	5
1.4 Applications of borehole fluid injections . . . . .	9
1.5 Mohr-Coulomb failure criterion and the effect of pore fluids . . . . .	12
1.6 Categorization of different types of fractures . . . . .	13
1.7 $r - t$ diagram with triggering front and back front . . . . .	17
1.8 $r - t$ diagram of hydraulic fracturing induced seismicity . . . . .	20
1.9 Conceptual idea of both pressure-dependent diffusivity models . . . . .	20
 <b>Chapter 2 – Microseismic estimates of hydraulic diffusivity in case of non-linear fluid-rock interaction</b>	 <b>25</b>
2.1 Computation of the effective diffusivity for a synthetic event cloud . . . . .	35
2.2 Comparison of effective and heuristic diffusivity values . . . . .	37
2.3 Pore pressure profiles for different non-linear parameters $n$ and $\kappa$ . . . . .	38
2.4 Medium diffusivity for different non-linear parameters $n$ and $\kappa$ . . . . .	39
2.5 Synthetic seismicity clouds for the exponential diffusion model . . . . .	41
2.6 Synthetic seismicity clouds for the power-law diffusion model . . . . .	43
2.7 Model geometry and pressure evolution for averaging validation . . . . .	50
 <b>Chapter 3 – Non-linear diffusion-based interpretation of induced microseismicity: A Barnett Shale hydraulic fracturing case study</b>	 <b>51</b>

<b>Chapter 4 – Back front of seismicity induced by non-linear fluid-rock interaction</b>	<b>81</b>
4.1 Model concept of a pressure-dependent diffusivity . . . . .	86
4.2 Induced seismicity for the Ogachi experiment . . . . .	94
4.3 Temporal evolution of Ogachi seismicity . . . . .	95
4.4 Temporal evolution of normalized Ogachi seismicity . . . . .	96
4.5 $r - t$ diagram of normalized Ogachi seismicity . . . . .	97
4.6 Induced seismicity for the Fenton Hill experiment . . . . .	99
4.7 Temporal evolution of Fenton Hill seismicity . . . . .	100
4.8 Temporal evolution of normalized Fenton Hill seismicity . . . . .	101
4.9 $r - t$ diagram of normalized Fenton Hill seismicity . . . . .	102
4.10 Real data showing (mis)match of the linear diffusion back front . . . . .	104
4.11 Frozen diffusivity model . . . . .	106
4.12 Impact of non-linearity on pore-fluid pressure profiles . . . . .	108
4.13 Impact of non-linearity on synthetic seismicity clouds . . . . .	110
4.14 Real data motivated clouds of synthetic seismicity . . . . .	114
4.15 Results obtained for the non-linear diffusivity model . . . . .	117
<b>Chapter A – Estimates of fracture geometry and fluid transport properties from hydraulic fracturing induced seismicity</b>	<b>133</b>
A.1 Engineering data $r - t$ plot of induced seismicity . . . . .	139
A.2 Map and side view of induced seismicity . . . . .	140
A.3 Temporal evolution of induced seismicity . . . . .	141
A.4 Evaluation of the fracture width . . . . .	142
A.5 Estimation of fluid-loss coefficient . . . . .	144
A.6 Estimation of fracture body diffusivity . . . . .	145

# List of Tables

	<b>Page</b>
<b>Chapter 1 – General introduction</b>	<b>1</b>
1.1 Compilation of documented permeability compliances . . . . .	6
<b>Chapter 2 – Microseismic estimates of hydraulic diffusivity in case of non-linear fluid-rock interaction</b>	<b>25</b>
2.1 Diffusivity values obtained for the exponential diffusion model . . . .	42
2.2 Diffusivity values obtained for the power-law diffusion model . . . .	44
<b>Chapter 3 – Non-linear diffusion-based interpretation of induced microseismicity: A Barnett Shale hydraulic fracturing case study</b>	<b>51</b>
<b>Chapter 4 – Back front of seismicity induced by non-linear fluid-rock interaction</b>	<b>81</b>
4.1 Documented permeability compliances . . . . .	87
<b>Chapter A – Estimates of fracture geometry and fluid transport properties from hydraulic fracturing induced seismicity</b>	<b>133</b>
A.1 Overview of computed reservoir parameters . . . . .	146

## List of Tables

---

# Curriculum Vitae

For privacy reasons, the CV was removed in the digital version.



## Publications and conference abstracts

- 2013:**
34. Hummel, N. and Shapiro, S. A. (2013). Non-linear diffusion-based interpretation of induced microseismicity: A Barnett Shale hydraulic fracturing case study. In *Geophysics*, 78(5), B211–B226, Society of Exploration Geophysicists, doi: 10.1190/GEO2012-0242.1.
  33. Shapiro, S. A. and Hummel, N. (2013). Non-linear diffusion-based Interpretation of Hydraulic Fracturing Induced Seismicity. In *Frontiers of Shale Gas Extraction and Microseismic Monitoring, 75<sup>th</sup> EAGE Conference & Exhibition incorporating SPE EUROPEC, London*. European Association of Geoscientists & Engineers, doi: 10.3997/2214-4609.20131177.
  32. Hummel, N. and Shapiro, S. A. (2013). Microseismic permeability characterization from hydraulic fracturing of shales. In *EAGE Fourth Passive Seismic Workshop, Extended Abstracts, number PS28, Amsterdam*. European Association of Geoscientists & Engineers.
  31. Hummel, N. and Shapiro, S. A. (2013). Back front signatures of seismicity based on non-linear pore pressure diffusion. 73. *Jahrestagung der Deutschen Geophysikalischen Gesellschaft, Tagungsband, SO-1.005, Leipzig*.
  30. Hummel, N. and Shapiro, S. A. (2013). Diffusivity tensor characterization based on the back front of induced seismicity. 73. *Jahrestagung der Deutschen Geophysikalischen Gesellschaft, Tagungsband, SO-1.004, Leipzig*.
  29. Hummel, N. and Shapiro, S. A. (2013). Permeability reconstruction using hydraulic fracturing induced seismicity. 73. *Jahrestagung der Deutschen Geophysikalischen Gesellschaft, Tagungsband, SO-1.003, Leipzig*.

- 2012:** 28. Hummel, N. and Shapiro, S. A. (2012). Characterization of the permeability evolution and non-linear fluid-rock interaction from induced seismicity. *American Geophysical Union, Fall Meeting, abstract, S43D-2490, San Francisco.*
27. Hummel, N. and Shapiro, S. A. (2012). Back front signatures of seismicity induced by non-linear fluid-rock interaction. In *SEG Global Meeting Abstracts, - International Geophysical Conference and Oil & Gas Exhibition, pages 1-4, Istanbul.* Society of Exploration Geophysicists and The Chamber of Geophysical Engineers of Turkey, doi: 10.1190/IST092012-001.146.
26. Hummel, N. and Shapiro, S. A. (2012). Microseismic permeability estimates from hydraulic fracturing of shales. In *SEG Global Meeting Abstracts, - International Geophysical Conference and Oil & Gas Exhibition, pages 1-4, Istanbul.* Society of Exploration Geophysicists and The Chamber of Geophysical Engineers of Turkey, doi: 10.1190/IST092012-001.144.
25. Hummel, N. and Shapiro, S. A. (2012). Microseismic estimates of hydraulic diffusivity in case of non-linear fluid-rock interaction. *Geophysical Journal International*, 188:1441-1453, doi: 10.1111/j.1365-246X.2011.05346.x.
24. Franke, S., Hummel, N., and Shapiro, S. A. (2012). Overview of a data set of a three stage hydraulic fracturing treatment in a shale gas reservoir. *8<sup>th</sup> Annual PHASE Report.*
23. Hummel, N. and Shapiro, S. A. (2012). Permeability tensor characterization from the back front of seismicity. *8<sup>th</sup> Annual PHASE Report.*
22. Hummel, N. and Shapiro, S. A. (2012). Influence of non-linear fluid-rock interaction on the back front of seismicity. *8<sup>th</sup> Annual PHASE Report.*

- 2011:** 21. Hummel, N. and Shapiro, S. A. (2011). Non-linear diffusion estimates from hydraulic fracturing of shales. In *SEG Technical Program Expanded Abstracts, pages 1544-1549, San Antonio*. Society of Exploration Geophysicists, doi: 10.1190/1.3627497.
20. Hummel, N. and Shapiro, S. A. (2011). Transport properties from microseismics: Comparing heuristic and effective values from non-linear fluid-rock interaction. In *EAGE Third Passive Seismic Workshop - Actively Passive!, Extended Abstracts, number PSP02, Athens*. European Association of Geoscientists & Engineers.
19. Hummel, N. and Shapiro, S. A. (2011). Estimates of hydraulic diffusivity from microseismicity based on non-linear fluid-rock interaction. *71. Jahrestagung der Deutschen Geophysikalischen Gesellschaft, Tagungsband, SO 01, Köln*.
18. Reshetnikov, A., Hummel, N., and Shapiro, S. A. (2011). A hydraulic fracturing case study (III): Interpretation of new locations and comparative analysis of fracture geometry and fluid transport properties. *7<sup>th</sup> Annual PHASE Report*.
17. Hummel, N. and Shapiro, S. A. (2011). A hydraulic fracturing case study (I): Estimates of fracture geometry and fluid transport properties from hydraulic fracturing induced seismicity. *7<sup>th</sup> Annual PHASE Report*.
16. Hummel, N. and Shapiro, S. A. (2011). Microseismic back front signatures for non-linear fluid-rock interaction. *7<sup>th</sup> Annual PHASE Report*.
- 2010:** 15. Hummel, N. and Shapiro, S. A. (2010). Estimates of hydraulic transport parameters using microseismicity induced by non-linear fluid-rock interaction. In *SEG Technical Program Expanded Abstracts, pages 2156-2160, Denver*. Society of Exploration Geophysicists, doi: 10.1190/1.3513272.
14. Hummel, N. and Shapiro, S. A. (2010). Quantitative analysis of diffusivity estimates obtained from microseismicity based on non-linear diffusion. *72<sup>nd</sup> EAGE Conference & Exhibition, Extended Abstracts, P564, Barcelona*. European Association of Geoscientists & Engineers.
13. Hummel, N. and Shapiro, S. A. (2010). Influence of non-linear fluid-rock interaction on hydraulic fracturing induced seismicity from Barnett Shale. *6<sup>th</sup> Annual PHASE Report*.

- 2009:**
12. Hummel, N. and T. M. Müller (2009). Microseismic signatures of non-linear pore-fluid pressure diffusion. *Geophysical Journal International*, 179(3):1558-1565, doi: 10.1111/j.1365-246X.2009.04373.x.
  11. Hummel, N. and Shapiro, S. A. (2009). Influence of non-linear fluid-rock interaction on estimates of hydraulic diffusivity from microseismic data. In *SEG Technical Program Expanded Abstracts, pages 1576-1580, Houston*. Society of Exploration Geophysicists, doi: 10.1190/1.3255150.
  10. Hummel, N. and Shapiro, S. A. (2009). Nature of diffusivity estimates from microseismicity induced by non-linear fluid-rock interaction. *71<sup>st</sup> EAGE Conference & Exhibition, Extended Abstracts, P032, Amsterdam*. European Association of Geoscientists & Engineers.
  9. Hummel, N. and Shapiro, S. A. (2009). Nature of diffusivity estimates from microseismicity induced by non-linear fluid-rock interaction. *69. Jahrestagung der Deutschen Geophysikalischen Gesellschaft, Tagungsband, SM 07, Kiel*.
  8. Hummel, N. and Shapiro, S. A. (2009). Quantitative analysis of diffusivity estimates obtained from microseismicity with underlying pressure dependent transport properties. *5<sup>th</sup> Annual PHASE Report*.
- 2008:**
7. Hummel, N. and Shapiro, S. A. (2008). Diffusivity calculations for 1D non-linear microseismicity. *4<sup>th</sup> Annual PHASE Report*.
  6. Hummel, N. and Müller, T. M. (2008). Microseismic signatures of non-linear pore pressure diffusion. In *SEG Technical Program Expanded Abstracts 2008, pages 1382-1386, Las Vegas*. Society of Exploration Geophysicists, doi: 10.1190/1.3059174.
  5. Müller, T. M. and Hummel, N. (2008). Non-linear pore pressure diffusion and associated microseismicity in rocks with pressure-dependent permeability. *70<sup>th</sup> EAGE Conference & Exhibition, Extended Abstracts, B042, Rome*. European Association of Geoscientists & Engineers.
  4. Hummel, N. and Müller, T. M. (2008). Microseismic signatures of non-linear pore pressure diffusion. *70<sup>th</sup> EAGE Conference & Exhibition, Extended Abstracts, P022, Rome*. European Association of Geoscientists & Engineers.
  3. Hummel, N. and Müller, T. M. (2008). Numerical modelling and interpretation of microseismic signatures related to non-linear pore pressure diffusion. *68. Jahrestagung der Deutschen Geophysikalischen Gesellschaft, Tagungsband, PSM 7, Freiberg*.

- 2007:**
2. Müller, T. M. and Hummel, N. (2007). The physics of non-linear diffusion and associated microseismicity in rocks with pressure-dependent permeability. *3<sup>rd</sup> Annual PHASE Report*.
  1. Hummel, N. and Müller, T. M. (2007). Non-linear diffusion - numerical modelling and interpretation of microseismic signatures related to hydraulic fracturing. *3<sup>rd</sup> Annual PHASE Report*.



# Acknowledgements - Danksagung

Am Ende dieser Arbeit möchte ich mich bei zahlreichen Personen bedanken, die direkt oder indirekt zur Entstehung dieser Dissertation beigetragen haben.

Hierbei gilt mein besonderer Dank an erster Stelle Prof. Dr. Serge Shapiro, der mir nicht nur die Möglichkeit zu dieser Arbeit gegeben hat, sondern dessen hervorragende Betreuung maßgeblich zum Gelingen dieser Arbeit beigetragen hat. Dies berücksichtigt sowohl die mir in zahlreichen Gesprächen und Diskussionen vermittelten Anregungen als auch seine Bereitschaft mir den nötigen Freiraum zur Umsetzung zahlreicher Ideen zu gewähren. Ferner war er stets bereit, mich in allen Belangen und Vorhaben, wie z.B. der Organisation und Durchführung archäogeophysikalischer Messungen oder dem Forschungsaufenthalt in England, ausnahmslos zu unterstützen.

PD Dr. Erik Saenger danke ich sowohl für die Übernahme des Korreferats als auch für die aufschlussreichen Gespräche und Diskussionen. Ebenso bedanke ich mich bei den Mitgliedern der Prüfungskommission, Prof. Dr. Harry Becker, Prof. Dr. Marco Bohnhoff als deren Vorsitzender, sowie Dr. Carsten Dinske.

Ebenso seien hier meine Kolleginnen und Kollegen der Fachrichtung Geophysik genannt, bei denen ich mich für die gute Zusammenarbeit und den regen Gedankenaustausch sowohl während, als auch außerhalb der Dienstzeiten bedanken möchte. Dies gilt insbesondere für meinen Bürokollegen Dr. Carsten Dinske, der zusammen mit Dr. Jörn Kummerow, Anton Reshetnikov und Oliver Krüger stets bereit war meine Manuskripte sorgfältig Korrektur zu lesen. Nicht nur mit ihnen, sondern auch zusammen mit Cornelius Langenbruch und Karsten Stürmer durfte ich viele interessante, lehrreiche aber auch angenehm ausgestaltete Dienstreisen nach Amsterdam, Athen, Barcelona, Denver, Goslar, Houston, Köln, Las Vegas, San Antonio und San Francisco erleben.

Zuletzt möchte ich mich bei Anna-Sophia bedanken, die mich über die gesamte Zeit liebevoll, aufmerksam und tatkräftig unterstützt bzw. motiviert hat. Nicht nur ihre Anregungen, sondern auch ihr Rückhalt haben sehr zum Gelingen dieser Arbeit beigetragen.